THE APPLICATION OF CONTACT MECHANICS TO THE NUMERICAL SIMULATION OF PARTICULATE MATERIAL.

Clive William Randall, B.Sc.

Doctor of Philosophy

THE UNIVERSITY OF ASTON IN BIRMINGHAM

September 1989

The University of Aston in Birmingham.

THE APPLICATION OF CONTACT MECHANICS TO THE NUMERICAL SIMULATION OF PARTICULATE MATERIAL.

Clive William Randall.

Thesis submitted for the degree of Doctor of Philosophy.
September 1989.

Summary

Particulate solids are complex systems, comprising of discrete particles, which can incorporate many redundancies. The interactions between the particles are complex and have been the subject of many theoretical and experimental investigations. Investigations of particulate material have been restricted by the lack of quantitative information on the mechanisms occurring within an assembly. Laboratory experimentation is limited as information on the internal behaviour can only be inferred from measurements on the assembly boundary, or the use of intrusive measuring devices. In addition comparisons between test data are uncertain due to the difficulty in reproducing exact replicas of physical systems. An alternative is to numerically simulate particulate behaviour. Numerical simulation provides information on every particle and hence the micro-mechanical behaviour within an assembly, and can replicate desired systems.

To use a computer program to numerically simulate material behaviour accurately it is necessary to incorporate realistic interaction laws. This research programme, which used the finite difference simulation program 'BALL', developed by Cundall (1971), was primarily concerned with replacing the linear spring force-displacement laws by the more realistic interaction laws of Hertz (1882) and Mindlin and Deresiewicz (1953).

Verification of the new contact force-displacement laws was achieved by simulating a quasi-static oblique contact and single particle oblique impact. Applications of the program to the simulation of large assemblies of particles are provided, and the problems in undertaking quasi-static shear tests along with the results from two successful shear tests are described.

Key words: Computer simulated experiments
Contact mechanics
Granular / Particulate media
Oblique impact
Quasi-static shear deformation.

Dedication.

This thesis is dedicated to my parents, to whom I will be eternally grateful.

Acknowledgements.

I am extremely grateful to my research supervisor, Dr C.Thornton, for his support, guidance and continued optimism even during periods of extreme adversity.

I would like to thank my fiancee Sue for her tremendous support during the rigours of research and her assistance with the typing and production of this manuscript.

I would also like to acknowledge the work done in the undergraduate research projects of J.C.Platts and S.P.Webster in applying the program to the simulation of particle flow from hoppers and the pluvial deposition of a bed of particles.

Contents.

Chapter 4.

Chapter 5.

Chapter 6.

List of Figures.

Chapter 3.

Chapter 4.

Chapter 5.

Chapter 6.

1. Introduction.

The investigation of particulate assemblies is well established, and many empirical, theoretical and statistical analyses of assemblies have been performed. However, due to the complex nature of the interaction of each particle affecting the behaviour of the assembly as a whole, no entirely satisfactory constitutive relationships have been established. It is difficult to verify any proposed constitutive relationships for aspects of quasi-static behaviour by laboratory experimentation. This is due to internal stresses being inferred from boundary measurements. The ideal laboratory apparatus to determine or verify constitutive relationships would require non-intrusive measuring devices which could measure contact stresses, contact forces, movements and rotations of each particle within an assembly. In an attempt to achieve this many model materials have been developed, such as assemblies of optically sensitive particles and the use of X-ray photography. De Josselin de Jong and Verruijt (1969) used optically sensitive discs and measured contact forces and displacements, though the analysis was time consuming. Difficulties resulted in translating the results of these experiments to a continuum model. Average stresses and strains were determined in an attempt to relate to the continuum but these do not represent all the discrete characteristics of the material behaviour. It is felt by many researchers that numerical simulation may hold the key to the solution of these problems.

Numerical simulation of particulate systems is a wide and rapidly expanding field. Since the 1950's molecular dynamic simulations have been reported, some of which are reviewed

in Chapter 2. Solid particle simulation is a much more recent development and differs from molecular dynamic simulation in that solid particle collisions involve non-recoverable energy losses. There are two main approaches to solid particle system simulation; the 'hard' and 'soft' particle approach. The hard particle system uses instantaneous contacts and coefficients of restitution to represent rebound velocities and angles. Ideal applications are thus dilute systems of rapidly flowing particles where contacts can be justifiably assumed to be instantaneous. The soft particle models use a finite contact duration and force-displacement laws. This more flexible approach means that any system from rapid flow to quasi-static assemblies can be modelled, although the computational requirements can be massive. This restriction is rapidly being overcome as computers become more powerful and cheaper to purchase.

The pioneering work of Cundall (1971) in the use of the soft particle model has been developed by numerous researchers. However, most of the published work to date has been restricted to the investigation of discs and the use of linear spring force-displacement interaction laws with Coulomb type friction. It is only with the adoption of the most realistic interaction laws possible that the simulation and understanding of natural phenomena can be achieved. This research programme was the first to investigate the soft particle simulation of the quasi-static shear deformation of spheres, using the normal force-displacement relationship of Hertz (1882) and the tangential force-displacement laws of Mindlin and Deresiewicz (1953).

The sign convention employed in the simulation program is

such that tensile normal stresses and clockwise shear stresses are taken as positive. However, for ease of pictorial representation in this thesis compressive normal stresses are taken as positive. S.I. units have been introduced into the program and the simulation is restricted to the elastic deformation of topographically smooth spheres.

1.1 Order of presentation.

The work which has been undertaken is covered in the following chapters. In Chapter 2 a literature review is presented which illustrates the evolution of numerical simulation to date. The contact mechanics theories employed in the simulation are given in Chapter 3, whilst Chapter 4 is concerned with the adaptation of the theory into the computer program, along with other coding alterations. Chapter 5 presents results of the validation tests for the new coding and Chapter 6 deals with the simulation of large particle systems. Finally Chapter 7 gives a summary of the thesis and conclusions drawn from the research programme. A breakdown of these chapters is given below.

Chapter 2 describes the historical development of computer simulation starting with the simulations of the 1950's which employed the modified Monte-Carlo integration method. The development of the field of molecular dynamics is traced and some of the numerous applications mentioned. Solid particle system simulation is introduced and the two main methods using 'hard' or 'soft' particles are reviewed. Development of solid 'soft' particle simulation by Cundall is traced and Cundall's papers are reviewed, as are the papers produced by other researchers whose simulation programs were based on

Cundall's program BALL.

Chapter 3 is concerned with the new contact mechanics algorithms coded in the simulation. The normal force-displacement equations for a Hertzian contact are given and the effect of oblique loading is discussed. The tangential force-displacement equations for loading, unloading and reloading for a constant normal force are then developed. The effect of increasing and decreasing the normal force on the loading, unloading and reloading behaviour of a oblique contact is detailed and the equations of Mindlin and Deresiewicz (1953) for these cases are derived. Finally a general solution is presented which encompasses all the cases investigated.

Chapter 4 details the changes to the coding of the simulation program. The historical development of the program BALL is first considered, and then the development of the program at Aston prior to this research programme. The bulk of the chapter illustrates the implementation of the contact mechanics equations. Alterations concerned with particle generation and the implications of considering the particles as spheres are discussed. The new approach to the selection of an appropriate time step to advance the evolution of the system and the introduction of a new strain control facility termed 'the continuum strain rate tensor' is then covered. Modifications and additions to analysis routines are detailed, and finally alterations to graphics facilities are explained.

Chapter 5 is concerned with the validation of the contact mechanics equations detailed in Chapters 3 and 4. Two series of tests are illustrated. The first simulates quasi-static oblique loading to re-produce the force-displacement rela-

tionships defined by Mindlin and Deresiewicz (1953). The second reproduces the impact of a particle against a wall for various angles of incidence. Following the quasi-static tests the equations defined by Hertz (1882) for normal impact are given. Oblique impact is then considered and the analysis presented by Maw et al (1976), which used the laws of Mindlin and Deresiewicz (1953), is outlined. Maw's observations are reported and the results of his oblique impact tests are presented. The oblique impact tests produced by the simulation program are then detailed. These tests successfully reproduce all the observations noted by Maw and give further information on the mechanics of single particle oblique impact.

Chapter 6 presents the results of the simulations of large assemblies of particles. Two undergraduate research projects are briefly mentioned which represent very different applications of the program. The first is the flow of particles from wedge shaped hoppers and the second is the pluvial deposition of a bed of particles. Some instability problems were encountered with the pluvial deposition tests, which were overcome. The remainder of the chapter deals with the quasi-static deformation of large assemblies of particles. Problems encountered in both the isotropic and constant volume shear stage are discussed and resolved. The results of two test simulations, on a uniform and graded assembly, are presented and compared with the 1000 disc assembly reported by Barnes (1985).

Finally, Chapter 7 summarises and draws conclusions from the work done during the research programme.

2 Review of Computer Simulation

2.1 Introduction

The first computer simulation of particle systems employed the modified Monte-Carlo integration method in which particle movements were random so that only average positions were meaningful. These simulations using artificial particle movements gave way to molecular dynamic simulations which used the classical Newtonian or equivalent Lagrangian or Hamiltonian equations of motion. The forces applied to particles were calculated from the influences of their neighbours. The particles then moved under a constant force for a short time interval and then a new force was calculated etc.

A specialised case of these simulations was the hard sphere model. This allows the sequence of events in a multi-bodied system to be described by a series of two bodied collisions. Thus, in a finite system, there will never be more than two particles whose velocities are changing. A time step was used for these molecular dynamic simulations which was the time increment necessary for the next collision to occur. The alteration of the equilibrium equations of motion to satisfy desirable macroscopic constraints led to the new field of non-equilibrium molecular dynamics. Many varied applications followed. Three different particle types were used in these simulations; hard spheres, soft spheres and Lennard-Jones particles.

Essentially the main difference between molecular dynamics and solid particle system simulation is that molecular interactions conserve energy, whilst solid particle collisions involve energy losses which can not be recovered as vibrational kinetic energy of the particles. There are two

approaches to solid particle simulation: the hard sphere and the soft sphere approach. Hard sphere models are based on trajectory changes resulting from instantaneous collisions due to the transference of linear and angular momentum. Soft sphere models generate particle movements from inter-particle force laws and their collisions have a finite duration during which the constantly changing trajectories are continuously updated. Each model has an ideal type of application. The hard sphere particle simulations are ideally suited to long simulations of dilute systems with few collisions or where collisions can be justifiably assumed to be instantaneous. Soft particle models are much more flexible and, with the use of a small fixed time step, they are ideally suited for dense and even static simulations.

The use of coefficients of restitution is attractive because of the simplicity of determining a suitable value for correlation with experimental and theoretical data. However, this is not the most satisfactory approach. The use of a coefficient of restitution to empirically match analytical or experimental results means that the model is only applicable to the particular case studied and does not lead to a true understanding of the physical mechanisms. A better approach is the adoption in the simulation of inter-particle force-displacement laws. The more realistic the interaction laws the more chance of simulating and understanding natural phenomena.

2.2 Molecular dynamics simulations

2.2.1 Origins

One of the earliest papers published on computer simulation

was by Metropolis et al (1953). They used the modified Monte-Carlo integration method, considered two-body forces and assumed that the potential field of a molecule was strictly spherical. Two and three dimensional analyses were undertaken for the Lennard-Jones potential but not presented, though a two dimensional rigid sphere system was discussed. Periodic boundaries were employed which enabled a large assembly to be modelled by a smaller representative element that repeats itself throughout the hypothetically infinite space. If a particle leaves one side of a periodic boundary it re-enters on the opposite side with the same angular and linear momentum it left with. Thus by simulating a relatively small number of particles, conclusions on the behaviour of a large assembly can be drawn. The rigid sphere model with 56 and 224 particles was used to obtain values of pressure for a given volume and temperature. They successfully correlated their results to the free volume equation of state and to a four term viral coefficient expansion.

In 1959 a paper was published by Alder and Wainwright which illustrates the progress in the field of molecular simulation since Metropolis et al. The essential difference between this paper and earlier publications is that a dynamic calculation was now being used as opposed to the modified Monte-Carlo method. The modified Monte-Carlo method generates artificial particle movements such that only the average positions are meaningful. Therefore only equilibrium properties can be calculated. However, the dynamic calculation, which was originally developed to study relaxation phenomena, can also be used for the study of transport properties.

The method used by Alder and Wainwright (1959) calculated

the force on each particle due to the influence of its neighbours. The trajectories were then traced by allowing the particles to move under a constant force for a short time interval. Then a new force was calculated to apply for the next time interval and so on. Thus rotations and anisotropic potentials etc, could be handled. The accuracy of calculation was dependent on the time interval.

The hard sphere potential was a special case. This interaction potential allowed the sequence of events in a many bodied system to be described by a series of two-bodied collisions. Hence, in a finite system there were never more than two particles at a time whose velocities were changing. It was therefore possible to create a more realistic potential using perturbation techniques which also enabled different cases to be studied. During the simulation, pressure, collision rate, and potential energy were calculated to determine the equilibrium state of the assembly.

The major processing was done by storing the assembly information on tape and, with a cathode ray tube and a camera, a trace was recorded of the moving particles. The results were presented as pictorial traces of the particle system for 32 hard spheres in the solid phase, in the liquid phase, and with free boundaries; plus a 108 particle system with periodic boundaries in the liquid-vapour region. The results obtained were compared with the results from analytical theory for the same assemblies.

Generally, in these hard sphere simulations, the molecules were given equal initial kinetic energies with random velocity directions and face centred cubic lattice positions. The collision time was then calculated for all

particles, based on the velocity vectors of each potential (the collisions may be attractive or repulsive) and the time for the first particle collision to occur was then used as the time increment. The system was then advanced to this 'time' and, to increase calculation speed, a collision list was formed for which all trajectories were projected so as to order the list of particles according to their individual times to collision. This list was continuously updated as the system evolved. With this method the time step is variable and is always the time increment necessary for the next collision to occur.

The main developments in simulation techniques over this period were the use of dynamic calculations, a time step based on projected collisions, and the use of computer graphics as a method of displaying results. The limitations of both the Monte-Carlo and molecular dynamic calculations, when compared with real low temperature systems, were essentially due to the small number of particles that could be handled due to the computer memory/speed restrictions of the day. Statistically, samples were not large enough to correlate exactly with analytical solutions, even though periodic boundaries were used. Also, a long range potential could not be simulated, and an average potential was used. The application was restricted to simple real systems and to those for which perturbation theory from classical equations was adequate. Alder and Wainwright (1959) prophetically predicted that with new large memory computers, larger systems of particles could be used with an internal grid system, incorporating a method such that only adjacent particles need be checked for collisions.

2.2.2 Applications

In the 1960's many particle plasma one dimensional simulations based on classical kinetic theory were initiated. This presaged applications of simulations to the solution of the many collision-less plasma problems. Hockney and Buneman (1963) developed a fast solver for Poisson's equation, which enabled economical two dimensional electrostatic simulations to be performed. In the next several years plasma simulations in two and three dimensions were advanced, including theories for the effects of spatial grids and application to instabilities and transport in fusion plasma.

Erginsoy et al (1964) interpreted radiation damage in crystals caused by energetic elastic collisions. Rahman (1964) studied the structure of model fluids using a continuous potential similar to those of Erginsoy et al (1964). Phase changes, gas-liquid and solid-liquid, have been investigated, and considerable work has been devoted to the artificial stabilization of 'glassy' phases by 'compressor' experiments. In these latter investigations the hard sphere diameter was gradually increased with time. These controls were the first instances of deliberate alteration of the equilibrium equations of motion to satisfy desirable macroscopic constraints; the first 'non-equilibrium molecular dynamics'.

Another approach to phase equilibria was to examine systems large enough for two or three phases to co-exist, Cape and Woodcock (1980). The first dense fluid simulations in which temperature was constrained as a boundary condition were reported by Ashurst (1974). Calculations using a constant pressure tensor, energy, enthalpy, strain rate and heat-flux vectors, were not developed until the early 1980's. These

developments began with a simulation of bulk velocity, Hoover et al (1980a), (1980b) and the formulation of 'constant pressure' molecular dynamics, Andersen (1980). Shear flow simulations at constant temperature and constant energy were reported by Zwanzig (1981).

Simulation of viscous shear flows was undertaken by Ciccotti et al (1979), and Gosling et al (1973) used an external force to drive a sinusoidal shear flow. Ashurst and Hoover (1972) used reservoir regions, with constraints imposed on average velocities and temperatures, to drive the shear flow from the boundaries. Evans (1979) developed periodic deformation schemes constrained to a constant temperature or energy.

A number of couette flow simulations have been undertaken using hard spheres, Lennard-Jones particles, soft sphere mixtures, and polyatomic models of methane and chlorine; see Naitoh and Ono (1979), Heyes et al (1980), Evans and Hanley (1979), Evans (1979) and Hanley and Evans (1982) respectively. The results and calculations from some of these flows have been summarized by Evans (1981) and Hanley and Evans (1982). Quantitative studies, for both pure fluids and mixtures, have been carried out by Hanley and Evans (1980), (1981) and Hess and Hanley (1982). The flow of heat has also been simulated by Ashurst (1974) using reservoirs maintained at constant temperature.

Electrical conductivity is one of the simplest applications of linear response theory. By applying a small electrical field and comparing two neighbouring trajectories Ciccotti and Jacucci (1975) measured the conductivity of a Lennard-Jones particle, and Pollock and Alder (1980) and Watts

(1981) determined the dielectric constant for di-polar Lennard-Jones particles by non-equilibrium simulations.

In the simulation of solid phenomena, defects of various kinds have been studied. The defect generating simulations started by Erginsoy et al (1964) employ collisions of reasonably perfect crystals with incoming high energy particles. Voids in crystals, leading to stress concentration and fracture, have been the object of mostly two dimensional investigations, Hoover (1986c). He investigated the steady propagation of cracks at the speed of sound; increasing crack velocity with increasing stress, crack inertia, and crack surface irregularity. Hoover (1986b) also investigated flow and plasticity of solids, such as metals, under high strain rates using non-equilibrium molecular dynamics. Hoover (1986a) presented work carried out by Wilkins at the Lawrence Livermore National Laboratory on the dynamic compaction of powders; this simulates the combination of explosive forming and high temperature sintering using a few thousand particles.

2.3 Solid particle system simulation

Solid particle system simulation is a relatively recent development. There are two approaches to modelling solid particle systems which use different methods to approximate inter-particle interactions. Rigid particle models are based on trajectory changes resulting from instantaneous collisions due to the transference of linear and angular momentum between particles. The specified interaction parameters used in these simulations are the coefficients of friction, restitution, and angular restitution. Soft particle models generate particle movements from an inter-particle force-

displacement law. This is based on relative positions, velocities, and spins of the particles.

The soft particle simulations require a finite contact duration during which the interaction force constantly varies with displacement. The contact force is represented by particle overlap which is within the elastic limit. The time step is usually fixed and of a very small duration and thus requires a considerable number of calculation cycles for simulations of dilute systems with few collisions. One of the major advantages of the soft particle approach for the simulation of solid particle assemblies, is that all configurations, even static assemblies of particles with continuous contacts, can be simulated. The rigid particle simulations can only attempt to handle such continuous contacts by the use of complex constraints on the resulting trajectories, Lotstedt and Dahlquist (1977).

A good example of rigid particle simulations is provided by Campbell and Brennen (1982), (1985) who describe the simulation of rapid chute flows using rigid inelastic discs and periodic boundaries, with an infinite coefficient of friction between particles. Coefficients of restitution were used and two types of collision were adopted to simulate particle/particle and particle/wall interactions. The former collision type employs the condition of zero relative tangential velocity of the contact points upon departure of the collision. The latter sets the relative velocity of the centre of the particle to zero on departure whilst leaving the rotational speed unchanged. A similar rigid particle model of inelastic discs, but using a finite coefficient of friction, has been developed by Hawkins (1983).

Werner and Haff (1985) and Haff and Werner (1985) report

work on a rigid particle simulation of spherical particles confined in a three dimensional box. The system inelasticity is simulated by a coefficient of restitution, spin is neglected, and energy is supplied to the system by the use of 'hot' walls. The 'hot' wall behaves such that if a slow particle collides with a wall it leaves with a larger velocity, or a fast particle leaves with a slower velocity. The simulation was of only 27 particles, and was started using initial velocity distributions. Haff and Werner (1985) describe the adaptation of their simulation program to use concurrent processing in order to enable simulations of more particles and calculation cycles. They also adapted their program to the soft particle model for continuous contacts for two dimensional particles. Three applications were presented; the impact process in saltation, mechanical sorting by size, and transport down slopes. A two dimensional study of Eloian saltation was also reported by Werner and Haff (1986).

Solid particle simulations using soft particle interaction laws originated with the work of Cundall (1971) who developed a program to model the large scale progressive failure of systems of discrete rectangular blocks. The blocks were considered to be rigid but inter-connected by parallel linear springs and dashpots. Interface friction was also incorporated.

Application of the program to rock slope stability was presented by Cundall (1974) together with a simple example of the same simulation technique applied to a triangular pile of discs which was collapsed by reducing inter-particle friction. Further developments of the program to simulate

the quasi-static shear deformation of large assemblies of discs were reported in detail by Strack and Cundall (1978), Cundall and Strack (1979a), and the essential features of the method were described by Cundall and Strack (1979b). Cundall and Strack (1979a),(1979b) also qualitatively validated the program by simulating experiments analogous to laboratory tests performed on photoelastic disc assemblies by De Josselin de Jong and Verruijt (1969) and Oda and Konishi (1974).

Further applications of the program to the quasi-static shear deformation of disc assemblies was reported by Cundall et al (1982) and Cundall and Strack (1983). The first of these two papers discussed alternative boundary control techniques and the definition of stress and strain in particulate assemblies. Microscopic mechanisms observed in previous simulations were listed and the behaviour at large strains was also reported. The second paper considered the structural stability of particle assemblies and showed how the ensemble average stress tensor may be partitioned into different contributions due to normal forces, tangential forces, structure, and variation in normal forces at different contacts. The relevance of each partition was discussed.

Cundall (1988) reports a three dimensional version of his program BALL. A periodic cell was employed as a parallelepiped with numerical connection between opposite faces, and the system was treated as a continuum. A servo control for constant mean stress tests was introduced that adjusted the strain rate of the periodic cell. The normal force-displacement relationship was adapted such that either the linear spring-dashpot system could be used, as per Cundall and Strack (1979a), or a Hertzian contact could be modelled. For

the version using the Hertzian normal force-displacement relationship, the tangential force-displacement relationship was represented by the initial stiffness of the system, as defined by Mindlin (1949). The simulations were compared with the experiments of Ishibashi and Chen (1988) and the theoretical predictions provided by Jenkins (1988). A binary system of particles was used, and for these quasi-static shear tests mass proportional viscous damping was employed. All the following reviewed research work has been carried out using modified versions of the two dimensional program BALL.

A visco-elastic, frictional, inter-particle force model has been used by Walton (1983). Walton (1984) simulated inclined plane flows of two dimensional discs and polygonal particles. In Walton's (1984) simulation particles are described by two dimensional arbitrary polygonal soft particles. All contacts are modelled as corner interactions (point on side) and linear springs provide the elastic normal force at points of contact. Damping is velocity dependent at contact points and simulates energy absorption due to normal impacts. Tangential sliding is resisted by Coulomb type friction, i.e. a small but finite shear displacement with a linearly increasing shear force is allowed before initiation of any sliding friction.

Babic (1988) used uniform circular discs, with linear springs and dashpots for normal and tangential contacts employing a Coulomb type friction law. Once verified against the results of Cundall and Strack (1979a) three types of flow simulations were produced, hopper, couette and channel. Periodic boundaries were employed for these flow simulations

and it was possible to introduce 'rough' walls by fixing 'half particles' to the walls at specified intervals. The particular application Babic (1988) was concerned with was the flow of packed ice down rivers.

Petrakis et al (1988) adapted BALL to use a general solution to the Hertz-Mindlin contact problem. This was achieved by describing the non-linear force-displacement relationship at the particle contacts by a plasticity theory incorporating kinematic hardening. Results from various simulations were correlated to existing analytical and numerical solutions and to experiments performed on large triaxial cubical specimens. Periodic boundaries were employed to enable the simulation of large assemblies. Stability problems were encountered and it was reported that, to simulate quasi-static shear deformation, after one time step when strain was applied to the assembly, it was necessary to cycle the system with zero strain rate until the sum of the out of balance forces and moments were approximately equal to zero. Thus a very large number of cycles was needed to produce a test. Particle rotations were not permitted in any simulation reported. Results from the isotropic and anisotropic compression of 497 identical spheres were given. Also results from a binary system of 531 particles which were isotropically compressed and then loaded under biaxial compression, were reported.

Bathurst and Rothenburg (1988) employed a linear force-displacement law for normal and tangential contacts with Coulomb type friction. Two dimensional, random, isotropic assemblies of discs were generated for the tests. It was proposed that the contact orientation could be usefully approximated by a fourth order truncated Fourier series. The

calculation of the average stress tensor was presented and a relationship between the average contact force and the strain tensor illustrated, having ignored particle rotation. A stress-strain relationship was then obtained by developing equations for the average normal and tangential contact forces combined with the expressions derived for the normal and tangential inter-particle displacement components. The resulting expression for the average contact force vector was then introduced into the equation for the average stress tensor to obtain the stress-strain relationship.

It was observed that the dynamic nature of the system was such that static equilibrium could only be maintained if loading rates at the boundary were kept low enough such that the inertial forces were a fraction of the contact forces. It was also reported that to dissipate the kinetic energy of the system 'mass proportional' damping was used, without which static equilibrium could not be achieved.

Coding had been introduced into the program such that it was possible to modify the average coordination number of the assembly by searching out near contacts or deleting selected contacts in a random manner. This was equivalent to introducing small distortions in disc geometry such that inter-particle contacts could be created or lost whilst maintaining coincidence of contact normals with the lines joining disc centres. Results were presented relating the measured values of Poisson's ratio to the average coordination number and the tangential to normal contact stiffness ratio employed. An investigation of the effect of coordination number on particle rotations and the stability of an assembly was performed using an assembly of 1000 discs. It was noted that

when using assemblies with an average coordination number less than 3 the number of particles in unstable configurations was great enough to prevent the entire assembly from approaching static equilibrium within a reasonable number of calculation cycles. For assemblies with average coordination numbers close to 3 the average particle rotations were large reflecting the freedom afforded inter-particle deformations by the low system density. Conversely as the maximum average coordination number of 6 was approached the average particle rotations reduced to near zero as the particles were effectively restrained.

Ting et al (1989) used assemblies composed of discs and reproduced a number of 'standard' geotechnical tests to validate the program and obtain material aggregate properties. The force-displacement relationship used was a simple linear spring and dashpot system with Coulomb type friction. These tests comprised of one dimensional compression, simple shear and triaxial tests. Around 500 particles were used and particle rotations were suppressed to model deformable discs under load. For the triaxial tests vertical boundaries were controlled by simulating a confining membrane of finite flexibility. Erratic, low values of deviator stress were reported which were considered to be due to the limitations of two dimensional tests. However, upon inhibiting particle rotation values which were more consistent with results from soil laboratory tests were obtained.

Ting et al (1989) also demonstrated the application of the program to full-scale geotechnical problems by simulating a bearing capacity test. Centrifuge scaling laws were employed to ensure stress similitude between the simulated model test and the hypothetical full-scale problem.

Cundall's program was first used at Aston by Blackburn (1983) who restricted the applications to regular arrays of discs. Barnes (1985) extended the Aston version of the program to simulate the quasi-static shear deformation of large assemblies of different sized discs. This work was reported in a series of papers, Thornton and Barnes (1986a), (1986b), and Thornton (1987a), (1987b).

The first two papers were concerned with internal anisotropies related to contact and force distributions within particle assemblies, and stress partitioning, similar to that of Cundall and Strack (1983). Thornton and Barnes (1986b) also presented results from both a constant mean stress test and a constant volume test performed on the same initial sample configuration. It was shown that, for the two test simulations performed, the evolution of the angle of internal shearing resistance and the evolution of the induced structural anisotropy were both unique.

Thornton (1987a) reported a series of tests on a small 50 disc assembly in which the coefficient of inter-particle friction was varied from zero to 0.8. The results showed that, for this small assembly, larger inter-particle friction coefficients lead to higher strengths and stiffer assemblies. The volume change behaviour, however, was not affected by the angle of inter-particle friction provided that some inter-particle friction did exist.

Thornton (1987b) presented results from loading, unloading and reloading the same 1000 disc assembly reported by Thornton and Barnes (1986b). Internal anisotropies and energy dissipation were discussed; and implications for soil plasticity theories were also considered. Thornton and

Randall (1988) reported the incorporation of the Hertzian normal force-displacement relationship, and the laws of Mindlin and Deresiewicz (1953) to calculate the tangential force. This enabled the use of real units in the program such that it was possible to quantify particle velocities, forces, contact stresses etc. Two simulations were illustrated, one was the impact of a particle on a column of 10 identical particles, and the evolution of the force transmission through the assembly was studied. The other was the impact of a particle on a bed of 700 spheres of six different sizes, where the dynamic force transmission and particle velocity distributions were illustrated.

3.Contact Mechanics

Contact mechanics originated with Hertz (1882) who considered the case in which the forces were normal between two frictionless elastic contacting solids. Since 1950 work has been initiated into other areas of contact mechanics to study the effects of tangential and torsional loading. Applications have been extended to inelastic bodies by incorporating theories of plasticity and viscoelasticity. A comprehensive treatment of all these aspects of modern contact mechanics theory is provided by Johnson (1985). In computer simulations of solid particle systems it is possible to adopt any interaction law. However, the present research project is restricted to topologically smooth, elastic spheres incorporating inter-particle friction. It is therefore necessary to model the normal and tangential stiffnesses at the inter-particle contacts using the laws defined by Hertz (1882) and Mindlin (1949).

3.1 Normal contact stiffness

For two contacting spheres of radii $R_i (i=1,2)$, the Hertzian normal pressure distribution acting over the small circular area, radius a, is illustrated in fig 3.1a and is expressed as

$$p(r) = p_o[1-(r/a)^2]^{1/2} \quad 0 < r < a \qquad (3.1)$$

This leads to normal displacements over the contact area

$$u_i(r) = (\pi p_o(1-\nu_i^2)/4E_i a)(2a^2-r^2) \qquad (3.2)$$

where E_i and ν_i are Young's modulus and Poisson's ratio for each sphere, and (3.2) satisfies the following boundary condition for the surface of the contact area

$$u_1(r) + u_2(r) = \alpha - (1/2R^*)r^2 \qquad (3.3)$$

where

$$1/R^* = 1/R_1 + 1/R_2 \qquad (3.4)$$

and α is the relative approach of the centroids of the two spheres in contact.

Substitution of (3.2) into (3.3) for i=1,2 leads to

$$(\pi p_o/4aE^*)(2a^2-r^2) = \alpha - (1/2R^*)r^2, \qquad (3.5)$$

where

$$1/E^* = (1-\nu_1^2)/E_1 + (1-\nu_2^2)/E_2. \qquad (3.6)$$

Substituting r=0 into (3.5), the relative approach of the centroids of the spheres is

$$\alpha = \pi p_o a/2E^* \qquad (3.7)$$

and the radius of the contact area is obtained from (3.5) and (3.7) with r=a to give

$$a = \pi p_o R^*/2E^*. \qquad (3.8)$$

The total normal load is defined as

$$N = \int_0^a p(r)2\pi r dr = 2p_o\pi a^2/3 \qquad (3.9)$$

which may be substituted into (3.7) and (3.8) to give

$$a^3 = 3NR^*/4E^* \qquad (3.10)$$

and $$\alpha^3 = 9N^2/16R^*E^{*2} \qquad (3.11)$$

noting that

$$\alpha = a^2/R^* \qquad (3.12)$$

For computer implementation the normal stiffness needs to be defined. Hence, from (3.11) and (3.12)

$$N = (4E^*(R^*\alpha^3)^{1/2})/3 \qquad (3.13)$$

from which the stiffness is defined as

$$dN/d\alpha = 2E^*(R^*\alpha)^{1/2} \qquad (3.14)$$

or from (3.12)

$$dN/d\alpha = 2E^*a. \qquad (3.15)$$

When a contact is first created (3.15) cannot be used as

$a=0$. It is, therefore, necessary to use (3.13) with $N=\Delta N$, and $\alpha=\Delta\alpha$. The normal force displacement relationship given by (3.13) is illustrated in fig 3.1b.

3.2 The effect of oblique loading.

Mindlin (1949) demonstrated that for two elastic spheres in contact under a constant normal force N, the effect of applying a tangential force ($T<\mu N$) is to cause a small relative tangential motion, termed 'slip', over part of the contact area. Over the remaining part no such relative movement occurs and the surfaces are said to 'adhere' or 'stick'. The application of a tangential force initiates the formation of an annulus of slip which, upon increasing the tangential force, progresses radially inward until, when $T=\mu N$, the adhered area of contact is zero and rigid body sliding occurs. If before this state is reached the system is allowed to unload tangentially an annulus of counter-slip (slip in the opposite direction to the slip developed during the previous tangential loading) progresses radially inward from the perimeter of the contact area. The energy needed to produce the annulus of counter-slip is twice that needed to form the original slip annulus since the counter-slip has to cancel the original slip and progress slip in the opposite direction. Once the counter-slip annulus has progressed radially inward as far as the original slip annulus then the loading history of the previous loading direction is erased. The contact area merely comprises of an area of stick in the centre and the rest an annulus of slip, in the opposite sense to the original.

If the annulus of counter-slip did not fully progress to the same extent as the original slip annulus, and the tangential

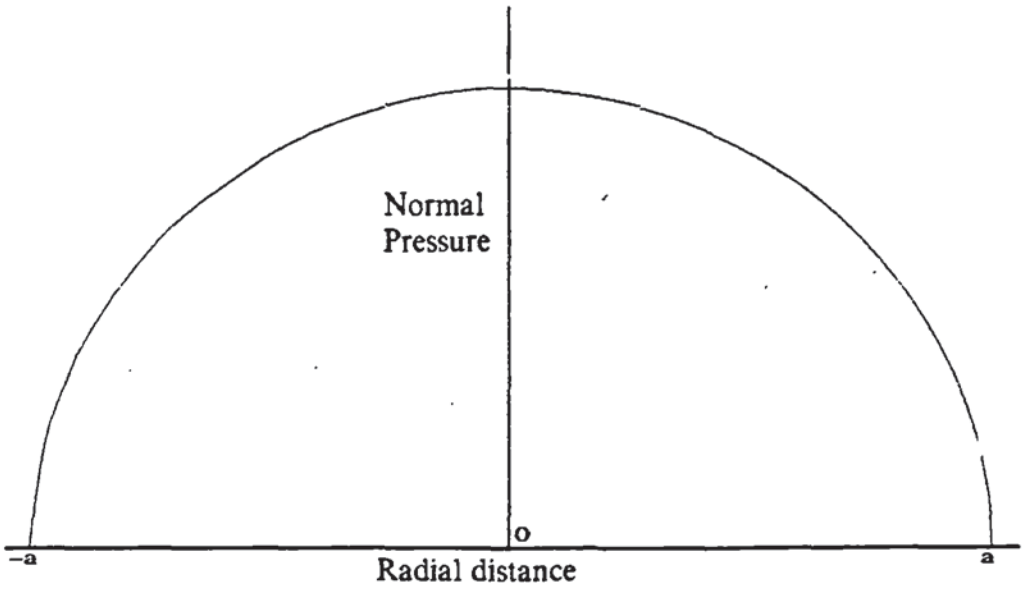

F.g 3.1a Hertzian pressure distribution.

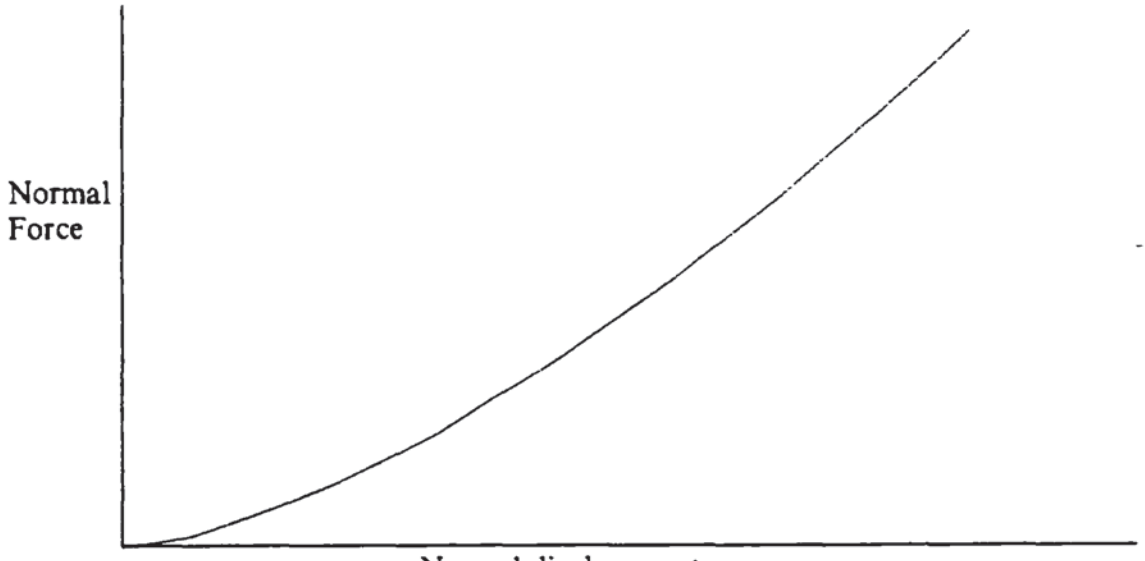

Fig 3.1b Normal force–displacement relationship.

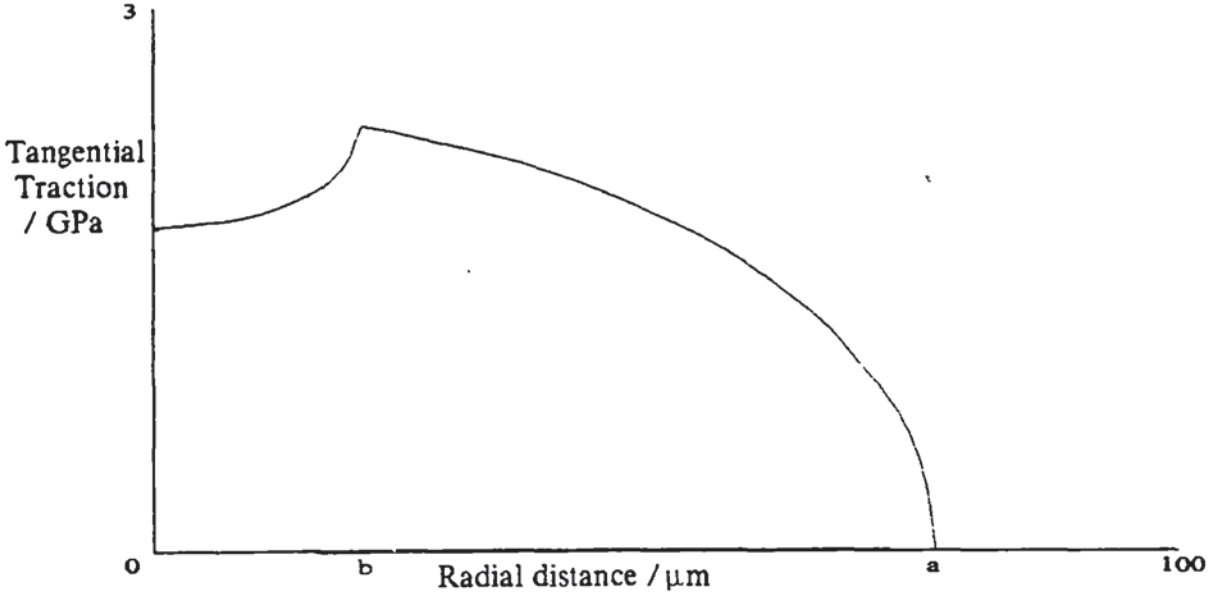

Fig 3.2 Tangential traction distribution (loading with T ⟨ μN)

loading is once more reversed, an annulus of slip in the original direction would progress radially inward. This slip annulus would also require twice the energy of formation of the virgin annulus due to the cancelling and reversal of the counter-slip annulus. Once the re-slip annulus has progressed inward as far as the counter-slip, the system will appear as though no counter-slip had ever been initiated, and any further tangential loading, in the original direction, will progress as before by radially decreasing the central remaining area of stick.

It may be noted that the theoretical tangential traction for no slip rises to an infinite value at the periphery of the contact area. In a real cohesionless system an infinite traction is impossible and thus 'micro slip' must occur at the contact edge which reduces the traction at the periphery of the contact to zero. Further points to be noted are that in the computer simulation it is necessary to consider tangential displacement rather than tangential force as the criterion for loading, unloading and reloading. This is because it is possible, as explained in section 3.5.2, for an increase in tangential force although the contact undergoes an overall negative tangential displacement.

The effect of particle rotation on the distribution of tangential traction was considered by Johnson (1982) and is illustrated in fig 3.3. The traction distribution for rigid body sliding is given by curve $\mu\sigma$. For a value of $T<\mu N$, with no relative spin of the particles, the resultant traction distribution is illustrated by curve A'. This symmetrical distribution is the resultant of curve $\mu\sigma$ and curve A. However, if there is a relative spin between the contacting particles the no-slip region is no longer centrally located

and curve A is displaced towards the leading edge of the contact. For the extreme case, when one particle is rolling over the other, the resultant traction distribution is given by curve B' which is the resultant of curve $\mu\sigma$ and curve B. Figure 3.3 demonstrates that relative spin does not affect the area under the resultant traction distribution. Hence, the magnitude of the tangential force is unaffected by relative spin and is defined by the theoretical treatment of Mindlin and Deresiewicz (1953). A consequence of the asymmetric traction distribution is that a small moment is applied to the particle. This moment is extremely small ($a<<R$) and is neglected in the computer simulation program although particle spins are permitted.

3.2.1 Tangential loading.

For the limiting condition of $T=\mu N$ the distribution of the tangential traction is given by

$$q(r) = (\mu p_o/a)(a^2-r^2)^{1/2}. \qquad 0<r<a \qquad (3.16)$$

For $T<\mu N$, the corresponding traction distribution is obtained by superimposing on (3.16) a negative traction over the adhered portion of radius $b(<a)$.

$$q(r) = -(\mu p_o/a)(b^2-r^2)^{1/2}. \qquad 0<r<b \qquad (3.17)$$

Hence the distribution of tangential traction over the total contact area, shown in fig 3.2, is

$$q = (\mu p_o/a)(a^2-r^2)^{1/2} \qquad b<r<a \qquad (3.18)$$

$$q= (\mu p_o/a)[(a^2-r^2)^{1/2} - (b^2-r^2)^{1/2}]. \qquad 0<r<b \qquad (3.19)$$

From the corresponding displacements, see Johnson (1985). Mindlin (1949) showed that the relative tangential displacement of the two spheres is

$$\delta = (3\mu N/16G^*a)(1-b^2/a^2) \qquad (3.20)$$

where

$$1/G^* = (2-\nu_1)/G_1 + (2-\nu_2)/G_2 \qquad (3.21)$$

The magnitude of the tangential force is defined as

$$T = \int_b^a 2\pi qr\,dr + \int_o^b 2\pi qr\,dr. \qquad (3.22)$$

Thus

$$T = \mu N(1-b^3/a^3), \qquad (3.23)$$

from which

$$b/a = (1-T/\mu N)^{1/3}. \qquad (3.24)$$

Thus the tangential force displacement law from (3.20) and (3.24) is

$$\delta = (3\mu N/16G^*a)[1-(1-T/\mu N)^{2/3}] \qquad (3.25)$$

from which the incremental stiffness is

$$\Delta T/\Delta\delta = 8G^*a(1-T/\mu N)^{1/3}. \qquad (3.26)$$

From (3.25) and (3.26) the initial stiffness is

$$(\Delta T/\Delta\delta)_{T=0} = 8G^*a \qquad (3.27)$$

and the tangential displacement to cause sliding δ^* is

$$\delta^* = 3\mu N/16G^*a. \qquad (3.28)$$

3.2.2 Tangential unloading.

To unload fully the two contacting spheres it is necessary to decrease the tangential force to its maximum previous value in the opposite loading direction, the counter-slip annulus has then fully penetrated and countered the original annulus of slip. Therefore the equations for the tangential tractions due to unloading are twice that of the loading case.

$$q = -2(\mu p_o/a)(a^2-r^2)^{1/2} \qquad c<r<a \qquad (3.29)$$

$$q = -2(\mu p_o/a)[(a^2-r^2)^{1/2} - (c^2-r^2)^{1/2}]. \qquad r<c \qquad (3.30)$$

Where c is the radius to which the counter-slip annulus has penetrated.

Hence the resultant tractions, i.e. the sum of the original

loading and the unloading tangential tractions, are

$$q = -(\mu p_o/a)(a^2-r^2)^{1/2} \qquad c<r<a \tag{3.31}$$

$$q = -(\mu po/a)[(a^2-r^2)^{1/2} - 2(c^2-r^2)^{1/2}] \quad b<r<c \tag{3.32}$$

$$q = -(\mu p_o/a)[(a^2-r^2)^{1/2} - 2(c^2-r^2)^{1/2} + (b^2-r^2)^{1/2}] \quad r<b \tag{3.33}$$

The tangential force is equal to the integral of q over the limits 2π and a to cover the contact surface.

$$T = \int_o^{2\pi}\int_o^a qrdrd\theta. \tag{3.34}$$

Substituting for q

$$T = (\mu N/a^3)(a^3-b^3) - (2\mu N/a^3)(a^3-c^3) \tag{3.35}$$

$$\text{but } (\mu N/a^3)(a^3-b^3) = T^*. \tag{3.36}$$

where T^* is the value of T from which unloading commenced. Hence

$$T = T^* - (2\mu N/a^3)(a^3-c^3) \tag{3.37}$$

$$\text{and } c = a[1-(T^*-T)/2\mu N]^{1/3}. \tag{3.38}$$

The relative tangential displacement δ is given by

$$\delta = (3\mu N/16G^*a)(2c^2/a^2 - b^2/a^2 - 1) \tag{3.39}$$

or, using (3.38)

$$\delta = (3\mu N/16G^*a)[2(1-(T^*-T)/2\mu N)^{2/3} - (1-T^*/\mu N)^{2/3} - 1] \tag{3.40}$$

Hence the incremental stiffness for unloading is

$$\Delta T/\Delta\delta = 8G^*a[1-(T^*-T)/2\mu N]^{1/3}. \tag{3.41}$$

The load displacement curve for a decreasing tangential force is shown in fig 3.4. If unloading is initiated from point B on the loading curve OA, then unloading occurs along BCD. The traction distribution at point C, when the tangential force is zero, is given in fig 3.5. Counter-slip progresses radially inwards until point D in fig 3.4 when $T=-T^*$ and $c=b$. The traction distribution at this point is a mirror image of that existing when $T=T^*$, and any further

decreases in T follows the virgin loading curve ODE in fig 3.4. If an oscillation of tangential force occurs between $\pm T^*$ with a constant normal force, this leads to the closed hysteresis loop shown in fig 3.4.

3.2.3 Tangential reloading.

Reloading from the point C in fig 3.6, when T=0, will initiate an annulus of slip in the original loading direction at the perimeter of the contact area which will propagate inwards cancelling and countering the counter-slip. This re-slip progresses radially inward over an annulus $d<r<a$ as shown in fig 3.7. The distribution of tangential traction during reloading is

$$q = (2\mu p_o/a)(a^2-r^2)^{1/2} \qquad d<r<a \qquad (3.42)$$

$$q = (2\mu p_o/a)[(a^2-r^2)^{1/2} - (d^2-r^2)^{1/2}]. \quad r<d \qquad (3.43)$$

Superimposing the above on the traction distribution at the start of reloading, given by (3.31) (3.32) and (3.33), we obtain

$$q = (\mu p_o/a)(a^2-r^2)^{1/2} \qquad d<r<a \qquad (3.44)$$

$$q = (\mu p_o/a)[(a^2-r^2)^{1/2} - 2(d^2-r^2)^{1/2}] \quad c<r<d \qquad (3.45)$$

$$q = (\mu p_o/a)[(a^2-r^2)^{1/2} + 2(c^2-r^2)^{1/2} - 2(d^2-r^2)^{1/2}] \quad b<r<c \qquad (3.46)$$

$$q = (\mu p_o/a)[(a^2-r^2)^{1/2} - (b^2-r^2)^{1/2} + 2(c^2-r^2)^{1/2} - 2(d^2-r^2)^{1/2}] \quad r<b \qquad (3.47)$$

Upon integration the tangential force is

$$T = \mu N(1-b^3/a^3) - 2\mu N(1-c^3/a^3) + 2\mu N(1-d^3/a^3) \qquad (3.48)$$

from which

$$d = a[1-(T-T^{**})/2\mu N]^{1/3}. \qquad (3.49)$$

where T^{**} is the tangential force from which reloading is initiated. Thus

A' - traction distribution for T for no relative spin of particles, where T < μN.
B' - traction distribution for identical T value for extreme limit of relative spin.

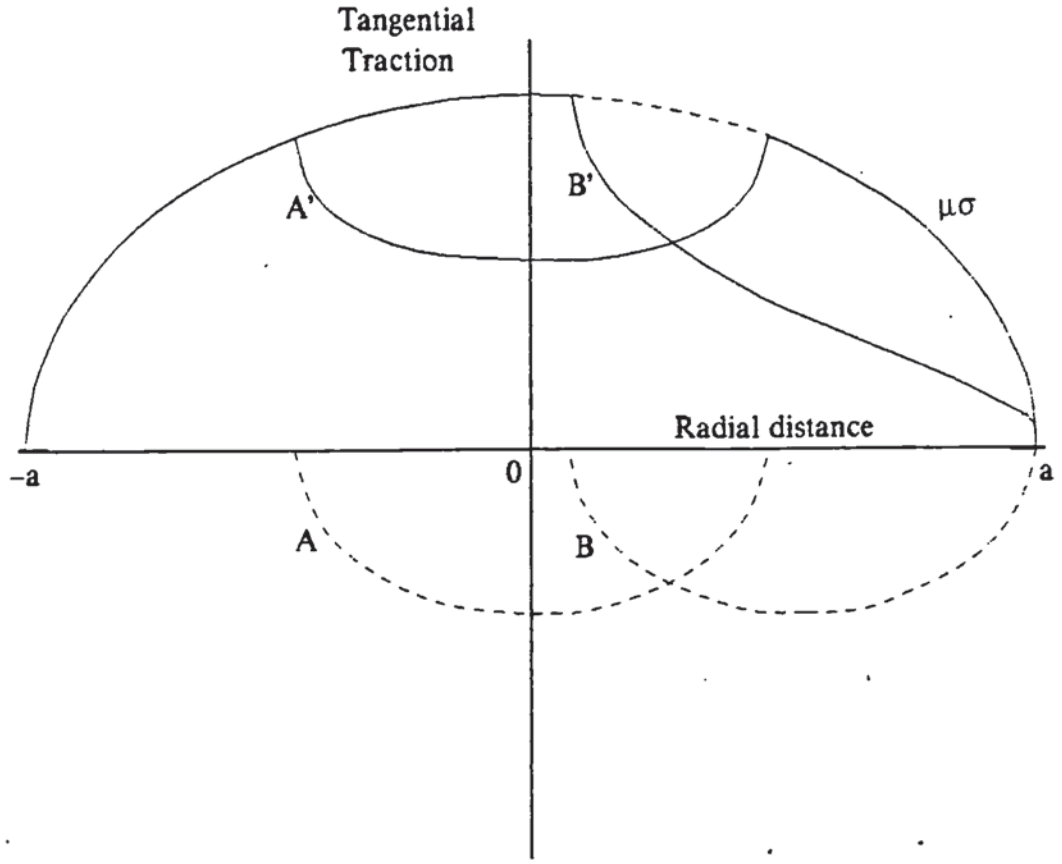

Fig 3.3 The effect of particle spin on the tangential traction distribution.

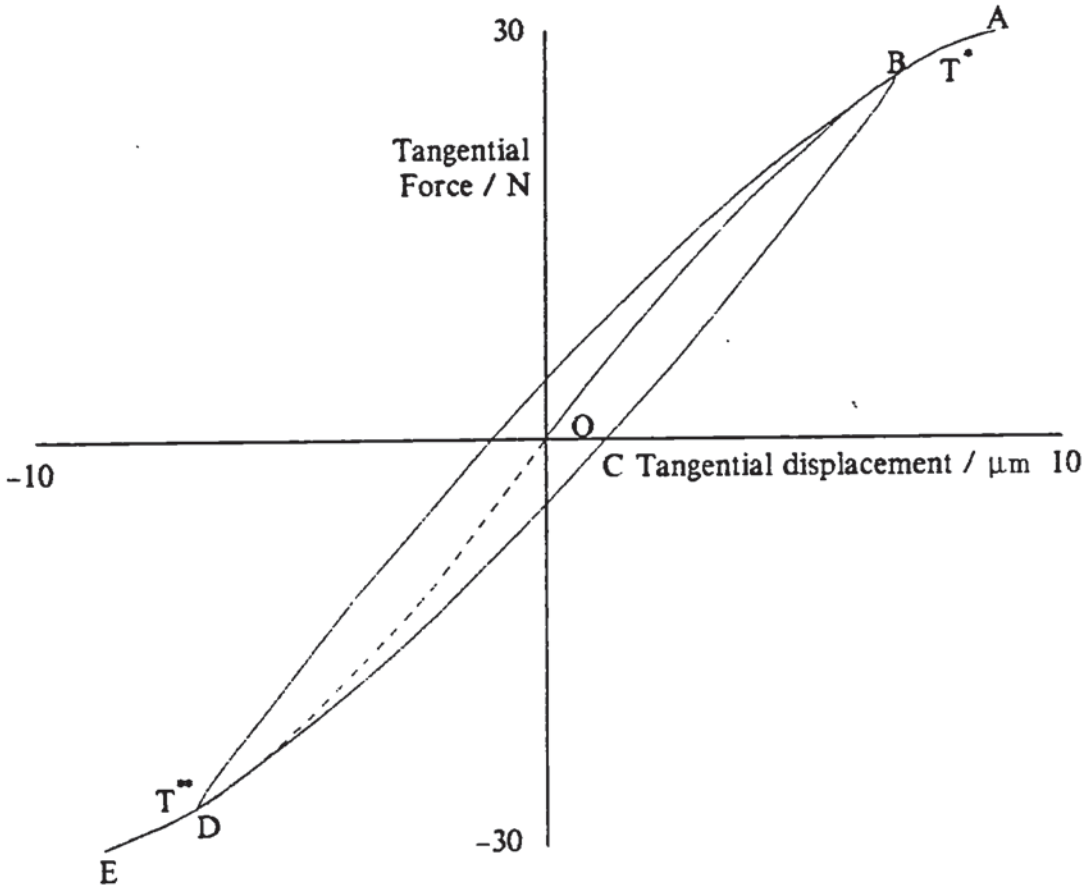

Fig. 3.4 Tangential force–displacement relationship.

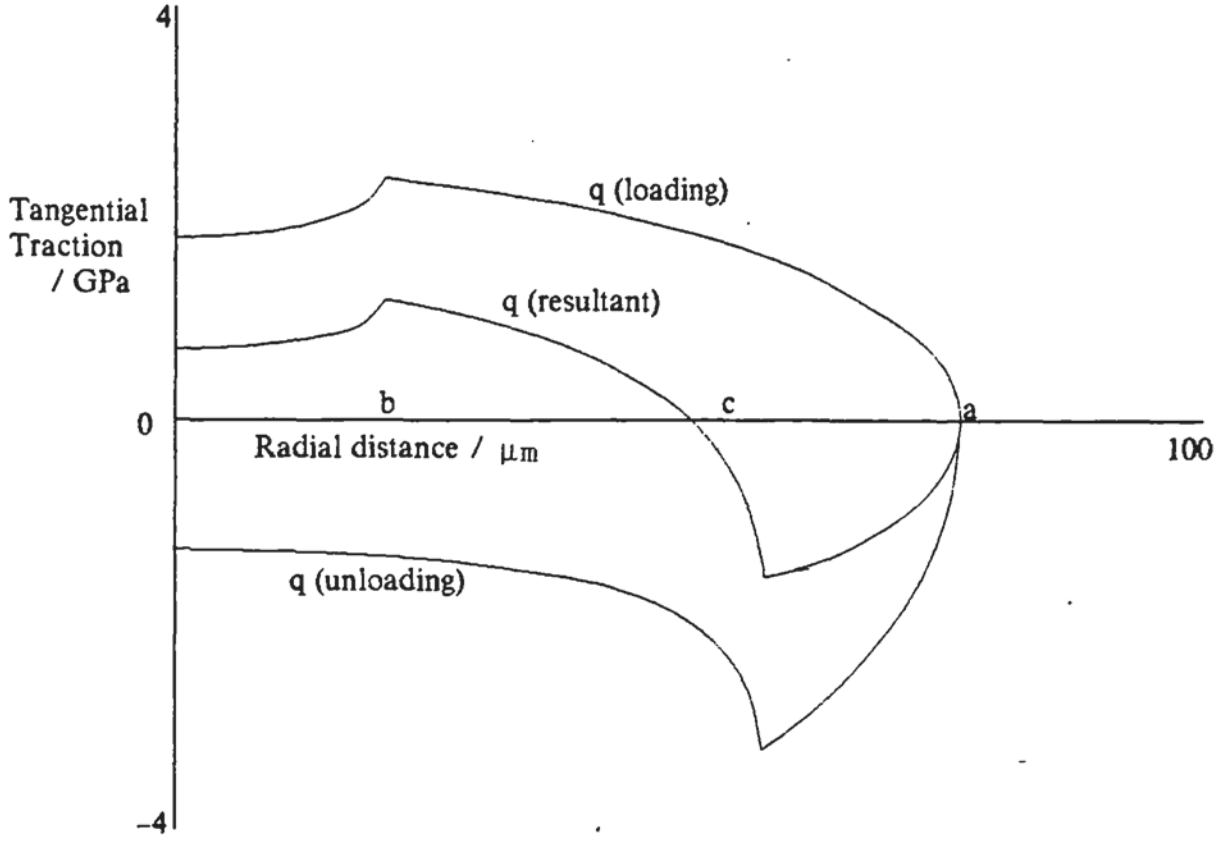

Fig. 3.5 Tangential traction distribution corresponding to point C in Fig. 3.4.

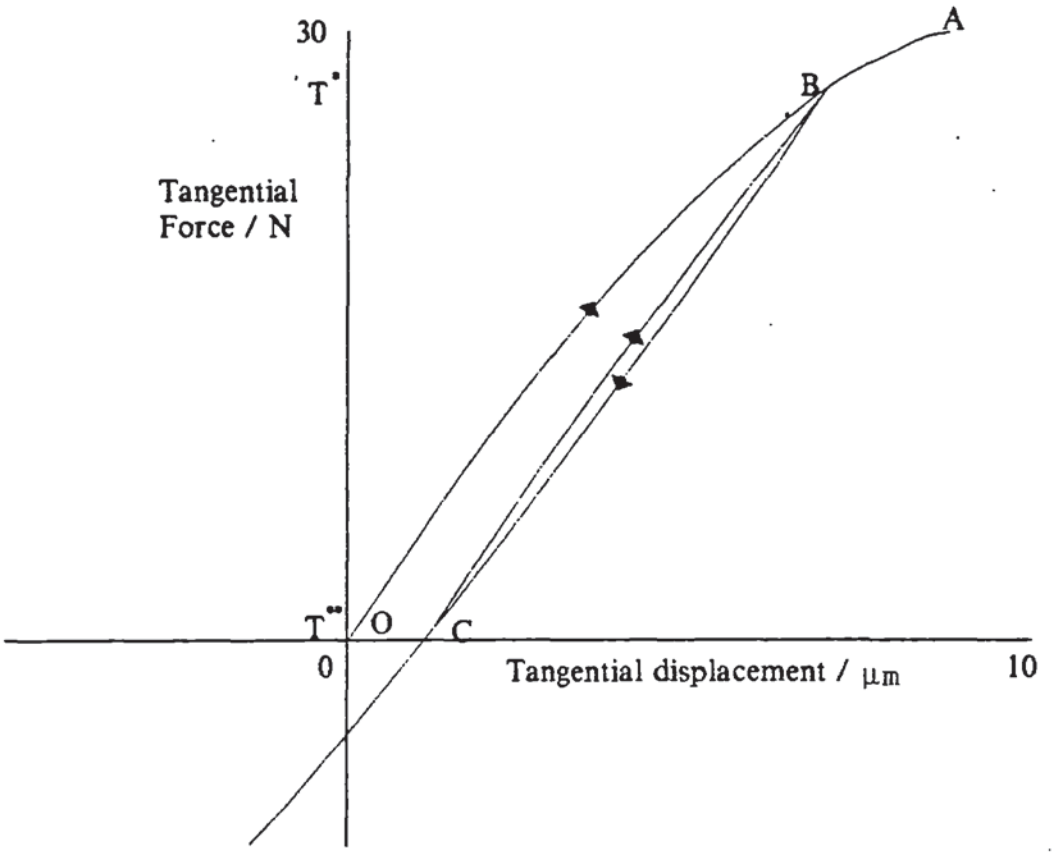

Fig. 3.6 Tangential force-displacement behaviour illustrating loading, unloading and reloading.

$$\delta = (3\mu N/16G^*a)[1 - b^2/a^2 + 2c^2/a^2 - 2d^2/a^2]. \quad (3.50)$$

Substituting (3.24),(3.38) and (3.49) and differentiating leads to the incremental equation for the stiffness.

$$\Delta T/\Delta\delta = 8G^*a[1 - (T-T^{**})/2\mu N]^{1/3}. \quad (3.51)$$

The load displacement relationship for reloading is shown in fig 3.6. When the tangential force reaches its previous maximum value, $T=T^*$, re-slip has now fully countered the counter-slip and d=c. At this point the traction distribution is that shown in fig 3.2. Consequently, further increases in T follow the virgin loading curve and the memory of the unload-reload cycle has been completely erased.

3.3 Tangential contact stiffnesses, $\Delta N=0$.

It follows from the previous sections that, for the normal force constant cases, the tangential stiffness can be defined by one equation with appropriate substitutions, i.e.

$$\Delta T/\Delta\delta = 8G^*a\theta. \quad (3.52)$$

where

$$\theta = (1-T/\mu N)^{1/3} \quad (3.53)$$

for the loading case,

$$\theta = [1-(T^*-T)/2\mu N]^{1/3} \quad (3.54)$$

for the unloading case, and

$$\theta = [1-(T-T^{**})/2\mu N]^{1/3} \quad (3.55)$$

for the reloading case.

For a contact which undergoes decreasing tangential oscillations many tangential force reversals will occur, and due to the decreasing nature of these reversals, no reversal will exceed the previous maximum or minimum tangential force. Thus the tangential force/displacement curves are described by a series of nested loops. It is impossible to foretell

how many of these reversals any contact may undergo, and to maintain the full history of the contact all reversal points would have to be stored. Since this would increase memory requirements drastically and reduce processing speed, an approximation has been introduced for the computer simulation. Only the first two reversal points are stored. Any further reversals within these two limits are treated as non-linear elastic, as indicated in fig 3.8.

3.4 Effect of increasing normal force.

The previous section established the dependency of the limiting value of the tangential force on the normal force. As a consequence there exists an infinite set of geometrically similar force-displacement curves, each corresponding to a different value of N. A theoretical investigation of the behaviour of elastic spheres in contact under varying oblique forces was presented by Mindlin and Deresiewicz (1953). Several loading histories involving variations of both normal and tangential forces were examined from which general procedural rules were identified. The procedure is to update the normal force and contact area radius followed by calculating ΔT using the new values of N and a.

3.4.1 Tangential loading.

For the case of normal force and tangential force increasing, the increasing normal force results in an increase in the contact area. If $\Delta T=\mu\Delta N$ the central area of stick will not decrease as the increase in tangential force is sufficient to enable penetration of slip into the new outer annulus of the contact area only. If $\Delta T>\mu\Delta N$ then not only is the new outer annulus fully penetrated but the inner annulus

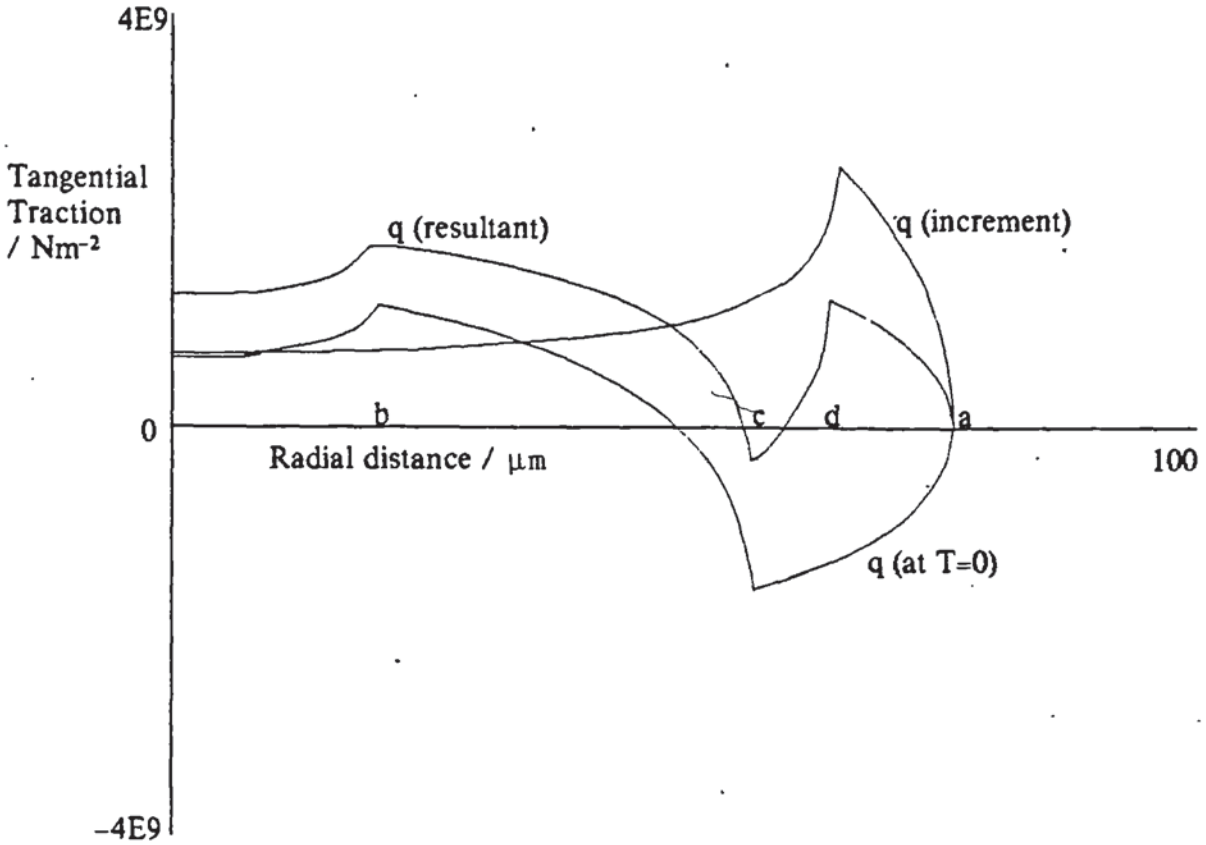

Fig. 3.7 Tangential traction distribution.

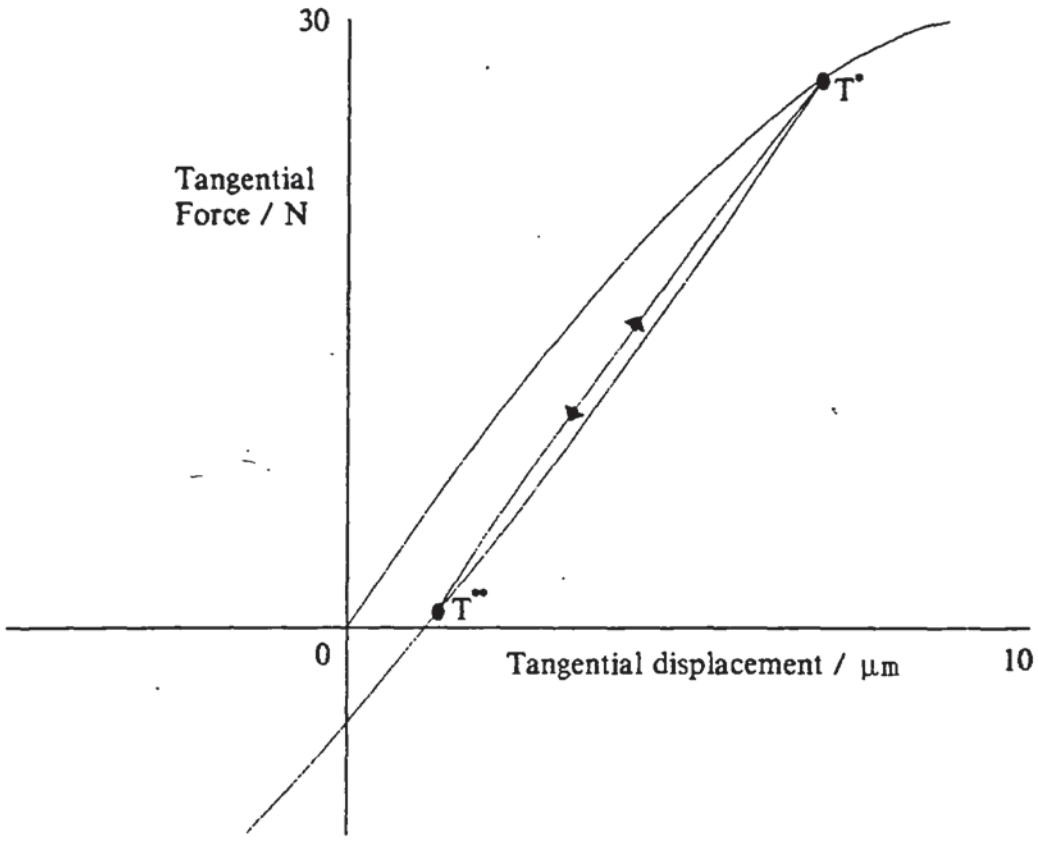

Fig. 3.8 Tangential force-displacement behaviour.

of stick is decreased, thus progressing the system to failure. For $\Delta T<\mu\Delta N$ the increase in tangential force is not sufficient to penetrate the new outer annulus of stick and thus the contact area forms four annuli, a central area of stick, surrounded by an annulus of high traction (which was an annulus of slip with the previous lower normal force), surrounded by a stick annulus with an annulus of slip on the outside. Thus progression of the slip annulus into the central annulus of stick can not occur until any outer annuli of high traction, have first been loaded to form annuli of slip in the current loading direction and any outer annuli of stick have been penetrated.

Figure 3.9 shows two typical loading curves corresponding to a normal force of N and (N+ΔN). Consider an initial state (T,N) given by point A in fig.3.9. The corresponding tangential traction distribution q over the contact area of radius a is shown in fig.3.10. If, in the next time increment, both N and T increase then the solution depends upon the ratio $\Delta T/\Delta N$.

Consider the case $\Delta T = \mu\Delta N$. The increase in normal force will result in a larger contact area of radius a_1, defined by

$$a_1^3 = 3(N+\Delta N)\, R^*/4E^*. \qquad (3.56)$$

If T is now increased this will initiate slip at $r=a_1$. The increment in tangential traction Δq is given by

$$\Delta q = (\mu(p_o + \Delta p_o)/a_1)(a_1^2 - r^2)^{1/2} \qquad c_1 <= r <= a_1 \qquad (3.57)$$

$$\Delta q = (\mu(p_o + \Delta p_o)/a_1)[(a_1^2 - r^2)^{1/2} - (c_1^2 - r^2)^{1/2}] \qquad o<=r<=c_1 \qquad (3.58)$$

It follows from (3.24) that

$$c_1^3 = a_1^3\,[1 - \Delta T/\mu(N+\Delta N)] \qquad (3.59)$$

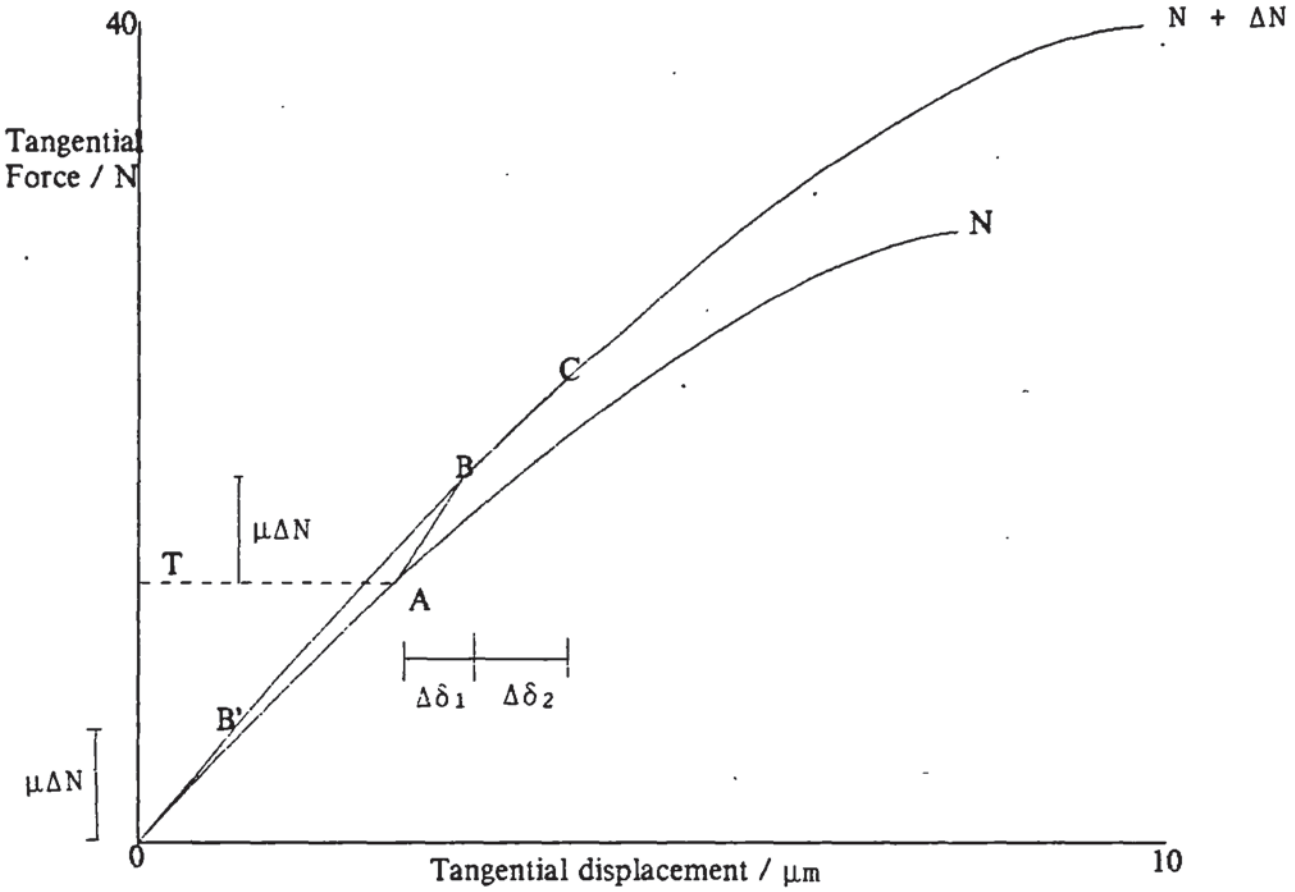

Fig. 3.9 Tangential force-displacement behaviour.

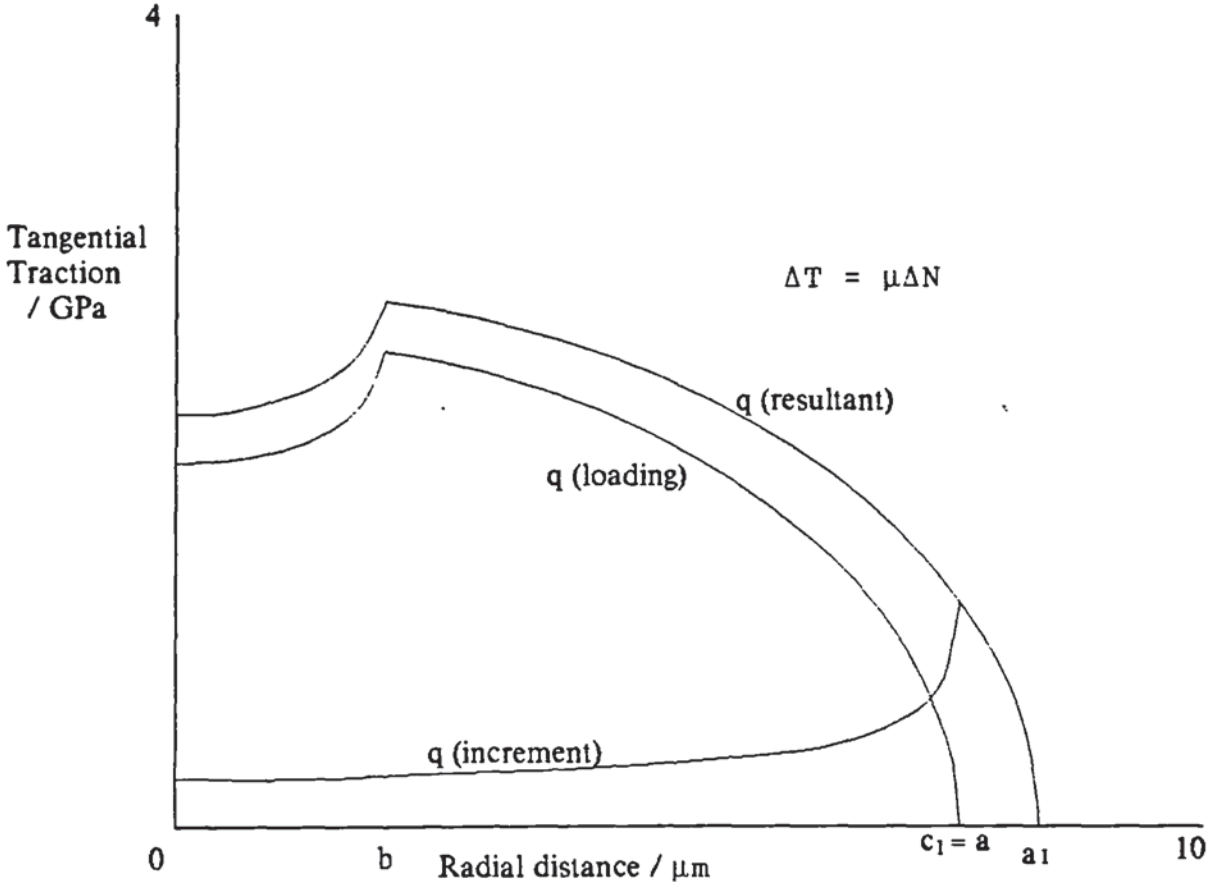

Fig. 3.10 Tangential traction distribution.

and from (3.10) and (3.56)

$$a^3(N + \Delta N) = a_1{}^3 N, \qquad (3.60)$$

thus

$$c_1{}^3 = a^3(\mu N + \mu\Delta N - \Delta T)/\mu N. \qquad (3.61)$$

It is clear from (3.61) that if $\Delta T = \mu\Delta N$ then $c_1 = a$ and hence, combining (3.57) and (3.58) with (3.18) and (3.19), the resultant traction q_R is

$$q_R = (\mu(p_o + \Delta p_o)/a_1)(a_1{}^2 - r^2)^{1/2} \qquad b <= r <= a_1 \qquad (3.62)$$

$$q_R = (\mu(p_o + \Delta p_o)/a_1)[(a_1{}^2 - r^2)^{1/2} - (b^2 - r^2)^{1/2}] \qquad o <= r <= b \qquad (3.63)$$

The tractions q, Δq and q_R, defined above, are illustrated in fig 3.10 from which it can be seen that there has been no further penetration of the stick region, and that the resultant tangential traction distribution is exactly the same as would have been obtained by applying a tangential force $(T+\mu\Delta N)$ with the normal force constant at $(N+\Delta N)$. This corresponds to point B in fig 3.9.

Since the normal force and contact area are increased prior to increasing T to T + ΔT, the load displacement curve AB is identical to the curve OB' shown in fig 3.9. It therefore follows from (3.26) that the incremental stiffness is

$$\Delta T/\Delta\delta = 8G^* a_1 \qquad (3.64)$$

Hence, considering ΔN and ΔT to be small, the displacement increment necessary to move from A to B in fig 3.9 is given by

$$\Delta\delta_1 = (1/8G^* a_1)\mu\Delta N. \qquad (3.65)$$

If $\Delta T > \mu\Delta N$ then there will be an additional displacement increment $\Delta\delta_2$ necessary to advance along the curve corresponding to the new value of N (to point C for example in fig 3.9). This displacement increment is defined by modifying

and from (3.10) and (3.56)

$$a^3(N + \Delta N) = a_1^3 N, \qquad (3.60)$$

thus

$$c_1^3 = a^3(\mu N + \mu\Delta N - \Delta T)/\mu N. \qquad (3.61)$$

It is clear from (3.61) that if $\Delta T = \mu\Delta N$ then $c_1 = a$ and hence, combining (3.57) and (3.58) with (3.18) and (3.19), the resultant traction q_R is

$$q_R = (\mu(p_o + \Delta p_o)/a_1)(a_1^2 - r^2)^{1/2} \qquad b <= r <= a_1 \qquad (3.62)$$

$$q_R = (\mu(p_o + \Delta p_o)/a_1)[(a_1^2 - r^2)^{1/2} - (b^2 - r^2)^{1/2}] \qquad o <= r <= b \qquad (3.63)$$

The tractions q, Δq and q_R, defined above, are illustrated in fig 3.10 from which it can be seen that there has been no further penetration of the stick region, and that the resultant tangential traction distribution is exactly the same as would have been obtained by applying a tangential force $(T+\mu\Delta N)$ with the normal force constant at $(N+\Delta N)$. This corresponds to point B in fig 3.9.

Since the normal force and contact area are increased prior to increasing T to T + ΔT, the load displacement curve AB is identical to the curve OB' shown in fig 3.9. It therefore follows from (3.26) that the incremental stiffness is

$$\Delta T/\Delta\delta = 8G^* a_1 \qquad (3.64)$$

Hence, considering ΔN and ΔT to be small, the displacement increment necessary to move from A to B in fig 3.9 is given by

$$\Delta\delta_1 = (1/8G^* a_1)\mu\Delta N. \qquad (3.65)$$

If $\Delta T > \mu\Delta N$ then there will be an additional displacement increment $\Delta\delta_2$ necessary to advance along the curve corresponding to the new value of N (to point C for example in fig 3.9). This displacement increment is defined by modifying

(3.26) to give

$$\Delta\delta_2 = (1/8G^*a_1)\,[1-(T + \mu\Delta N)/\mu(N + \Delta N)]^{-1/3}(\Delta T - \mu\Delta N) \quad (3.66)$$

Hence, for $\Delta T >= \mu\Delta N$ the total displacement increment is

$$\Delta\delta = (1/8G^*a_1)\,\{\mu\Delta N + (\Delta T - \mu\Delta N)[1-(T + \mu\Delta N)/\mu(N + \Delta N)]^{-1/3}\} \quad (3.67)$$

Rearranging to obtain the tangential force increment

$$\Delta T = 8G^*a\,\theta\Delta\delta + \mu\Delta N(1-\theta) \quad (3.68)$$

where

$$\theta = [1- (T + \mu\Delta N)/\mu N]^{1/3} \quad (3.69)$$

and the values of a and N have been updated.

For the case of $\Delta T>\mu\Delta N$ in terms of the traction diagrams for the increment of ΔT_2, where $\Delta T_2 = \Delta T - \mu\Delta N$ slip is now initiated not from the periphery of contact, as this is already under the influence of slip, but from point c, the limit of the stick annulus. Fig 3.11 illustrates Δq_1 for $\Delta T = \mu\Delta N$ and Δq_2 for ΔT_2 with q_R the resultant traction.

If $\Delta T<\mu\Delta N$ it follows from (3.61) that $c_1 > a$ and the initial, incremental and resultant tangential tractions are as shown in fig 3.12. It also follows from (3.64) that $\Delta\delta < \Delta\delta_1$ and is therefore insufficient to reach point B in fig 3.9. This leads to a problem in that the new state (T,δ) does not lie on the curve corresponding to the new value of N. This situation could be repeated a number of times before the next increment in T is sufficient to bring the state (T,δ) onto the appropriate curve.

The case of $\Delta T< \mu\Delta N$ has been considered analytically by Szalwinski (1985). However, for computer implementation it is considered sufficient to use the following incremental approach. If $\Delta T<\mu\Delta N$ then the incremental stiffness is given by

$$\Delta T/\Delta\delta = 8G^*a \quad (3.70)$$

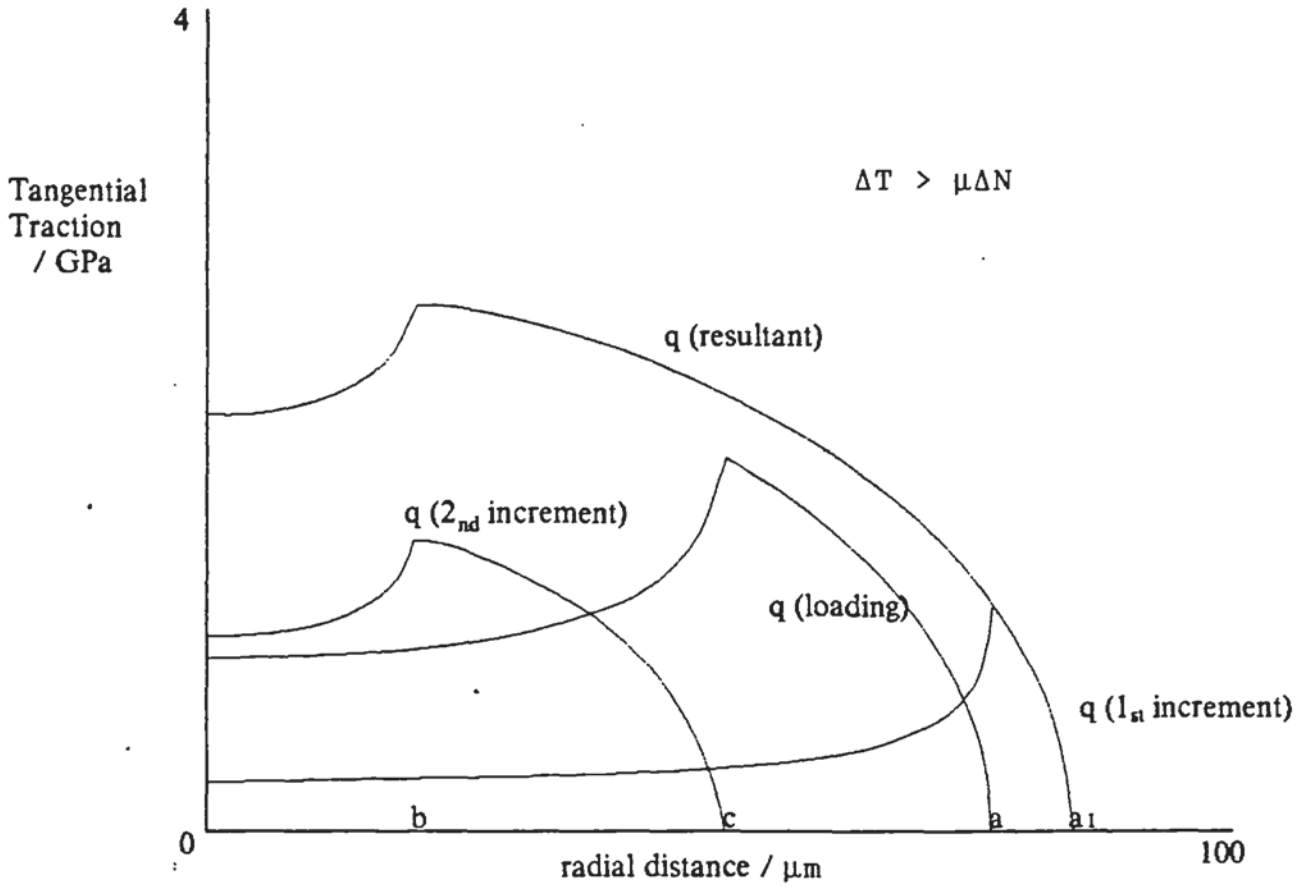

Fig. 3.11 Tangential traction distribution.

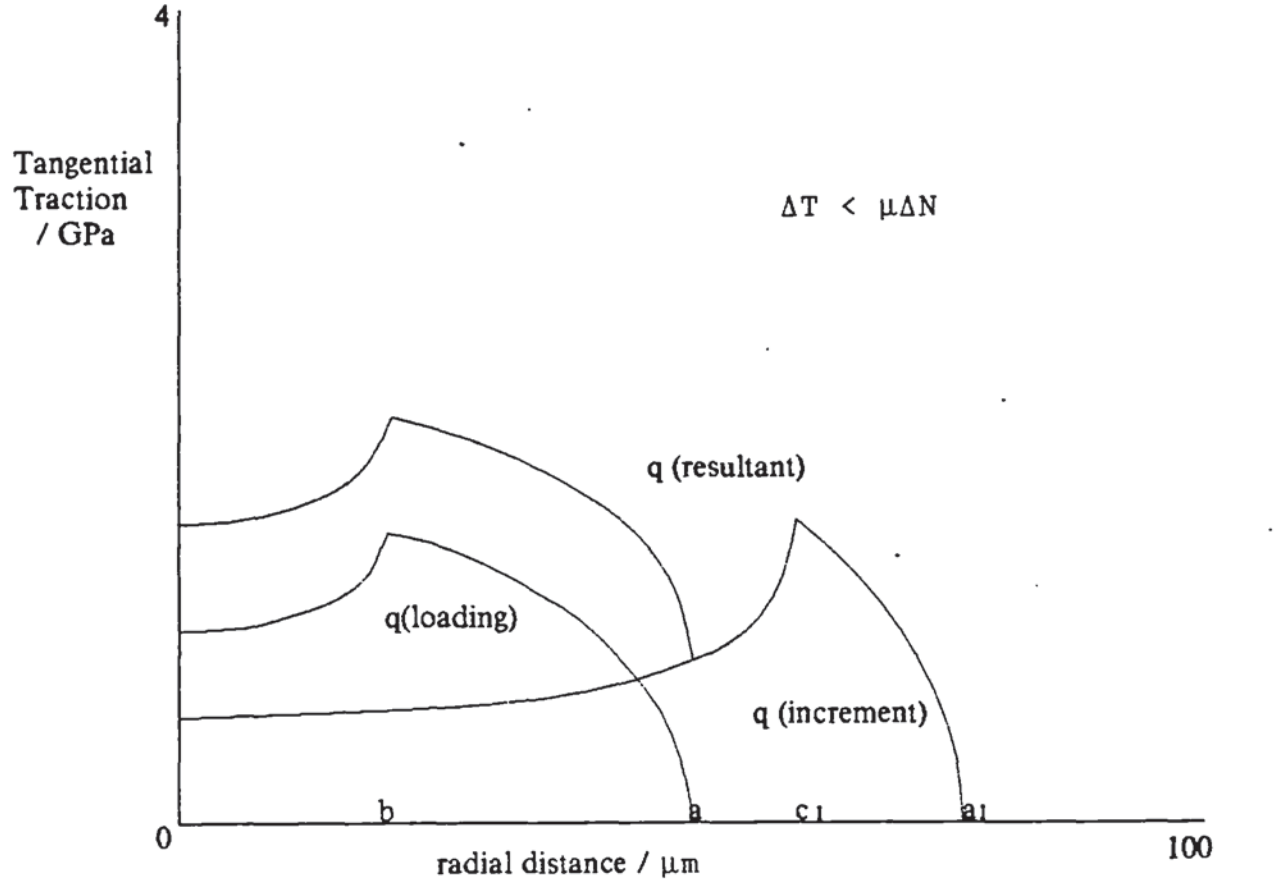

Fig. 3.12 Tangential traction distribution.

using the new value of a. This equation is then used for subsequent time increments until the condition

$$\Sigma\Delta T >= \mu\Sigma\Delta N \qquad (3.71)$$

is reached. When (3.71) is true the new state falls on the corresponding normal force constant curve and (3.68) is used.

3.4.2 Tangential unloading.

Upon tangential load reversal the annulus of counter-slip when progressing radially inwards will first encounter the outer annulus of stick, caused by the increase in normal force, which it will have to penetrate. If the tangential force decrement is large enough ($>\mu|\Delta N|$), it will also have to penetrate and counter the inner annulus of high traction. Thus with increasing contact area there is always an annulus of stick on the outside of the contact area that any tangential loading will have to penetrate before it can reach the previous high traction annuli or stick annuli to either counter or extend slip inwards.

Consider a history in which a normal force N is applied and then, keeping N constant, a monotonically increasing tangential displacement is applied until $T = T^*$, after which the tangential displacement is reversed and the tangential force reduces to $T<T^*$, given by point A on the curve OT*A in fig.3.13. The traction q, in fig 3.14, acting over the area of radius a corresponds to point A in fig 3.13.

If, during the next time increment, there is a further reduction in tangential displacement plus an increase in normal force the solution once more depends on the ratio $|\Delta T|/|\Delta N|$. For the case $|\Delta T| = \mu|\Delta N|$ it follows from the arguments presented in Section 3.4.1 that the incremental

traction Δq and the resultant traction q_R are as shown in fig 3.14. Similarly the new state is given by point B on the unloading curve corresponding to $N+\Delta N$, as shown in fig 3.13. Hence the displacement increment necessary to move from A to B is

$$\Delta\delta_1 = -(1/8G^*a)\mu\Delta N \qquad (3.72)$$

It also follows from section 3.4.1 that for $|\Delta T|>\mu|\Delta N|$ the additional displacement increment necessary to advance along the unloading curve corresponding to $N+\Delta N$, point C in fig 3.13, is obtained by modifying (3.41) to give

$$\Delta\delta_2 = (1/8G^*a)[1-(T^*-T+2\mu\Delta N)/2\mu N]^{-1/3}(\Delta T+\mu\Delta N) \qquad (3.73)$$

and hence, for $|\Delta T|>=\mu|\Delta N|$, the total displacement increment is

$$\Delta\delta = (1/8G^*a)\{-\mu\Delta N+(\Delta T+\mu\Delta N)[1-(T^*-T+2\mu\Delta N)/2\mu N]^{-1/3}\} \qquad (3.74)$$

where a and N are the updated values.

Therefore, by rearranging (3.74), we obtain

$$\Delta T=8G^*a\theta\Delta\delta-\mu\Delta N(1-\theta) \qquad (3.75)$$

where

$$\theta=[1-(T^*-T+2\mu\Delta N)/2\mu N]^{1/3}. \qquad (3.76)$$

The case of $|\Delta T|<\mu|\Delta N|$ for unloading results in the same problems as for loading and is dealt with in a similar manner. If $|\Delta T|<\mu|\Delta N|$ then the incremental stiffness is given by (3.70) until the following condition is satisfied

$$\Sigma|\Delta T|>=\mu\Sigma|\Delta N| \qquad (3.77)$$

3.4.3 Tangential reloading.

Figure 3.15 shows two force displacement curves corresponding to constant normal forces of N and $N+\Delta N$. The figure illustrates how the corresponding unload-reload cycles 'nest' within each other. If the current state is given by point A then, from the arguments presented in the previous

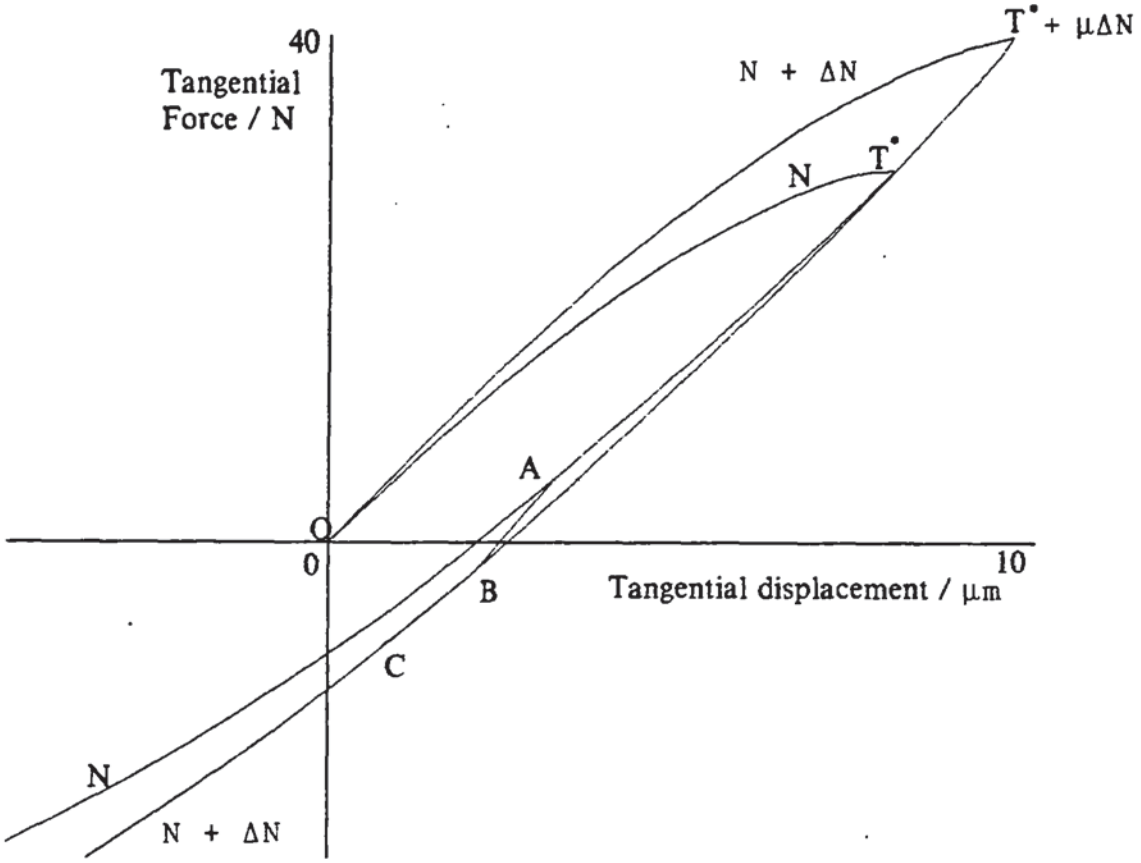

Fig. 3.13 Tangential force–displacement behaviour.

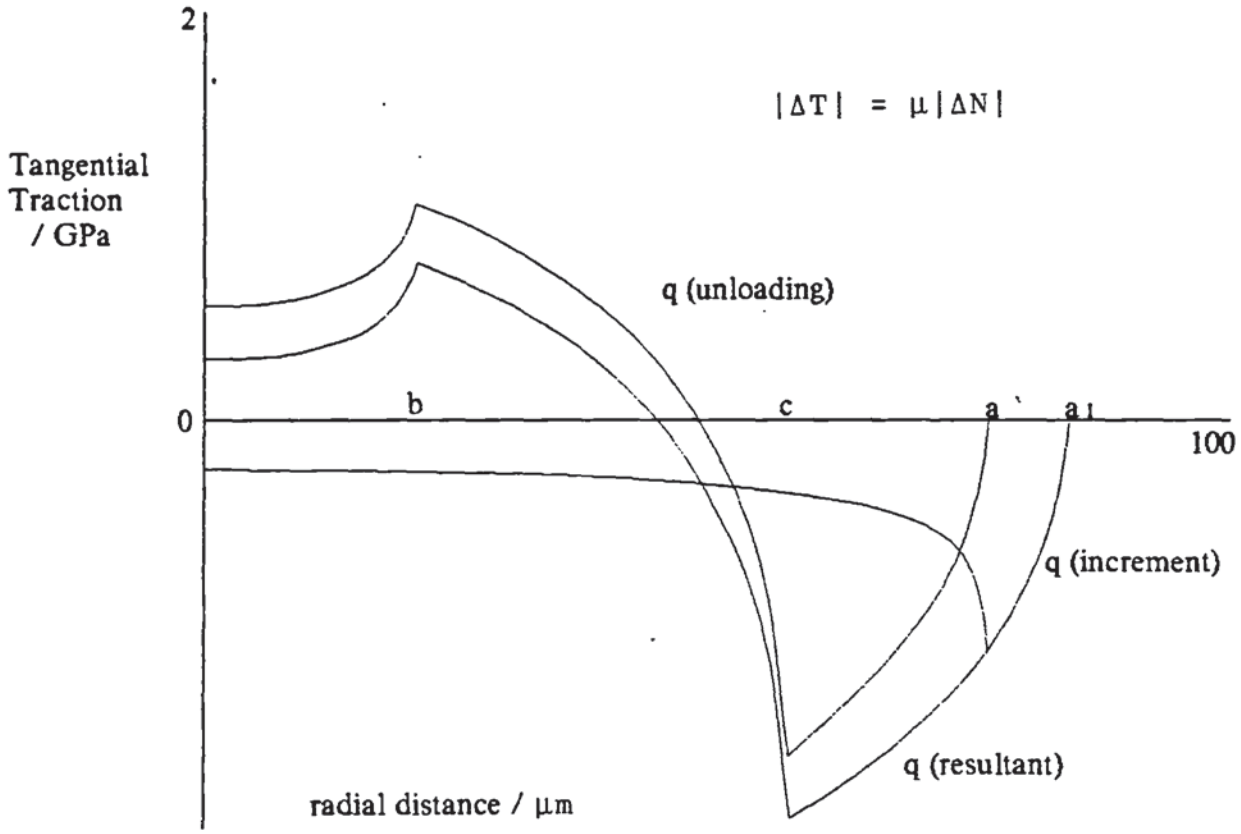

Fig. 3.14 Tangential traction distribution.

two sections, if $\Delta N>0$ then the solution for ΔT depends on the ratio $\Delta T/\Delta N$. The procedure is similar to the case for initial loading. For $\Delta T>=\mu\Delta N$ the total tangential displacement is

$$\Delta\delta = \Delta\delta_1+\Delta\delta_2 \qquad (3.78)$$

where $\Delta\delta_1$ is given by (3.65) and $\Delta\delta_2$ is obtained by modifying (3.51)

$$\Delta\delta_2=(1/8G^*a)[1-(T-T^{**}+2\mu\Delta N)/2\mu N]^{-1/3}(\Delta T-\mu\Delta N) \qquad (3.79)$$

where T^{**} is defined in fig 3.8. Hence

$$\Delta\delta=(1/8G^*a)\{\mu\Delta N+(\Delta T-\mu\Delta N)[1-(T-T^{**}+2\mu\Delta N)/2\mu N]^{-1/3}\} \qquad (3.80)$$

which may be rearranged to give

$$\Delta T=8G^*a\theta\Delta\delta+\mu\Delta N(1-\theta) \qquad (3.81)$$

where

$$\theta=[1-(T-T^{**}+2\mu\Delta N)/2\mu N]^{-1/3}. \qquad (3.82)$$

For $\Delta T<\mu\Delta N$ as in the loading case, (3.70) is used until the condition given by (3.71) is reached.

3.5 Effect of decreasing normal force.

If the normal force decreases the contact area decreases. However, before the contact area can be reduced it is necessary to relocate the slip annulus. Mindlin and Deresiewicz (1953) suggested the following procedure- i) freeze the contact area of radius a, ii) free the annulus $a_1<r<a$ of tangential traction, iii) unfreeze the contact area. It is important to note that in the remainder of this section ΔN is implicitly negative and is not taken to be an absolute value as in the paper by Mindlin and Deresiewicz (1953).

3.5.1 Tangential loading.

Figure 3.16 illustrates two typical loading curves corresponding to a normal force of N and (N+ΔN). For an initial state (T,N), described by point A in fig 3.16, the corres-

ponding tangential traction distribution q over the contact area of radius a, where the annulus of slip has penetrated to c, is illustrated in fig 3.17. The decrease in normal force results in a decrease in contact area to a_1, defined by equation (3.56), illustrated by q_{R1}. The traction Δq_1 present over the annulus $a_1 < r < a$ must be removed before a reduction in the contact area to a_1 can occur, this is achieved by redistributing the traction Δq_1 over the area $0 < c$ thus reducing the central annulus of stick.

$$\Delta q_1 = -(\mu p_0/a)(a^2-r^2)^{1/2} \quad a_1 <= r <= a \tag{3.83}$$

$$\Delta q_1 = -(\mu p_0/a)[(a^2-r^2)^{1/2} - (a_1^2-r^2)^{1/2}]. \quad 0 <= r <= a_1 \tag{3.84}$$

Where the redistributed traction penetrates the remaining area of stick $r < c$ to point c_1, fig 3.17, where

$$c_1^3 = a_1^3(1-T/\mu(N+\Delta N)) \tag{3.85}$$

and the traction Δq_1 is distributed in the form Δq_2 over the remaining contact area where

$$\Delta q_2 = (\mu(p_0+\Delta p_0)/c)(c^2-r^2)^{1/2} \quad c_1 <= r <= c \tag{3.86}$$

$$\Delta q_2 = (\mu(p_0+\Delta p_0)/c)[(c^2-r^2)^{1/2} - (c_1^2-r^2)^{1/2}] \quad 0 <= r <= c_1 \tag{3.87}$$

Where $|\Delta q_1| = |\Delta q_2|$

The traction distribution is now represented by q_{R2} in fig 3.17 where

$$q_{R2} = (\mu(p_0+\Delta p_0)/a_1)(a_1^2-r^2)^{1/2} \quad c_1 <= r <= a_1 \tag{3.88}$$

$$q_{R2} = (\mu(p_0+\Delta p_0)/a_1)[(a_1^2-r^2)^{1/2} - (c_1^2-r^2)^{1/2}] \quad 0 <= r <= c_1 \tag{3.89}$$

This distribution corresponds to point C in fig 3.16. If T is increased this will initiate slip at $r=c_1$ where c_1 is the point at which the slip annulus has reached due to the distribution of the tangential traction over the smaller contact area. Slip will thus penetrate to point b on fig

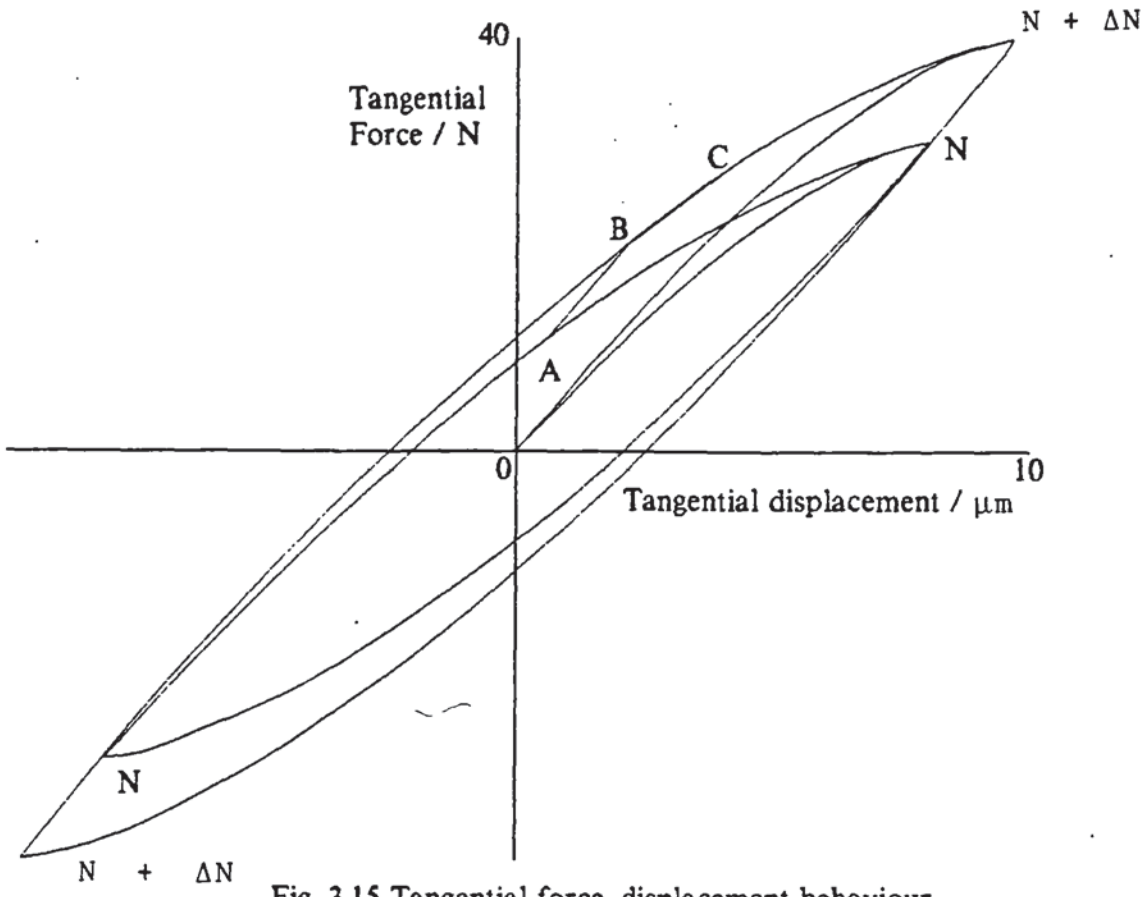

Fig. 3.15 Tangential force–displacement behaviour.

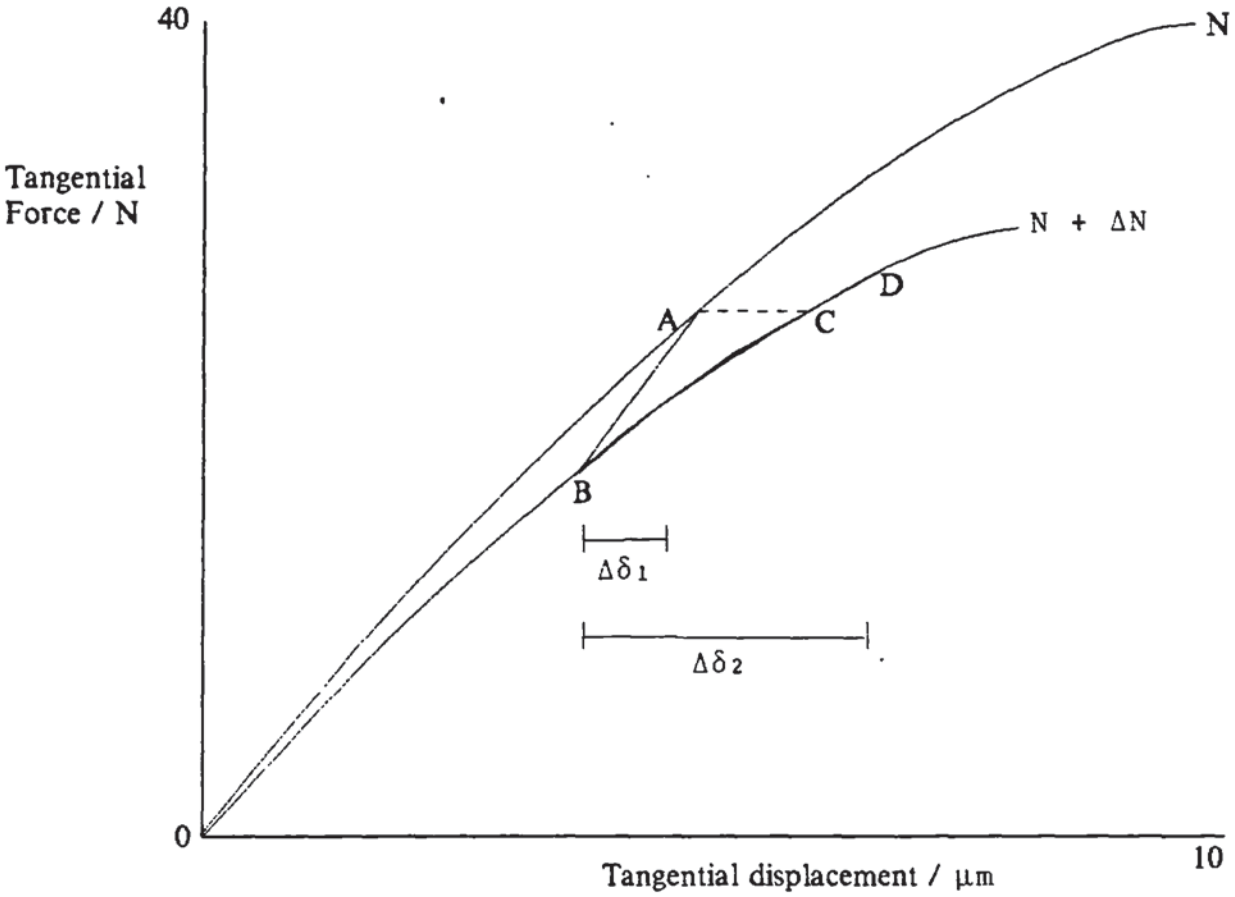

Fig. 3.16 Tangential force–displacement behaviour.

3.17 where the traction increment is

$$\Delta q_3 = (\mu(p_0+\Delta p_0)/c_1)(c_1^2-r^2)^{1/2} \qquad b<=r<=c_1 \qquad (3.90)$$

$$\Delta q_3 = (\mu(p_0+\Delta p_0)/c_1)[(c_1^2-r^2)^{1/2} - (b^2-r^2)^{1/2}] \quad 0<=r<=b \qquad (3.91)$$

where b is defined by equation (3.61). The resultant traction is

$$q_{R3} = (\mu(p_0+\Delta p_0)/a_1)(a_1-r)^{1/2} \qquad b<=r<=a_1 \qquad (3.92)$$

$$q_{R3} = (\mu(p_0+\Delta p_0)/a_1)[(a_1^2-r^2)^{1/2} - (b^2-r^2)^{1/2}] \quad 0<=r<=b \qquad (3.93)$$

The tractions q, Δq_1, q_{R1}, Δq_2, q_{R2}, Δq_3 and q_{R2}, as defined above, are shown in fig 3.17. From which it can be seen that when the normal force decreases it is necessary to redistribute the existing traction over the smaller contact area, and as such even if there was no increase in tangential force it can be seen that the slip annulus has further penetrated the contact area and thus progressed the contact towards rigid body sliding. The resultant traction distribution is exactly the same as would have been obtained by applying a tangential force (T+ΔT) with the normal force constant at (N+ΔN), corresponding to point D in fig 3.16.
As with previous sections, for small ΔT and ΔN the displacement increment necessary to move from A to B in fig 3.16 is given by equation (3.65). The situation of $|T|<\mu|\Delta N|$ which can occur on normal force increasing can not occur with normal force decreasing. This is due to the removal and redistribution of traction over the reduced contact area which causes a displacement increment that brings the state to point C in fig 3.16. An increase in tangential force would cause a displacement as defined by equation (3.66), leading to, for example, point D in fig 3.16. The total displacement increment is thus given by equation (3.67).

Hence, the tangential force increment and definition of θ are defined by equations (3.68) and (3.69), remembering that ΔN is implicitly negative.

3.5.2 Tangential unloading.

Consider a loading history corresponding to the curve OT*A shown in fig. 3.18. If, during the next time step, there is a further decrease in tangential force accompanied by a decrease in normal force then it follows from the arguments presented in sections 3.5.1 that the load-displacement behaviour will follow the hypothetical curve ABCD. Allowing for the implied negative value of ΔN, it follows from the previous sections that equations (3.72), (3.73) and (3.74) apply, and that the increment in tangential force and θ are defined by (3.75) and (3.76) respectively.

3.5.3 Tangential reloading.

Figure 3.19 illustrates two force displacement curves for two constant normal forces of N and $N+\Delta N$. The initial state is represented by point A, and for no increment of ΔT, upon reduction of normal force the resultant state is defined by point C. It follows from section 3.5.1 and section 3.4.3 that the tangential displacement between point A and point D is defined by equation (3.80) and thus the increment in tangential force and θ by equation (3.81) and (3.82) respectively.

3.6 General Solution.

From the previous sections in this chapter it can be seen that one general equation can be used for all cases.

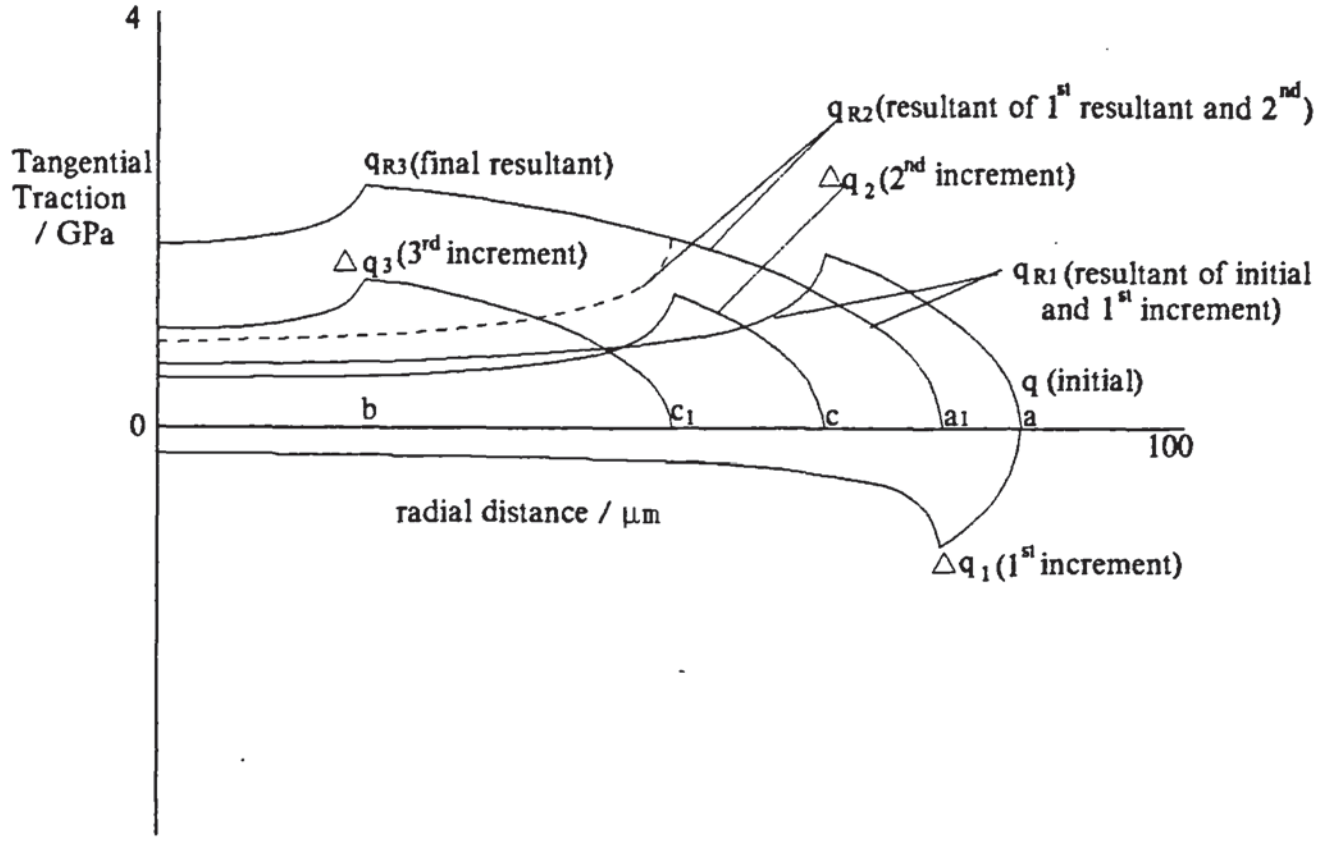

Fig. 3.17. Tangential traction distribution.

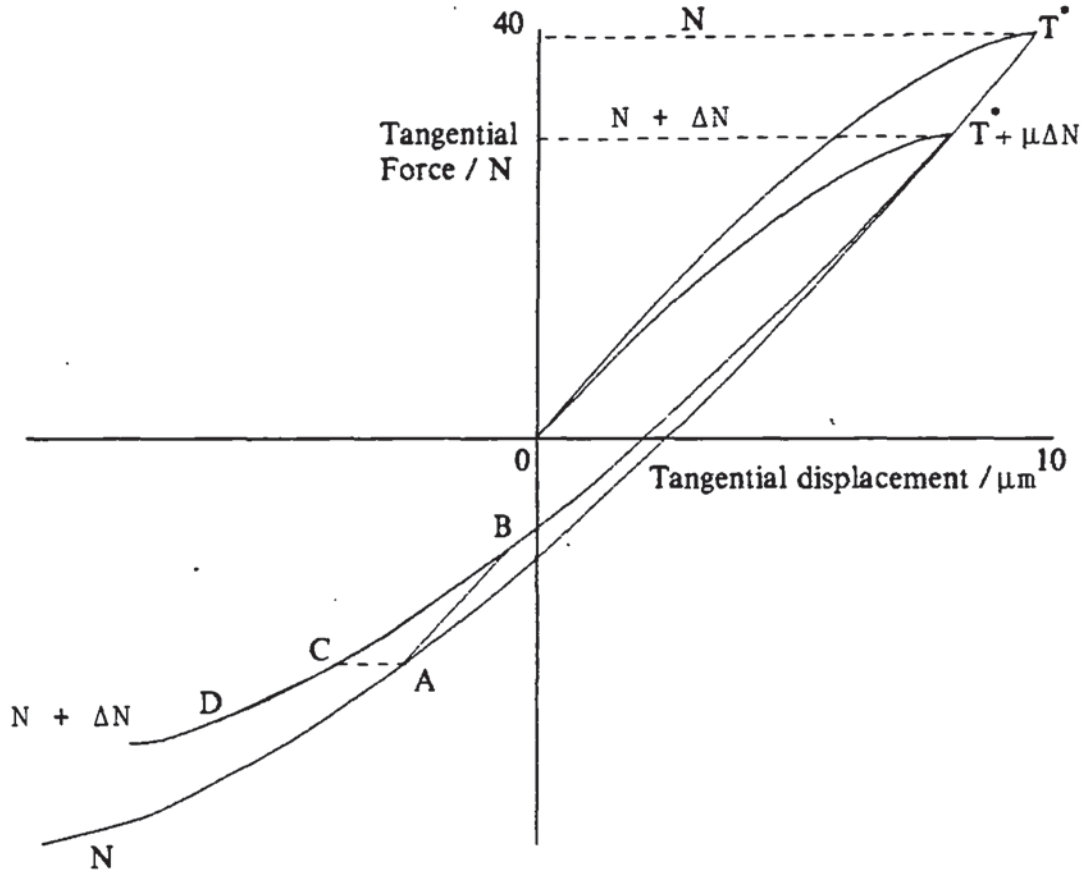

Fig. 3.18 Tangential force–displacement behaviour.

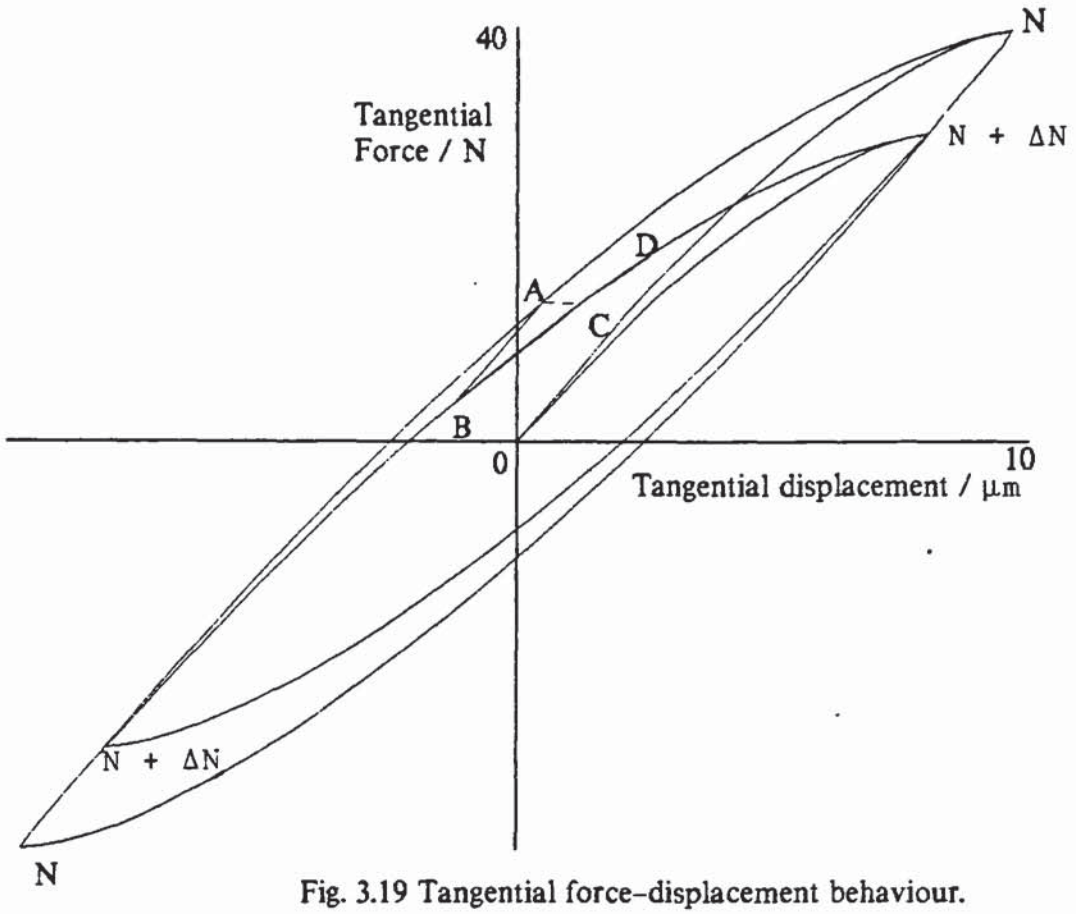

Fig. 3.19 Tangential force–displacement behaviour.

Comparing (3.68), (3.75) and (3.81) it is clear that we may use the following equation

$$\Delta T = 8G^* a\theta\Delta\delta \pm \mu\Delta N(1-\theta) \qquad (3.94)$$

which when ΔN is zero reduces to the general solution for constant normal force, equation (3.52).

The parameter θ is defined by the appropriate loading case and the sign of the second term is negative for unloading only, thus

$$\theta = [(1-(T+\mu\Delta N))/\mu N]^{1/3} \qquad \text{loading} \qquad (3.95)$$

$$\theta = [(1-(T^*-T+2\mu\Delta N))/2\mu N]^{1/3} \qquad \text{unloading} \qquad (3.96)$$

$$\theta = [(1-(T-T^{**}+2\mu\Delta N))/2\mu N]^{1/3} \qquad \text{reloading} \qquad (3.97)$$

$$\theta = 1.0 \qquad \text{for } \Delta N>0 \text{ and } \Delta T<\mu\Delta N \qquad (3.98)$$

In addition, as described in section 3.3, load reversals, when $T^{**}<T<T^*$, are treated as non-linear elastic using (3.94) and (3.97).

4. Development of the computer program BALL.

4.1 Historical development of BALL.

Cundall (1971) described a simulation program for modelling large-scale movements of blocky rock systems. There were two basic versions of the program, one which modelled a section through an assembly of cylinders and the other which modelled a section through an assembly of rectangular blocks. In this early version of the disc program all discs had identical dimensions and properties. Simulation of movements of the discs was advanced using a small fixed time step which was limited to a fraction of the critical time step for numerical stability which in turn was based upon the mass and equivalent stiffness of the discs. The calculation cycle was divided into two parts. In the first part the forces at every contact were updated from the displacement and rotation increments of the two particles in contact. A linear spring and dashpot force-displacement law was then employed for the shear and normal directions with sliding being governed by a Coulomb type friction law. The contact force was then resolved into the global coordinate components and summed for each particle. The second part of the cycle took the force and moment sums for each particle and with Newton's second law of motion derived the accelerations which upon integration gave velocities and displacement increments and on further integration gave the new positions and rotations. Two types of boundary control were possible, strain control (velocity fixed), and stress control (fixed applied force).

Cundall (1976) incorporated a number of modifications to reduce processing time. The introduction of a distance around each particle (TOL) was developed such that if

adjacent particles have a distance less than TOL between them, although the particles themselves are not already in contact, the system is considered as a potential contact. If a potential contact is determined a space in the contact list is made available, and if particles are separating the contact is only deleted when the distance between them is greater than TOL. Thus only when a particle moves more than TOL/2 is a search for new contacts necessary. The particle coordinates are stored in two parts, the sum of which gives the coordinate. The second part is always less then TOL/2$\sqrt{2}$ and is the cumulated movement of the particle. When the cumulated movement exceeds TOL/2$\sqrt{2}$, in terms of the cumulated x or y coordinate, a search for potential contacts is undertaken and the cumulated value zeroed after being added to the first part of the coordinate.

The processing time was further reduced in the search for contacts by dividing the system into a grid of boxes and mapping particles into the boxes and remapping them as they moved. Thus potential contacts could be detected without scanning the whole assembly. The boxes are squares of size DEL and the maximum radius of a particle is restricted to <(DEL/2)+TOL. Thus the maximum number of boxes in which a particle can have entries is four. In the search for a potential contact it is only necessary to interrogate particles with common box entries. A linked list technique was also introduced whereby data was stored at random and linked by pointers. Terms could be added or deleted from the lists extremely rapidly and memory was automatically allocated to new contacts and recovered from old. Cundall (1978) reported the addition of new commands to facilitate creation

and deletion of particles and the introduction of kinematically controlled walls. The facility was added to input different particle and wall properties and dimensions. Also, if required during a test, it was possible to change properties and dimensions of particles, the boundary control and the time step of the program. Zeroing of velocities, introduction of gravity and a print facility to obtain the full details of particles, walls, types, contacts and boundary particles etc, were also introduced.

Two of the most useful additions were analysis routines to calculate the average stress and strain tensors for a specified circular region within the assembly. A further boundary control facility was also added which permitted either strain or stress to be applied over a specified number of cycles, thus allowing a gradual application of stress or strain. Further alterations which had been recently added were detailed in an appendix to Cundall (1978). These included a porosity calculation within a given radius, pictorial representation of force polygons, particle rotations and fabric plots. Cundall and Strack (1983) partitioned the stress tensor into its fabric, normal variation and shear components which were calculated and printed out.

A boundary servo control was also introduced which, upon choosing an appropriate gain parameter, enabled a desired stress path to be followed by constantly adjusting the appropriate components of the boundary strain tensor.

4.2 Program BALL at Aston.

Cundall's program BALL was used and enhanced by Barnes (1985). Further plotting options and analysis routines were

introduced. Barnes (1985) introduced two analysis routines both of which require a given internal radius. One subroutine is primarily concerned with calculating the stress tensor for a sub-assembly and partitioning it into its normal, shear, normal variation and fabric components. This differs from the subroutine developed by Cundall and Strack in that it partitions the tensor into its four components where each partition is calculated independently, including the total, which thus gives a check on the calculations. Also the stress tensor is calculated as an average of the individual stress tensors for each particle in the sub-assembly. The other analysis subroutine is concerned with statistical information and calculates the second and fourth order structural anisotropy tensors for the assembly, refer to section 4.6 for more detail. The total number of contacts and sliding contacts within the sub-assembly are also given. Barnes (1985) also introduced a subroutine to determine the total and dissipated energy in the assembly. The plotting routines that were available as single plots or to superimpose on others at this time were; discs (with the option of the disc number in the centre), grid of boxes, boundary, contact forces and particle velocities. Also the following plots were available in comparison to a reference state; rotation vectors, cumulative sliding displacement, rotation directions and a representation of the equivalent space lattice of the system illustrating the current state and the changes that have occurred since the reference state.

4.3 Particle-particle interaction laws.

To enable the simulation to successfully predict the internal mechanisms and forces of a real system of particles it

was necessary to introduce realistic contact laws. Hence the linear force-displacement laws were replaced by the non-linear normal force-displacement law of Hertz (1882) and the non-linear history dependant tangential force-displacement laws of Mindlin and Deresiewicz (1953).

The subroutine FORD which incorporates the force-displacement laws for normal and tangential particle interactions has therefore been extensively rewritten. Originally the following linear force-displacement laws were employed

$$\Delta N = \Delta n(STIFN) \tag{4.1}$$

$$\Delta T = \Delta s(STIFS) \tag{4.2}$$

where STIFN and STIFS were directly input into the program and represented the normal and shear stiffnesses, ΔN and ΔT were the normal and tangential force increments, and Δn and Δs were the normal and shear displacement increments.

Normal and tangential contact damping was of the form

$$N_t = N + \Delta N(\beta/2.FRAC) \tag{4.3}$$

$$T_t = T + \Delta T(\beta/2.FRAC) \tag{4.4}$$

where FRAC was the desired fraction of the critical time step and β was the required damping factor. The theory governing the new force-displacement laws has been covered in Chapter 3. The following section will explain the logic of the coding and highlight any other alterations necessary for the implementation of the new force-displacement laws.

4.3.1 The logic of subroutine FORD.

If the contact is between a particle and a wall, a previously set flag is read as true and sends the program to

a section which calculates the normal and shear displacements based on the particle and wall movements. The equivalent radius and mass for the contact is set to that of the particle. The program then enters the coding at the E* calculation.

For particle-particle contacts the particles are tested as to whether they are still in contact or merely a potential contact. This is achieved by determining whether the distance between the two particle centres is less than the sum of their radii. For two particles in contact the direction cosines of the contact normal vector are calculated. The program then calculates the following relative properties for the contact,

equivalent radius:

$$R^* = (R_1 . R_2)/(R_1 + R_2) \qquad (4.5)$$

equivalent mass:

$$M^* = (M_1 . M_2)/(M_1 + M_2) \qquad (4.6)$$

equivalent Young's modulus:

$$E^* = (E_1 . E_2)/(E_1(1-\nu_2^2) + E_2(1-\nu_1^2)) \qquad (4.7)$$

where ν is the Poisson's ratio. (Note this is the re-entry position for particle/wall contact).

Finally, the relative shear modulus is defined by

$$G^* = (G_1^* . G_2^*)/(G_1^* + G_2^*) \qquad (4.8)$$

where

$$G_1^* = E_1/(2(1+\nu_1).(2-\nu_1)) \qquad (4.9)$$

$$G_2^* = E_2/(2(1+\nu_2).(2-\nu_2)) \qquad (4.10)$$

The Hertzian contact law is then used to determine the normal force increment.

For no previous normal force (thus no radius of contact)

$$\Delta N = 4[E^*(R^* . \Delta n^3)^{1/2}]/3 \qquad (4.11)$$

For a previous normal force

$$\Delta N = 2.\Delta n.E^*.a \qquad (4.12)$$

where a is the radius of the contact area.

The normal force is updated and a test performed to check whether the particles are still in contact after the last normal force increment or decrement. If so, then the normal force damping contribution is added. If not, then the contact data is set to zero and the subroutine ends. The contact is not necessarily deleted as, although there is no normal force between the particles concerned, the gap between the particles may be very small and the particles likely to come into contact again. Only if the gap between the particles exceeds a specified value (TOL) is the contact deleted. The new normal force damping calculations are,

Total Normal force = Updated Normal force + Dx'

Where $D = \beta.D_{crit}$ and $D_{crit} = 2(M^*.2.E^*.a)^{1/2}$, and $2.E^*.a$ is the normal stiffness.

Thus,

$$N_t = N + (2.\beta(M^*.2.E^*.a)^{1/2}).(\Delta n/\Delta t) \qquad (4.13)$$

where Δt is the time step.

The radius of contact is then calculated as

$$a = (3.N.R^*/4.E^*)^{1/3} \qquad (4.14)$$

The minimum coefficient of friction of the two particles in contact is taken as the controlling friction coefficient. If the contact is frictionless then the program moves to the updating of the tangential force where the tangential force contributions are necessarily zero, otherwise the direction of loading is determined. It is necessary to move to the updating of the tangential force if the tangential force

contribution is zero because various other parameters may need updating. This is due to changes in the normal force, the implications of which will be described later in this section.

A test is performed to determine whether there is a tangential displacement. For no tangential displacement the subroutine also moves to the updating of the tangential force with the tangential force increment set to zero.

It is important to determine the current direction of tangential loading. This is stored under CDF which is -1 for a negative loading direction and +1 for a positive. The loading direction is based upon the program's sign convention of tensile normal stresses and clockwise shear stresses acting on a bounded area being positive.

For virgin loading CDF=+1 for T>0. For unloading or reloading the sign of CDF corresponds to the sign of T* which is the tangential force from which unloading commenced. The program then calculates the tangential force increment using the value of θ determined by the function THETA which also sets an unloading flag UFL, (see section 4.3.2).

The increment in tangential force is expressed by

$$\Delta T = CDF(\theta(8.G^*.a.\Delta s.CDF - \mu.\Delta N.UFL) + \mu.\Delta N.UFL) \qquad (4.15)$$

which compares with (3.94) after re-arrangement.

Once the tangential force increment is calculated the new value of DD is determined.

To explain the use of the parameter DD it is necessary to refer to the end of section 3.4.1, which describes the case of normal force increasing when $\Delta T<\mu\Delta N$. This illustrates that for this case $\Delta s<\Delta s_1$ and the system would fail to meet point B in fig 3.9, but would be on the line between A and

B where the equation for the line AB is defined by (3.70). This equation for the incremental stiffness is used until (3.71) is true. To apply this to the coding of the program it is necessary to calculate the critical value of Δs (Δs_c) which is necessary for the system to reach the appropriate point on a normal force constant curve. From equation (3.65)

$$\Delta s_c = \mu.\Delta N/(8.G^*.a) \qquad (4.16)$$

The difference between this value and the actual Δs is termed DD and needs to be found and stored. For successive cycles of $\Delta T<\mu\Delta N$ the value DD will cumulate as the system grows farther from its point on an appropriate normal force constant curve. Then if for the following cycles $\Delta T>\mu\Delta N$ the system will approach its appropriate point on a normal force constant curve and thus DD would need to be reduced. Only when DD is found to be <=0, and thus the condition prescribed by equation (3.71) met, will equation (3.68) be used. Hence, for each cycle if $\Delta T<\mu\Delta N$ DD is given by (4.17). If $\Delta T>\mu\Delta N$ and DD has a cumulated value (4.17) is also used to decrease the value of DD as $\Delta s_c < \Delta s$.

$$DD = DD + (\Delta s_c - \Delta s.CDF) \qquad (4.17)$$

For the case of N decreasing ΔT is always greater than $\mu\Delta N$ and thus DD is defined by (4.18).

$$DD = DD + \Delta s_c \qquad (4.18)$$

The system is then tested for load reversals. If the tangential displacement increment multiplied by the loading direction is negative, and T* and T** do not have values, then unloading must have been initiated and T* is set to the old value of T. Also, if the tangential displacement

increment multiplied by the loading direction is positive and T* has a value but T** does not, then reloading must have been initiated and T** is set to the old value of T. The tangential force is then updated by adding the calculated increment. The contact is examined for sliding. If T > μN the contact is sliding, T is reset to μN, and the sliding displacement is accumulated. Optional tangential contact damping is available of the form,

$$T_t = T + 2.\beta(M^*.|\Delta T/\Delta s|).\Delta s/\Delta t \qquad (4.19)$$

However, due to the dissipative nature of the tangential contact laws it is anticipated that further tangential energy dissipation will not be necessary.

It is important to determine whether the system is at the point of initiation of unloading or reloading when N is varying. This is because if the system has not just started unloading or reloading and T* and T** have values (i.e. T* will have a value only if the system has previously unloaded, T** will have a value only if the system has previously reloaded) they need to be updated by μΔN. Refer to fig 3.13 which illustrates that for increasing values of N, T* is increased and thus T** decreased by μΔN.

$$T^* = T^* + CDF.\mu.\Delta N \qquad (4.20)$$

$$T^{**} = T^{**} - CDF.\mu\Delta N \qquad (4.21)$$

Finally, it is necessary to check for the re-establishment of virgin loading or unloading, as with virgin loading the previous history of the contact has been erased and thus T* and T** are re-set to zero. Similarly with unloading any reloading history of the contact has been erased and thus T** is set to zero.

Having updated the normal and tangential contact information, the contributions of the contact forces to the out of balance force and moment of the two particles are then calculated in terms of the global coordinate system and added to the force sums for each particle. The subroutine then ends.

4.3.2 The logic of function THETA.

In function THETA the critical tangential displacement (Δs_c) is initially determined. This is the tangential displacement necessary for the system to reach its equivalent point on a normal force constant curve, equation (4.16).

The function is then divided into four sections; setting a flag THE1 for normal force increasing, decreasing and constant, and then reading the flag to use the appropriate equation for θ. For all unloading cases an unloading flag UFL is set to -1. Otherwise it is set to +1.

For the cases of normal force decreasing or constant, a series of conditional statements are used to determine whether the system is loading, unloading, reloading or re-unloading. Reloading is identified if the tangential displacement multiplied by the loading direction is increasing but the absolute value of the tangential force is less than the absolute value of T*. For this case THE1 is set to 3. If the reloading criterion is false and the tangential displacement multiplied by the loading direction is increasing, then THE1 is set to 1 indicating virgin loading. Re-unloading is identified if the preceding criteria have not been met, the tangential force multiplied by the loading direction is greater than T** multiplied by the loading direction, and T** is not zero. For this case THE1 is set to 3. Unloading

is determined if all the other criteria were not met and then THE1 is set to 2.

However, for the reasons given in section 3.4, each case for normal force increasing has two possibilities in terms of tangential displacement: $\Delta s <> \mu.\Delta s_c + DD$ where DD is the cumulative amount the system has fallen short of its equivalent point on a normal force constant curve. All cases are dealt with in the same way as the previous paragraph, unless $\Delta s < \mu.\Delta s_c + DD$ in which case THE1 is set to 4.

Finally, for the various values of THE1, θ is calculated:

THE1=1 $\quad \theta = (1-(T.CDF + \mu\Delta N)/(\mu.N))^{1/3}$ (4.22)

THE1=2 $\quad \theta = (1-(T^*.CDF - T.CDF + 2.\mu.\Delta N)/(2.\mu.N))^{1/3}$ (4.23)

THE1=3 $\quad \theta = (1-(T.CDF - T^{**}.CDF + 2.\mu.\Delta N)/(2.\mu.N))^{1/3}$ (4.24)

THE1=4 $\quad \theta = 1$ (4.25)

corresponding to (3.95)-(3.98) respectively.

The value of θ is then passed to the subroutine FORD.

4.4 System initialisation.

The program was originally limited to a maximum of 5 particle types and a maximum particle size of 10 units. The number of possible particle sizes has now been increased to 50. This enables less discontinuous particle size distributions to be adopted.

When a new simulation test is initiated certain parameters are used for checking particle movements and for graphics which are fixed by the program. These parameters are now automatically scaled to the maximum particle size. This was necessary for the introduction of S.I. units and enables

particle sizes to be changed by orders of magnitude. Particles were previously considered as cylinders or discs of unit length. The particles are now considered to be spheres whose centroids all lie in the same plane. For the purpose of calculating sample volumes and for calculating or applying the overall stress tensor, the dimension normal to the plane is taken to be the average sphere diameter. Young's modulus and Poisson's ratio for each particle type are now input as properties instead of the normal and shear stiffness previously specified.

The particle CREATE command has been altered so that an initial velocity (x velocity, y velocity and angular velocity) can be specified. This is particularly useful for impact experiments.

One of the problems in preparing an assembly had always been that the initial assembly as generated had a high porosity. This meant that when a boundary was generated and strain controlled, and when forces had propagated through the assembly from the boundary, a considerable reduction in the overall assembly diameter occurred. The particles that were fixed on the boundary when the assembly was generated are now fixed on a much smaller boundary perimeter. This reduction in the assembly perimeter had the effect of compressing the boundary particles such that large overlaps, and thus forces, were unrealistically generated between them. With an assembly in this state it was then very difficult to switch between a strain controlled and a stress controlled boundary. Unless the applied stress was considerably higher than the boundary stresses, the high unrepresentative boundary forces would cause the particles to be ejected. To reduce these effects by generating a denser

initial assembly, the program was re-coded so that if all the required particles of a certain size could not be fitted into the assembly, instead of stopping as was previously the case, the program would now move on to the next smaller particle size and attempt to generate all those. This new method of generation produces a much more dense assembly than the previous method, and thus not only reduces the effect of the locked in high boundary forces, but also requires much less compression to achieve a desired isotropic stress level.

4.5 Experimental procedures.

4.5.1 Time step considerations

Previously the time step for the program was based upon the critical time step for numerical stability, equal to the minimum of

$$\Delta t_c = 2(M/STIFN)^{1/2} \quad (4.26)$$

or

$$\Delta t_c = 2(M/STIFS)^{1/2} \quad (4.27)$$

where STIFN and STIFS were input directly into the program. The time step was then set to the specified fraction of the critical time step.

$$\Delta t = \Delta t_c . FRAC \quad (4.28)$$

However, to simulate the behaviour of real material the time step used in the calculation cycle should be based on real force transmission speeds. In three dimensional elastic bodies energy is transferred through the body by dilational (pressure) waves, which are material element volume fluctuations without shear deformation, distortional (shear) waves,

in which the material elements distort without a change in volume, and surface waves. The speed of the dilational wave is given as

$$c_1 = (2(1-\nu)G/(1-2.\nu)\rho)^{1/2} \qquad (4.29)$$

and the distortional wave speed is

$$c_2 = (G/\rho)^{1/2} \qquad (4.30)$$

In addition Rayleigh waves are propagated along the surface of a body with a velocity

$$c_3 = \alpha.c_2 = \alpha(G/\rho)^{1/2} \qquad (4.31)$$

Where α is the root of the equation

$$(2-\alpha^2)^4 = 16(1-\alpha^2)(1-\alpha^2 c_2^2/c_1^2) \qquad (4.32)$$

The speed of the surface waves is just slightly less than that of the distortion waves. The pressure waves account for 7%, the shear waves for 26% and the surface waves for 67% of the radiated energy. Also pressure and shear waves decay with distance to a much greater degree than surface waves. For these reasons the time step is now based on the Rayleigh wave speed for the average particle diameter of the assembly. Thus, the program having calculated the average radius and shear modulus for the assembly and having used a linear approximation to (4.30), the equation for the Rayleigh wave speed for the assembly is rearranged to give the time step required,

$$\Delta t = ((\pi^2.\bar{R}^2.\rho/\bar{G})^{1/2})/\alpha \qquad (4.33)$$

where

$$\alpha = (0.1631\nu + 0.876605) \qquad (4.34)$$

A multiple of this time step can be used by issuing the command FRAC x where x is the multiple of the Rayleigh wave

speed required. By using a smaller time step a greater degree of accuracy is obtained but more cycles are necessary to achieve desired movements. A larger time step can be used for disperse systems to enable large movements in small numbers of cycles. Cundall (1971) shows that for a simple mass-spring system the time step should not exceed the critical time step, $2\sqrt{(M/K)}$. However, for a non-linear system K varies and thus the critical time step constantly alters for each particle in the assembly. Hence, to determine the critical time step for a particle the stiffness K, which is the effective stiffness of the particle, needs to be calculated in terms of the current force and velocity increment.

$$K = \Delta\Sigma F/\Delta x \tag{4.35}$$

where

$$\Delta x = [(Vx^2 + Vy^2)^{1/2}]\Delta t \tag{4.36}$$

where Vx and Vy are the current velocity components.

Thus the critical time step is

$$\Delta t_c = 2(M.\Delta x/\Delta\Sigma F)^{1/2} \tag{4.37}$$

for each particle.

In subroutine MOTION, which is the subroutine that computes new velocities and displacements for each particle given the forces and moments acting upon it, an array SUMFOLD (no. of particles) is used to determine $\Delta\Sigma F$, as

$$\Delta\Sigma F = \Sigma F_{new} - \Sigma F_{old} \tag{4.38}$$

where

$$(\Sigma F_{new})^2 = (\Sigma F_x)^2 + (\Sigma F_y)^2 \tag{4.39}$$

The ratio of the actual time step to the critical time step is

$$FRACC = \Delta t/\Delta t_c \tag{4.40}$$

If FRACC is greater than 0.3 it has been found that the time step for dense assemblies with many contacts can be too large, and unrealistic particle overlaps can occur in one time step which can thus create large out of balance forces, and as a result numerical instability. The program warns the user if the maximum value of FRACC for any cycle is over 0.3. Thus the command FRAC x can be issued to reduce the time step, where x<1.

4.5.2 Strain control

Cundall (1988) reports the development of a three dimensional version of BALL, which is reviewed towards the end of section 2.3. In this simulation periodic boundaries are employed and thus the definition of a boundary from which a stress or strain tensor is applied is not applicable. Cundall (1988) treats the centres of the particles as points in a continuum and defines a continuum strain rate tensor which prescribes the particle movements, further movements resulting from the interactions between particles are treated as perturbations on the continuum behaviour. Cundall (1988) achieves this by the use of the following equations

$$\Delta u_i = \Delta u_i + \dot{e}_{ij} x_j \Delta t \qquad (4.41)$$

where

Δu_i is the displacement increment

$\dot{e}_{ij}$ is the continuum strain rate tensor

x_j is the particle coordinate

Δt is the time step.

The relative approach velocity is increased by

$$\dot{u}_i^{(rel)} = u_i^{(real)} + \dot{e}_{ij}\, z_j^{(diff)} \qquad (4.42)$$

where

$\dot{u}_i^{(rel)}$ is the relative approach velocity of the two spheres

$\dot{u}_i^{(real)}$ is the relative 'real' velocities obtained from particle interactions

$\dot{e}_{ij}$ is the continuum strain rate tensor

$z_j^{(diff)}$ is the vector joining particle centres.

For the two dimensional particle simulation reported in this thesis a similar tensor to Cundall's has been employed. In conjunction with the continuum strain rate tensor it was necessary to define a boundary strain rate tensor of equal magnitude. If this was not used the assembly would break up due to perturbations caused by interactions within the assembly. Two alterations were necessary to the program to incorporate the tensor, the first being in subroutine FORD which is the subroutine which calculates the normal and tangential force increments and the second in subroutine MOTION which calculates the new velocities and displacements for each particle. The following two equations were added to both these subroutines

$$\dot{x} = \dot{x} + \dot{c}_{11}.x + \dot{c}_{12}.y \qquad (4.43)$$

$$\dot{y} = \dot{y} + \dot{c}_{22}.y + \dot{c}_{21}.x \qquad (4.44)$$

where $\dot{x}$ and $\dot{y}$ are the relative velocities of the particles in FORD and are the velocity components of the particle under consideration in MOTION. In FORD x and y are the distances between the particle centres but in MOTION they are taken to be the particle coordinates.

The continuum strain rate tensor is defined by

$\dot{c}_{ij}$ (i,j=1,2).

4.6 Analysis routines.

A large amount of additional information is now available to the user. The radius of the contact area, the average normal and shear contact stresses, and the contact radius divided by the radius of the smaller of the two contacting particles. These are all now printed out when the PRINT CONTACTS command is given. The normal and shear stress information is particularly useful in gauging the maximum, minimum, average and distribution of contact stresses for a given applied stress, Thornton and Randall (1988). If the material yield stress is known the areas of the assembly for which the Hertzian contact laws are not strictly relevant can be identified. The contact radius divided by the minimum particle radius for that contact can be used to determine whether the contact has exceeded 7% overlap. This is another indication of whether the assembly has been loaded to such an extent that the Hertzian laws employed are no longer valid. One further new parameter that is calculated is the contribution of each particle type to the total number of contacts. With this facility it is possible to determine whether for particular loading cases it is the smallest particles that are generally redundant or whether the redundancy is evenly spread across the particle sizes. It is anticipated that this may become of greater use for assemblies with extreme gradings, with the largest particle many times larger than the smallest.

A new subroutine has been introduced called AVERAGES which, when eight particle or contact parameters are passed to it, returns the maximum, minimum and average values of the parameters which are then printed out. For particles the

eight parameters are, the contact angle, x velocity, y velocity, angular velocity, x force, y force and moment. For contacts, the parameters are the normal force, shear force, contact angle, radius of contact, normal contact stress, tangential contact stress, and the radius of contact divided by the minimum particle radius for that particular contact. Also two further commands have been introduced, PRINT AVERAGES and PRINT ALL. Issuing the PRINT AVERAGES command will ensure that every time thereafter when a PRINT BALLS or PRINT CONTACTS command is given only the max, min and average information will be printed out. The PRINT ALL command cancels a previously issued PRINT AVERAGES command.

In the calculations and statistics subroutine CAST, the structural anisotropy tensor for the assembly is calculated. To describe the structure of the assembly satisfactorily the closeness of packing and directional distribution of particles must be accounted for. This was achieved by Oda et al (1982) who described the microstructure of an assembly of particles by a second order 'fabric' tensor, which can be expressed as:

$$F_{ij} = F_{KK} . \Phi_{ij} \quad (i,j=1,2) \tag{4.45}$$

The program BALL calculates and prints out the two components of the fabric tensor where

$$F_{kk} = (2M\bar{R}/V) \tag{4.46}$$

and 2M is the total number of contacts occupying a volume V, $\bar{R}$ is the average disc radius. The structural anisotropy is defined by the tensor

$$\Phi_{ij} = \langle n_i n_j \rangle \quad (i,j=1,2) \tag{4.47}$$

where n_i define the contact normal vectors.

In the program BALL Φ_{ij} is calculated in the following way

$$\Phi_{ij} = (1/M)\sum_{1}^{M} n_i n_j \qquad (i,j=1,2) \qquad (4.48)$$

where

$$n_1 = \Delta x/D \qquad (4.49)$$

$$n_2 = \Delta y/D \qquad (4.50)$$

$$D = (\Delta x^2 + \Delta y^2)^{1/2} \qquad (4.51)$$

where Δx and Δy are horizontal and vertical distances between the centres of two contacting particles. In addition the structural anisotropy tensor is printed out weighted to the normal and tangential force.

The major and minor principal values and angles are also calculated for the second order structural anisotropy tensors.

With reference to fig 4.1,

$$\Phi_1 = (\Phi_{11} + \Phi_{22})/2 + [((\Phi_{12}+\Phi_{21})^2 + (\Phi_{11}-\Phi_{22})^2)^{1/2}]/2 \qquad (4.52)$$

$$\Phi_2 = (\Phi_{11} + \Phi_{22})/2 - [((\Phi_{12}+\Phi_{21})^2 + (\Phi_{11}-\Phi_{22})^2)^{1/2}]/2 \qquad (4.53)$$

$$\theta = 0.5.\arctan[(\Phi_{12}+\Phi_{21})/(\Phi_{11}-\Phi_{22})] \qquad (4.54)$$

All input and output parameters are now given in SI units.

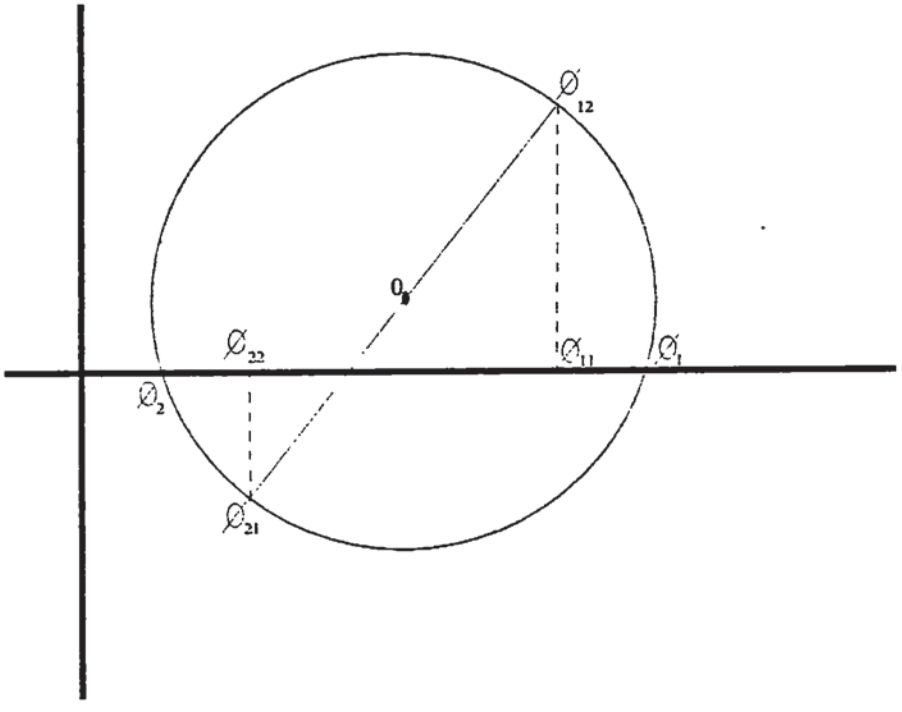

Fig. 4.1 Mohr's circle illustrating the second order structural anisotropy tensor.

4.7 Graphics facilities.

Minor alterations have been made to the plotting routines due to the different sizes of particles that are now used. Scaling, velocity vectors and particle number position offsets are now based on the maximum particle size. With the command PLOT X, where X is a real number, a picture can be enlarged or reduced. Also it is now possible to select different colours for each plotting option. The SELECT command now expects a number between 1 and 10 after each plotting option number. The numbers represent the following colours,

1- black

2- red

3- orange

4- yellow

5- green

6- cyan

7- blue

8- violet

9- brown

10- white.

5. Program validation tests.

5.1 Introduction.

It is essential to test the validity of the modifications to the program undertaken in this research project. Many of the alterations were relatively simple to check. For example the introduction of a time step based on the Rayleigh wave speed merely required hand calculations to determine the correct time step for a number of cases, including some extremes. These cases were then used in the program and the same time steps were obtained. However, before using the program to simulate a large assembly of particles, simple tests had to be performed to verify the new inter-particle force laws described in chapter 3, and coded as described in chapter 4. Two simple series of tests were performed to validate the program under quasi-static and dynamic conditions.

5.2 Quasi-static oblique loading tests.

Two identical spheres were created with the following properties: R=10 mm, μ=0.3, ρ=7.8 Mg/m^3, E=210 GPa, ν=0.3. Kinematically controlled frictionless walls, with the same elastic properties as the particles, were used to achieve the desired relative displacement of the spheres. The initial configuration of the system is shown in fig 5.1. For the first test two equal and opposing vertical velocities were applied to both sets of walls to compress the two spheres and thus establish a normal force between them. Fig 5.2 illustrates the normal force-displacement curve obtained with theoretical predictions using (3.13) superimposed giving excellent agreement.

The vertical wall velocities were then zeroed and horizontal velocities specified to develop a relative tangential dis-

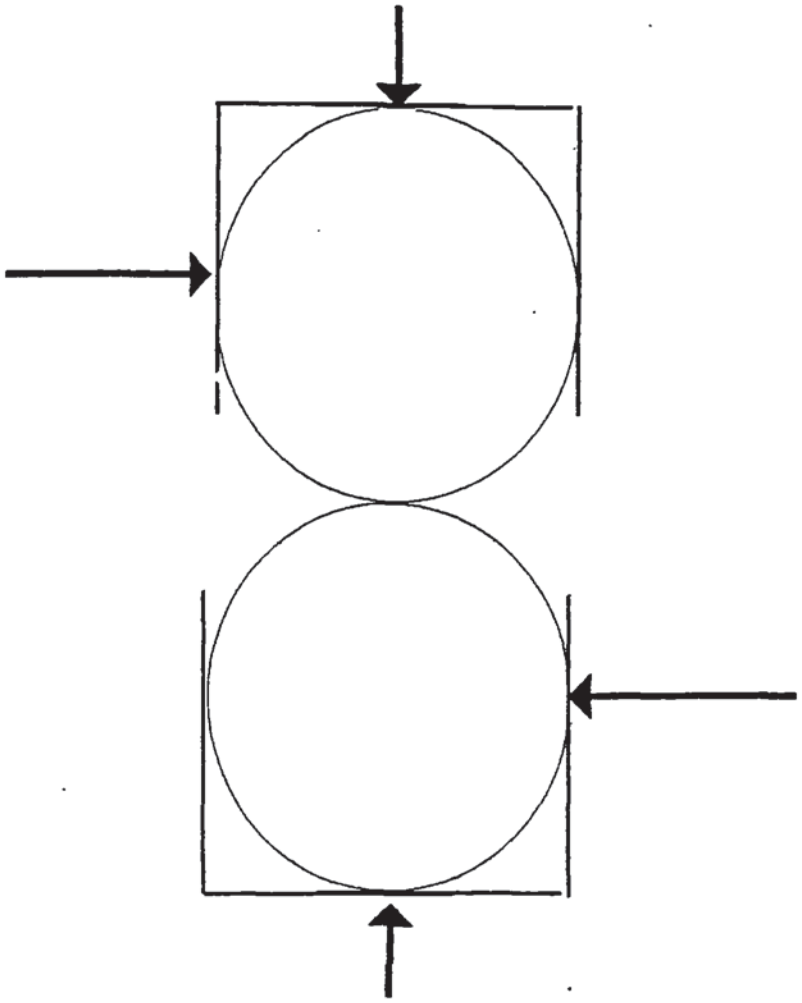

Fig 5.1 Quasi-static contact validation tests.

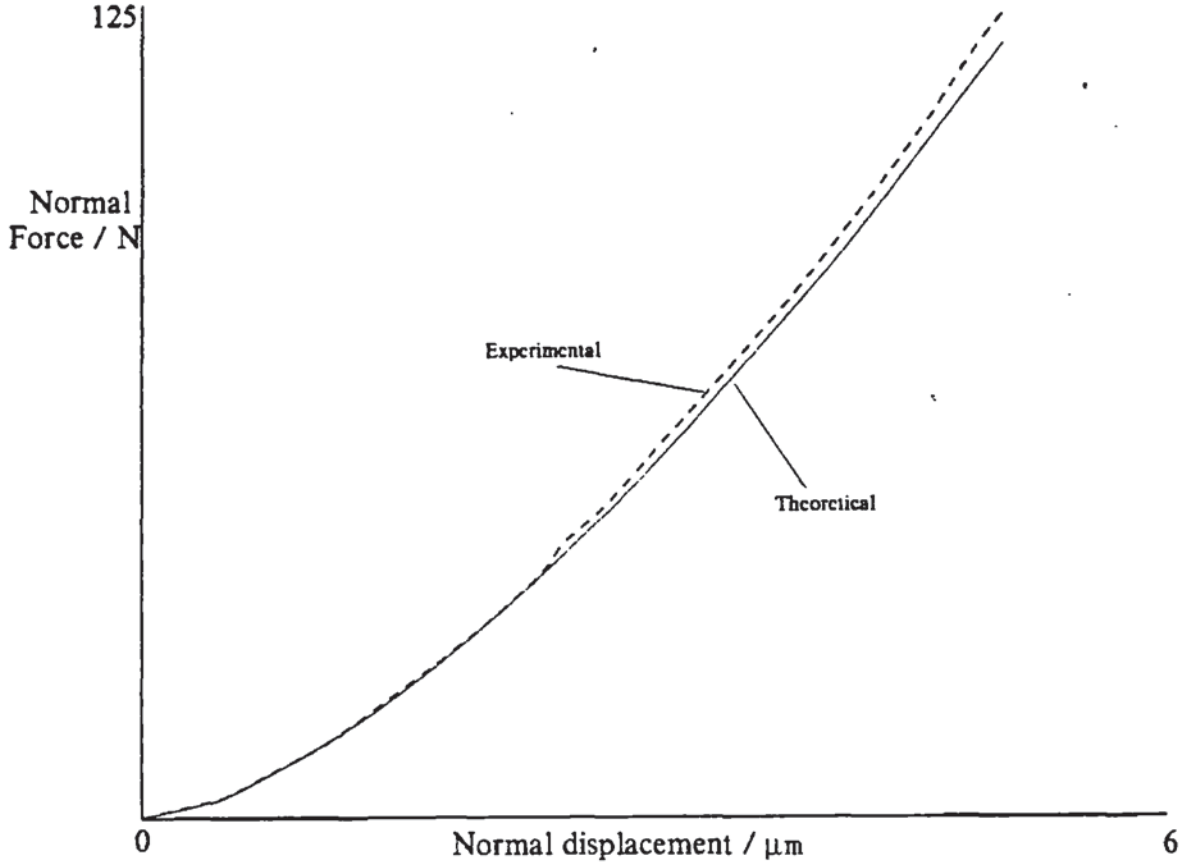

Fig. 5.2 Hertzian force-displacement relationship.

placement between the spheres to produce tangential loading, unloading and reloading behaviour. During this stage the normal contact force remained essentially constant. The results from some of these simulations are illustrated in fig 5.3 with the theoretical values calculated using the equations of Mindlin and Deresiewicz (1953) for a constant normal force of 88N. Excellent agreement between theory and simulation can be seen.

With the same initial configuration as in fig 5.1 a number of other tests were undertaken for more complex loading histories. Tangential loading, unloading, reloading and re-unloading were all performed for both increasing and decreasing normal force. These simulations produced complex load-displacement curves which could not be easily verified from the theory in chapter 3 due to the tracing of the loading history. However the correct operation of the program was checked by printing out the dominant loading direction, and the loading case which was currently being used along with the decisions this was based upon.

5.3 Dynamic impact.

For an explicit validation of the new force-displacement laws, involving complex loading histories and a varying normal force, a series of single particle impact tests were performed. This also checked the program's ability to handle dynamic problems. The simulations were restricted to elastic impact. Permanent contact deformation and energy dissipation due to particle deformation were ignored.

5.3.1 Normal impact.

The classical elastic impact theory was initiated by Hertz (1882) and follows from his static theory of elastic

contact, section 3.1. Elastic wave motion was ignored in his analysis and the total mass of each body was assumed to be moving at any instant with the velocity of its centre of mass. Hertz (1882) considered a co-linear impact for two elastic spheres with masses m_1 and m_2, and velocities v_{N1} and v_{N2} acting normal to their contact. During impact their centres approach by a displacement α, their relative velocity being

$$v_{N2} - v_{N1} = d\alpha/dt. \qquad (5.1)$$

The normal force between them is

$$N = m_1 dv_{N1}/dt = -m_2 dv_{N2}/dt \qquad (5.2)$$

thus

$$-N/m^* = d(v_{N2}-v_{N1})/dt = d^2\alpha/dt^2 \qquad (5.3)$$

where

$$1/m^* = 1/m_1 + 1/m_2 \qquad (5.4)$$

The relationship between N and α is assumed to be the same as for a static elastic contact

$$N = (4/3)R^{*1/2}E^*\alpha^{3/2} = K\alpha^{3/2} \qquad (5.5)$$

and hence

$$m^* d^2\alpha/dt^2 = -K\alpha^{3/2} \qquad (5.6)$$

Integrating (5.6) with respect to α gives

$$1/2[V_N^2-(d\alpha/dt)^2] = 2/5(K/m^*)\alpha^{5/2} \qquad (5.7)$$

where

$$V_N = (v_{N2} - v_{N1})_{t=0} \qquad (5.8)$$

is the approach velocity.

At the point of maximum compression α^*, $d\alpha/dt = 0$ and thus

$$\alpha^* = (5m^*V_N^2/4K)^{2/5} = (15m^*V_N^2/16R^{*1/2}E^*)^{2/5} \qquad (5.9)$$

Substituting α^* in (5.5) gives the maximum normal force further integration of (5.7) gives the compression-time curve

$$t = \alpha^*/V_N \int d(\alpha/\alpha^*)/[1-(\alpha/\alpha^*)^{5/2}]^{1/2} \qquad (5.10)$$

Deresiewicz (1968) evaluated this integral and produced the force-time curve in fig 5.4. After the time for maximum compression (t^*) the spheres once again rebound. The total impact time T_c is therefore

$$T_c = 2t^* = 2\alpha^*/V_N \int_0^1 d(\alpha/\alpha^*)/[1-(\alpha/\alpha^*)^{5/2}]^{1/2} \qquad (5.11)$$

$$T_c = 2.94\alpha^*/V_N = 2.87(m^{*2}/R^*E^{*2}V_N)^{1/5} \qquad (5.12)$$

This analysis is only applicable for elastic contacts with a circular contact area.

5.3.2 Oblique impact.

Maw et al (1976) presented two solutions for the oblique impact of an elastic sphere on a half space. Hertzian impact theory was used for normal force/velocity components, and the area of contact was assumed to be divided into areas of stick or slip. It was also assumed that the coefficient of friction was constant in an area of slip and that friction was the only source of energy dissipation. To enable a solution for the boundary values for the tangential tractions and displacements the contact area was arbitrarily split into a set of concentric annuli.

Previous elementary approaches neglected the elastic displacements of the solids, which would distinguish two conditions, that of sliding and rolling. The elastic displacements associated with impact are generally small compared with the dimensions of the solids. However, they can produce possibilities which cannot be accommodated within the elementary theories. This is because work done in producing tangential displacements is stored as elastic strain energy

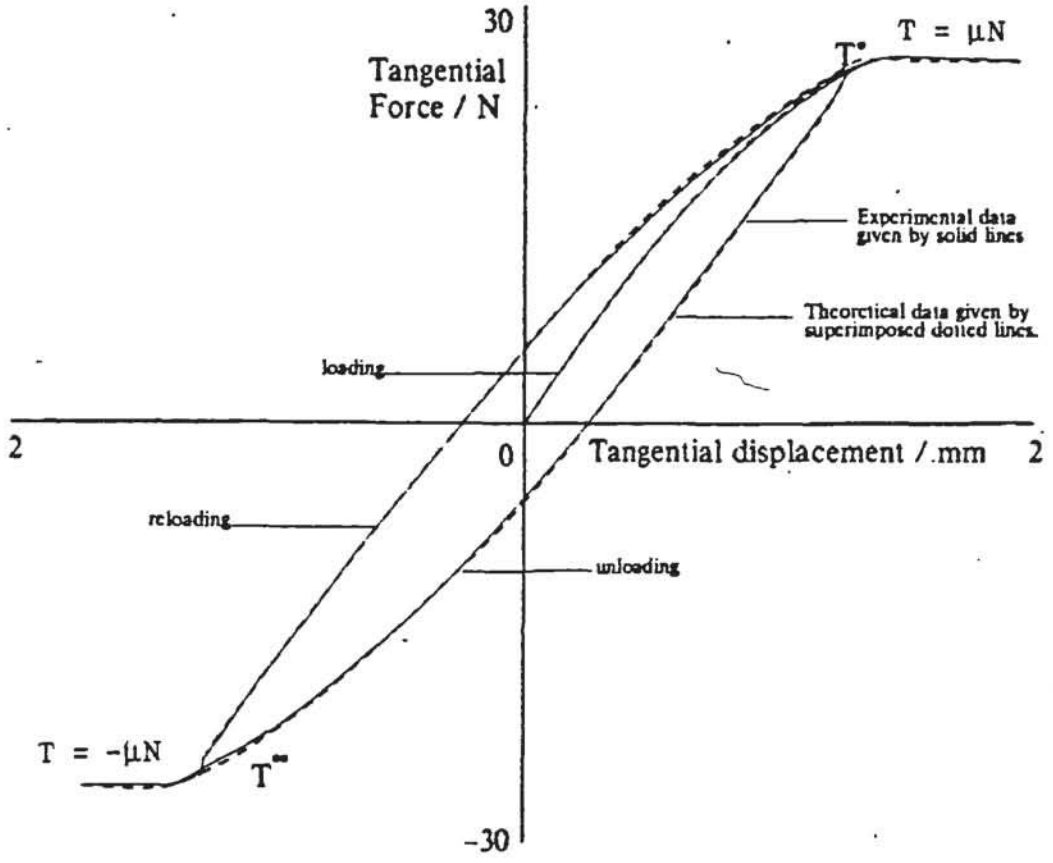

Fig. 5.3 Tangential force / displacement behaviour.

Fig 5.4 Variation of the normal approach of the sphere as a function of the time of contact, Deresiewicz (1968).

which is recoverable. Also, as described by Mindlin (1949), the tangential displacement is not constant across the contact area but is split into areas of slip and stick. During impact the normal force varies, and thus the loading situations of varying normal force investigated by Mindlin and Deresiewicz (1953) are applicable.

Maw et al (1976) describe their exact solution, which used the laws of Mindlin and Deresiewicz (1953), and which advanced through the period of impact in small discrete time increments. This exact solution from initial known values of normal and tangential velocity found the displacements in a time step and these thus defined the boundary conditions of the instantaneous contact. The changes in velocity components during the time increment were then found from the contact forces having used momentum considerations.

Maw et al (1976) stated that the previous history of the system only influences the instantaneous behaviour of the contact in so far as it determines the locked in tangential displacements in the areas of stick. Hence for their simple rigid body theory they represent the distribution of tangential displacements by a series of functions, and thus the system was no longer dependent upon the storage of the loading history. Maw et al (1976) compared the results of using their exact and simple rigid body methods and reported close agreement in cases to which both can be applied.

Maw et al (1976) defined the traction distribution such that the total traction in the direction of the tangential motion at a radius r is

$$q(r) = \sum_{i=j}^{n} q_i (1-n^2 r^2 / a^2 i^2)^{1/2} \qquad (5.13)$$

where j is the smallest integer greater than nr/a, n is the number of concentric annuli across the contact area and a is the maximum radius of the contact area. This series is based upon the work of Mindlin (1949) and gives an analytical expression for tangential displacements and includes the exact solution for the condition of sliding.

An equation for determining the n coefficients q_i can be obtained for each of the n annuli. In areas of slip the tangential traction $q(r) = \pm\mu p(r)$ where $p(r)$ is the local normal contact pressure. To facilitate this a provisional division into stick and slip regions is assumed, the appropriate equations were solved and the solution tested to check the initial assumption. In regions of stick the tangential traction is below the limit at which slip occurs, whereas within slip regions the relative incremental displacement must be in the correct sense for the assumed frictional traction. If these tests fail in any region the assumption is changed and a new solution is obtained. Convergence was reported as rapid.

Maw et al (1976) showed that the resultant trajectory of the sphere after impact was dependant on two non-dimensional parameters. The first of these, related to the radius of gyration of the sphere, is,

$$\chi = (1-\nu)(1+1/K^2)/(2-\nu) \qquad (5.14)$$

where $K = (I/MR^2)^{1/2}$. Note for a solid sphere $K^2 = 2/5$.

The other is the local non-dimensional tangential velocity: the 'local' tangential velocity being the velocity of the contact.

$$\psi = (2(1-\nu)/\mu(2-\nu))(V_T/V_N) \qquad (5.15)$$

where V_N is the normal velocity, V_T is the corresponding

tangential velocity and

$V_T/V_N = \tan\theta$ (5.16)

where θ is the angle of incidence.

Fig 5.5 illustrates the variation in tangential and normal forces during a cycle at various values of ψ_1 produced by Maw et al (1976). The value of χ was fixed at 1.4412 corresponding to a homogeneous solid sphere with ν=0.3. The forces were plotted such that T and N coincide when $T=\mu N$. For small angles of incidence the tangential force can be seen to reverse shortly after the point of maximum penetration. At the mid-point of the cycle the local tangential velocity is opposite in direction to that at incidence. The tangential oscillation is reduced in the cases when $T = -\mu N$ and the direction of sliding is opposite to the relative tangential velocity at incidence. During the final stage of impact the surface of the half space moves in the same direction as the local incident tangential velocity of the sphere, and at a greater speed than the sphere itself, which has been retarded. For larger angles of impact the initial period of sliding delays the start of the tangential force oscillation but the same general type of behaviour occurs.

Maw et al (1981) made the following observations. When $\psi_1 <= 1$ the surfaces initially stick and new contact annuli are formed, free of tangential traction, until just before maximum compression when slip is initiated. Once the mid point of the impact is passed the contact area reduces and the tangential elastic recovery of the system causes an annulus of slip to spread inwards, until a point is reached when the system can no longer support the tangential traction, the stick annulus being fully penetrated, and rigid body sliding occurs. At this point the value μN has

been reached by the tangential force.

For $1 < \psi_1 < (4\chi-1)$ the impact initially occurs in sliding, hence the tangential traction is everywhere $\mu\sigma$. Friction decreases the relative velocity of the objects to zero at which instant the contact annulus is stuck throughout. The subsequent behaviour of the contact then during rebound is the same as for $\psi_1 < 1$. As ψ_1 is increased the sliding/stick transition occurs later in the cycle. Finally if $\psi_1 >= (4\chi-1)$ sliding occurs throughout the entire impact and hence the tangential displacement does not reverse.

If $\psi_1 = 1.2$ is taken as a typical case where the contact is initiated in sliding which is opposed by the friction force. At about a quarter of the cycle time the $\mu\sigma$ criterion is no longer satisfied and the surfaces are thus sticking, but the system continues to deform in the original slip direction. The oscillation then follows a normal pattern until near the end of the cycle, when the elastic recovery of the deformable surfaces is in the same direction as the movement of the particle, but at a greater speed. Thus sliding in the opposite sense to the original is initiated and persists for the remainder of the impact.

The non-dimensional local angle of reflection plotted against the corresponding angle of incidence produced by Maw et al (1976), fig 5.6, illustrates the regimes discussed above. For values of $\psi_1 < 1$ ψ_2 is positive, slip occurring during the impact. For values of $1 < \psi_1 < 4\chi-1$ ψ_2 is negative and the impact occurs initially in the sliding condition, and when $\psi > 4\chi-1$ sliding persists throughout the impact.

Maw et al (1981) report a series of experiments undertaken to validate the analyses presented by Maw et al (1976).

Fig 5.5 Nondimensional tangential force plotted against nondimensional time for different angles of incidence for a sphere, Maw (1976).

Fig 5.6 Nondimensional local angle of reflection against that of incidence for a sphere, Maw (1976).

Measurements were made of the angles of incidence and reflection of a disk impacting a fixed block. A disk shaped puck was propelled over an air bed towards a clamped block of an identical material. A heavy launching device, incorporating a pendulum, provided a means of producing repeatable initial conditions. Stroboscopic photography was used to measure impact and rebound angles and velocities. Three pucks were used, two of steel with a matching impact block and a third of rubber again with a matching impact block. Values of ν were obtained from the material specifications and μ from simple impact experiments. With the steel pucks the experimental values of ψ_2 for the partial-stick impacts were lower than predicted. This means that the elastic energy stored in the material was either less than expected or not recovered to the anticipated extent. The theoretical value for the coefficient of restitution of 1.0 was reduced to 0.93 giving an indication of the extent to which the material behaved according to the assumptions used in the theory. For the rubber puck the coefficient of restitution was 0.86 which was not considered low enough to transgress the assumptions seriously.

The paper presented by Maw et al (1976) was restricted to a study of the analytical behaviour of the oblique impact of spheres, whereas the paper produced by Maw et al (1981) was concerned with the analytical and experimental behaviour of oblique impacts of discs. Fig 5.6 illustrates ψ_1 against ψ_2 for spheres and fig 5.7 illustrates the same relationship for discs. Comparing these two graphs, the main difference arises for small angles of incidence where positive values of ψ_2 are obtained for $\psi_1 < 1$ in the case of spheres whereas this feature is not apparent for discs.

Rigid body theory outlined in the beginning of this section agrees with the more exact theory for $\psi_1 >= 4\chi$ but predicts $\psi_2 = 0$ for $\psi_1 < 4\chi$. The exact theory predicts elastic recovery of the surface which leads to negative local angles of reflection. Also, sliding occurs throughout the cycle at lower values of ψ_1 than those predicted by the rigid body theory since the tangential elastic recovery of the surfaces can maintain relative motion even when the sphere has been brought to rest.

5.4 Oblique impact tests.

Maw et al (1976) predicted that for oblique impacts the angles of reflection and rebound velocities would not be those obtained from the simple 'rigid body' theory. Thus in imitating the experiments of Maw et al (1976), having incorporated the laws of Mindlin and Deresiewicz (1953) and Hertz (1882) which were used by Maw in his 'exact' theory, and by defining a particle with the same non-dimensional parameters and contact friction as Maw, we should anticipate similar results from our simulations.

Maw et al (1976) published values of $\nu=0.28$, $\mu=0.12$ and $\chi=1.4412$ for his simulations using a spherical particle, thus a sphere was defined with $\nu=0.28$, $\rho=7800$ kg/m^3, E=210 GPa and R=1mm giving a value for χ of 1.465. A series of oblique impact tests were then simulated, refer to fig 5.8. The impact velocity of v=0.4m/s was chosen such that, for the time step used, between thirty and forty points were obtained for the contact duration. The particle was generated with the desired velocity close to the wall in a gravity free system so that few cycles were necessary to initiate

Fig 5.7 Nondimensional local angle of reflection against that of incidence for a disc, Maw (1981).

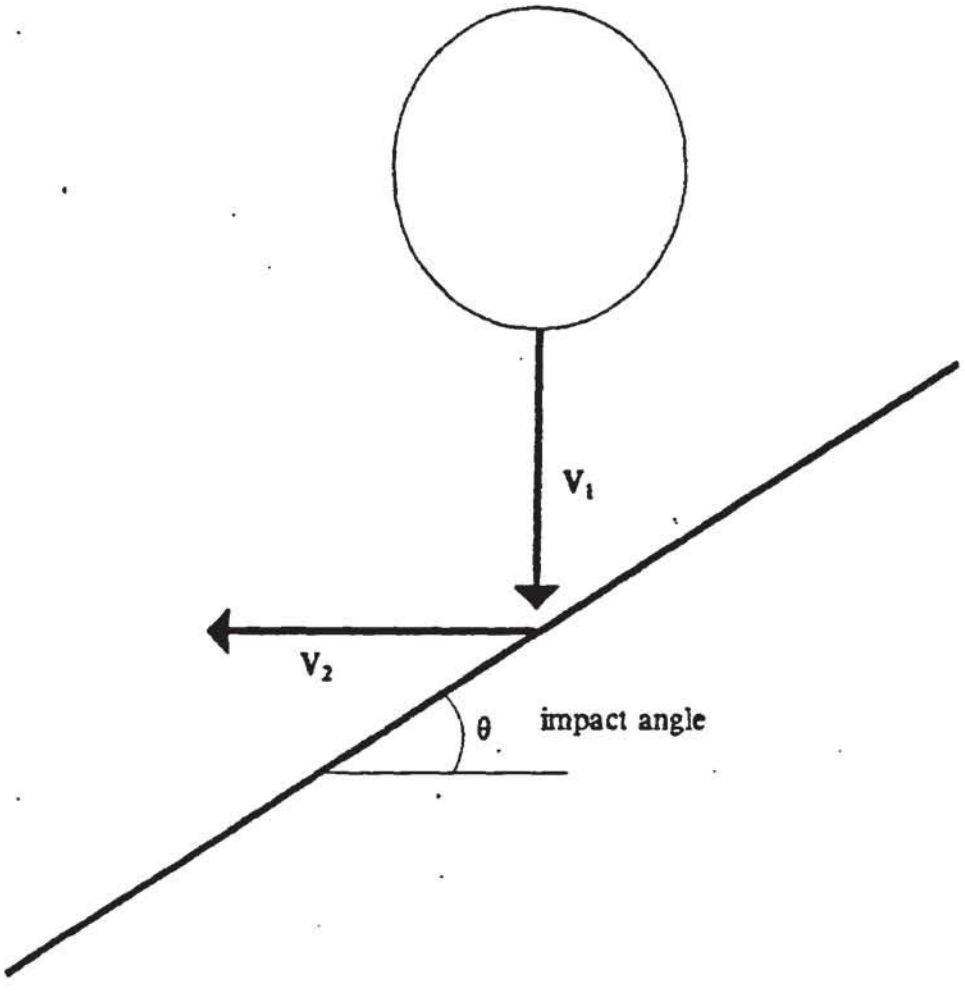

Fig. 5.8 Oblique impact.

the impact. Fig 5.9 illustrates $T/\mu N_{MAX}$ against t/T_c for various angles of impact which can be directly compared with the results published by Maw et al (1976) in fig 5.5; excellent agreement can be noted. All the trends reported by Maw are present. For small angles of incidence ($\psi_1 < 1$) the contact is initiated in stick. After maximum compression, annuli of slip begin to spread inwards over the contact area as a result of the re-distribution of traction over the shrinking contact area. Once the normal force decreases to a certain value, this value being dependent on the angle of impact, slip occurs over the whole of the remaining contact area and the contact undergoes rigid body sliding. The smaller the angle of impact the later this occurs until the asymptote of normal impact is reached.

In the second regime ($1 < \psi_1 < 4\chi - 1$) the contact is initiated in sliding which is eventually countered by the frictional force. Tangential force reversal then occurs. The stored elastic energy of the system is now released in the same direction as the particle movement but at a greater speed, and once again sliding is initiated until the end of contact. The larger the angle of incidence the later the tangential force oscillation occurs, until finally the third regime occurs ($4\chi - 1 < \psi_1$) where the entire duration of contact is dominated by rigid body sliding.

In fig 5.10 the plot of local angle of reflection against that of incidence is illustrated. Again, directly comparing this with the results of Maw et al (1976) shown in fig 5.6 illustrates excellent agreement. For $\psi_1 < 1$ ($\theta < 9°$), sliding only occurs at the end of impact and positive values of ψ_2 are obtained indicating no overall reversal in the tangential velocity. The results produced by Maw et al (1976) in

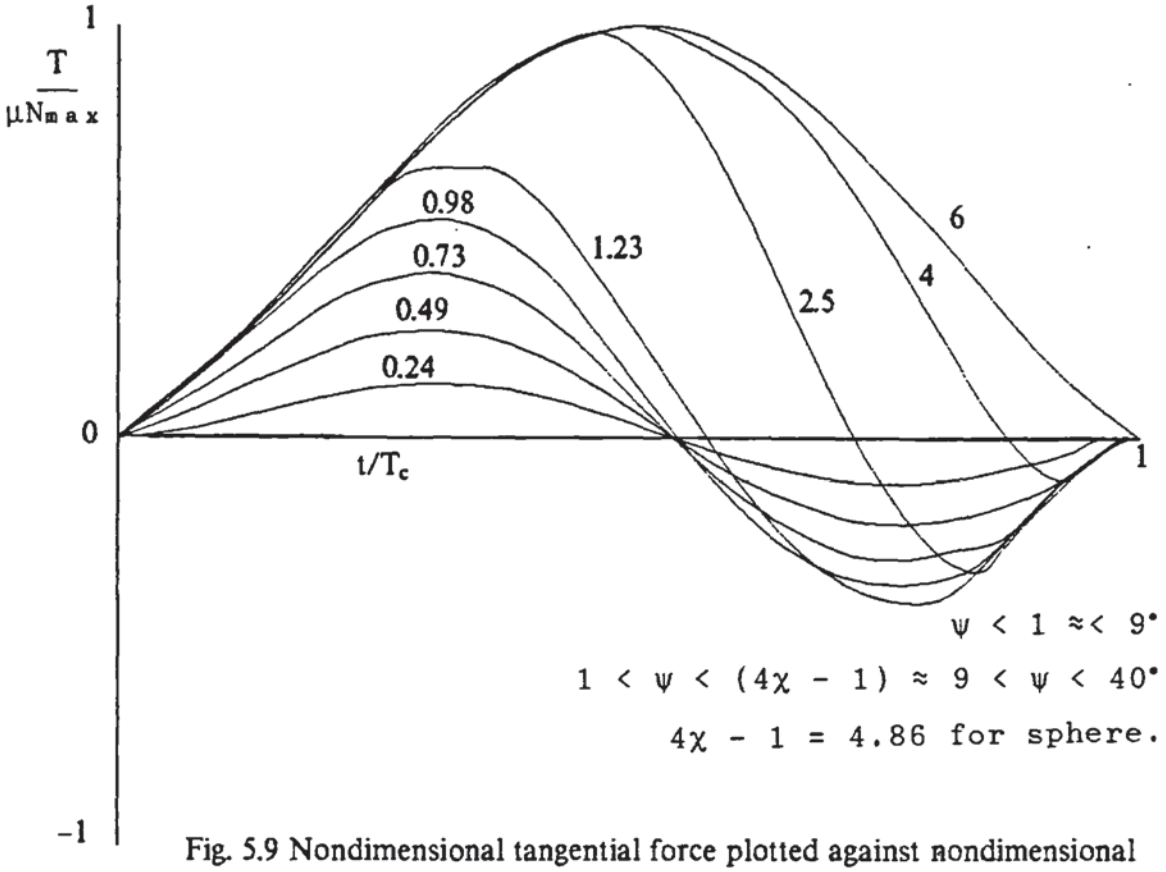

Fig. 5.9 Nondimensional tangential force plotted against nondimensional time for different angles of incidence.

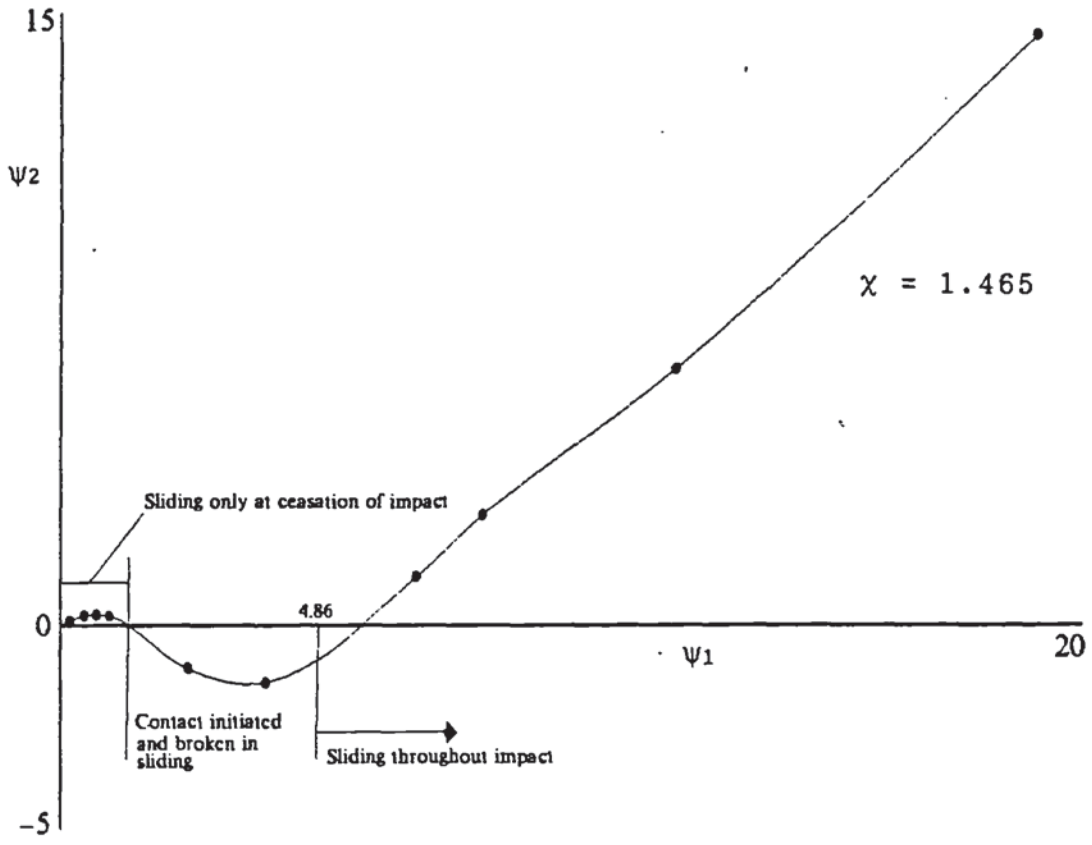

Fig. 5.10 Nondimensional local angle of reflection against that of incidence.

fig 5.6 using spheres illustrate this, however those produced by Maw et al (1981) in fig 5.7 using discs do not illustrate this phenomenon. This indicates that although the program BALL can only simulate two dimensional assemblies of particles the particles are treated as spheres and not discs and do successfully illustrate the behaviour of impacting spheres. For $1<\psi_1<4\chi-1$, which are the impacts initiated and terminated in rigid body sliding, the local tangential velocity component is reversed and the point on the periphery of the sphere, which on impact is at the centre of the contact, after impact has a negative angle of reflection thus 'bouncing back' toward the direction of impact. However, the angle of reflection of the sphere measured from the centre of the particle is positive and so the negative angle of reflection of the contact area is produced by spin. For impacts occurring within the third regime where $\psi_1>4\chi-1$ ($\theta>=40°$), because no rolling occurs and thus no tangential force reversal since sliding occurs throughout the impact, positive values of ψ_2 are once again obtained illustrating no overall local tangential velocity reversal.

As an alternative to fig 5.9 the variation of tangential and normal forces during an impact are shown in figs 5.11 to 5.13, for typical examples of the three regimes of behaviour indicated in fig 5.10. Figure 5.11 illustrates the variation of tangential with normal force for an angle of incidence $\theta=4°$. The figure clearly shows that rigid body sliding only occurs at the end of the impact. The tangential force can be seen to decrease well before the normal force reaches a maximum and soon after the normal force starts to decrease the tangential force direction reverses. For an impact angle of 20° fig 5.12 shows that rigid body sliding occurs from

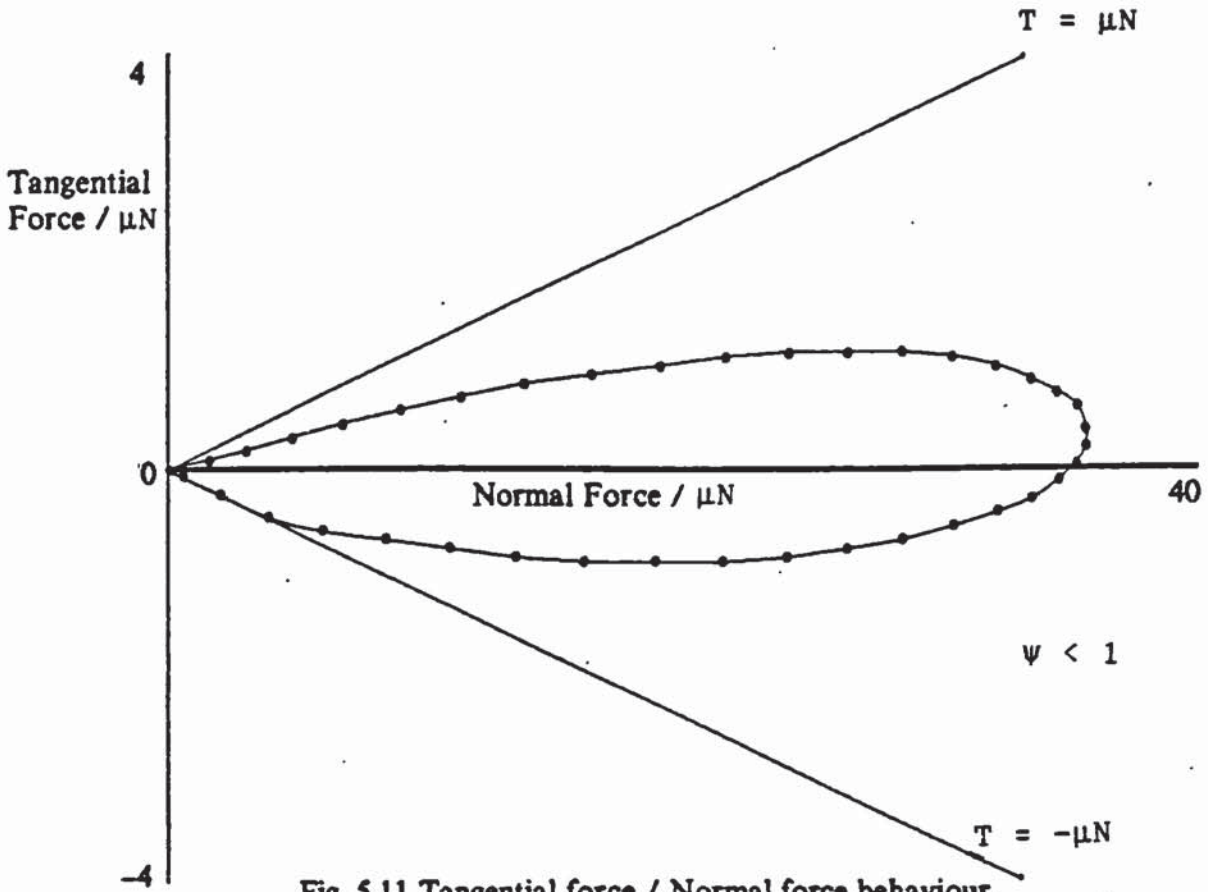

Fig. 5.11 Tangential force / Normal force behaviour.
Impact angle of 4°.

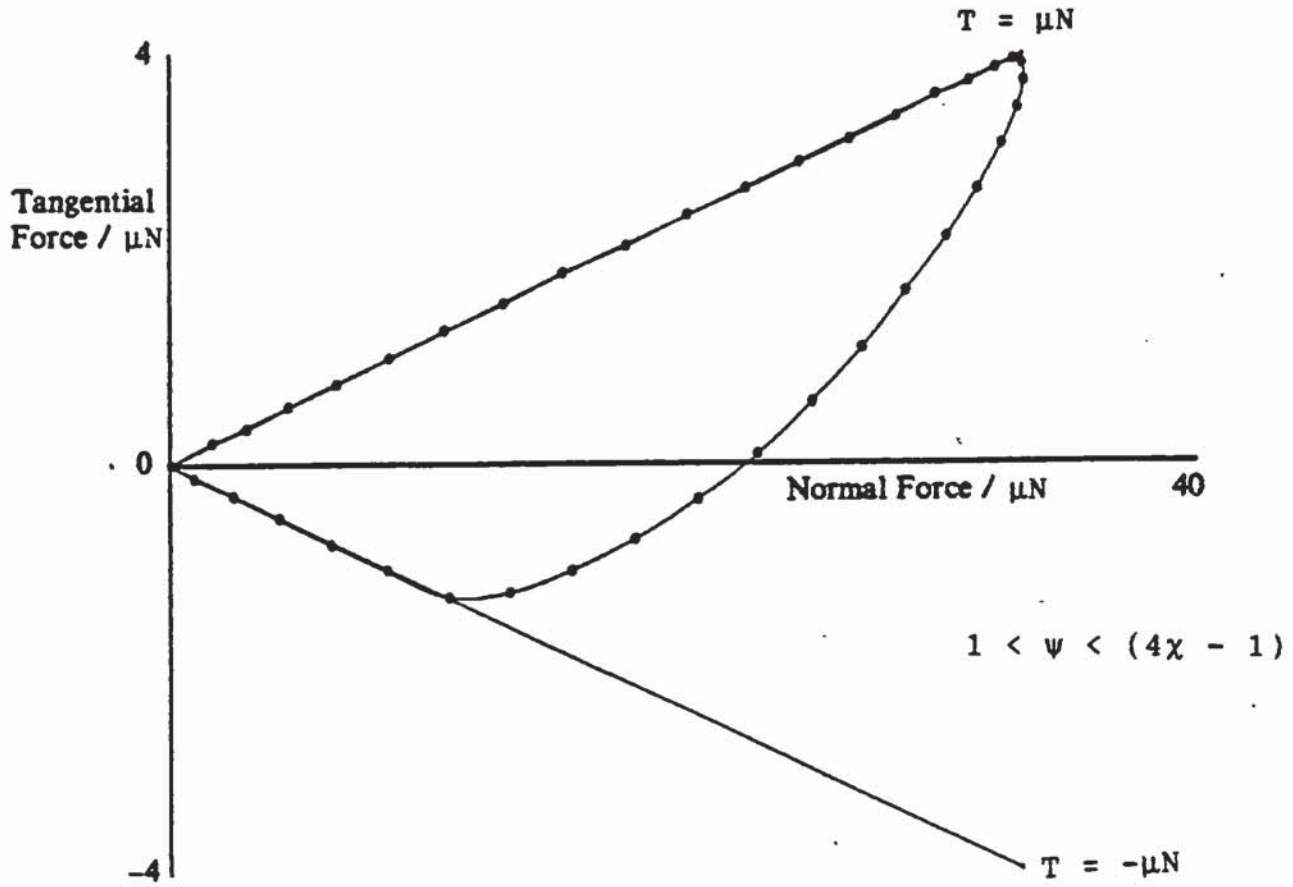

Fig. 5.12 Tangential force/ Normal force behaviour.
Impact angle of 20°.

the start of the impact until the normal force has almost reached its maximum value. At this point the tangential force is a maximum. Rigid body sliding then stops as the tangential force reduces. The normal force then reduces and the tangential force continues to reduce and then reverses in direction until it reaches a maximum value. At this point rigid body sliding is resumed and continues until the end of the impact. The third regime of behaviour is illustrated in fig 5.13 for $\theta=40°$. The figure clearly shows that rigid body sliding occurs throughout the duration of the impact.

For a given impact velocity the effect of increasing the angle of impact θ on the normal force-displacement behaviour is to reduce the maximum normal force and displacement due to the reduction in the normal velocity component. The tangential force-displacement behaviour of the contact is, however, much more complex, as shown in figs 5.14-5.16.

The tangential force-displacement behaviour for $\theta=4°$ is illustrated in fig 5.14. It can be seen that, although no rigid body sliding occurred as the normal force was increasing, the work done during tangential loading was not fully recovered when the tangential force reduced to zero. This is due to slip dissipating energy as it spreads radially inward over the contact area. Similarly, after the tangential force direction has reversed slip results in irrecoverable deformation. However, close to cessation of the contact, due to re-distribution of the remaining traction, sliding finally occurs causing further irrecoverable deformation and a small net negative tangential displacement results. It is interesting to note that fig 5.14 indicates that, if no rigid body sliding occurred, the overall displacement would have been fully recovered even though energy had been dissipated by

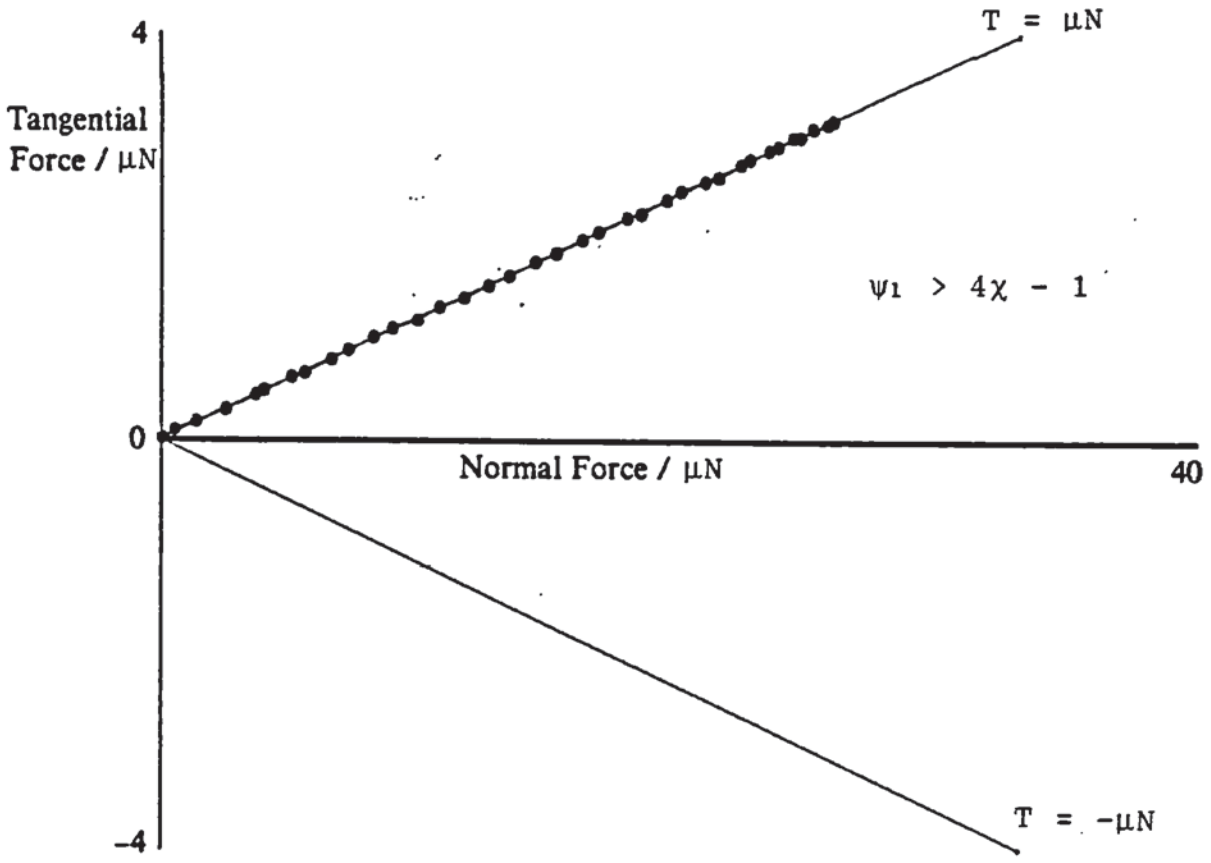

Fig. 5.13 Tangential force / Normal force behaviour.
Impact angle of 40°.

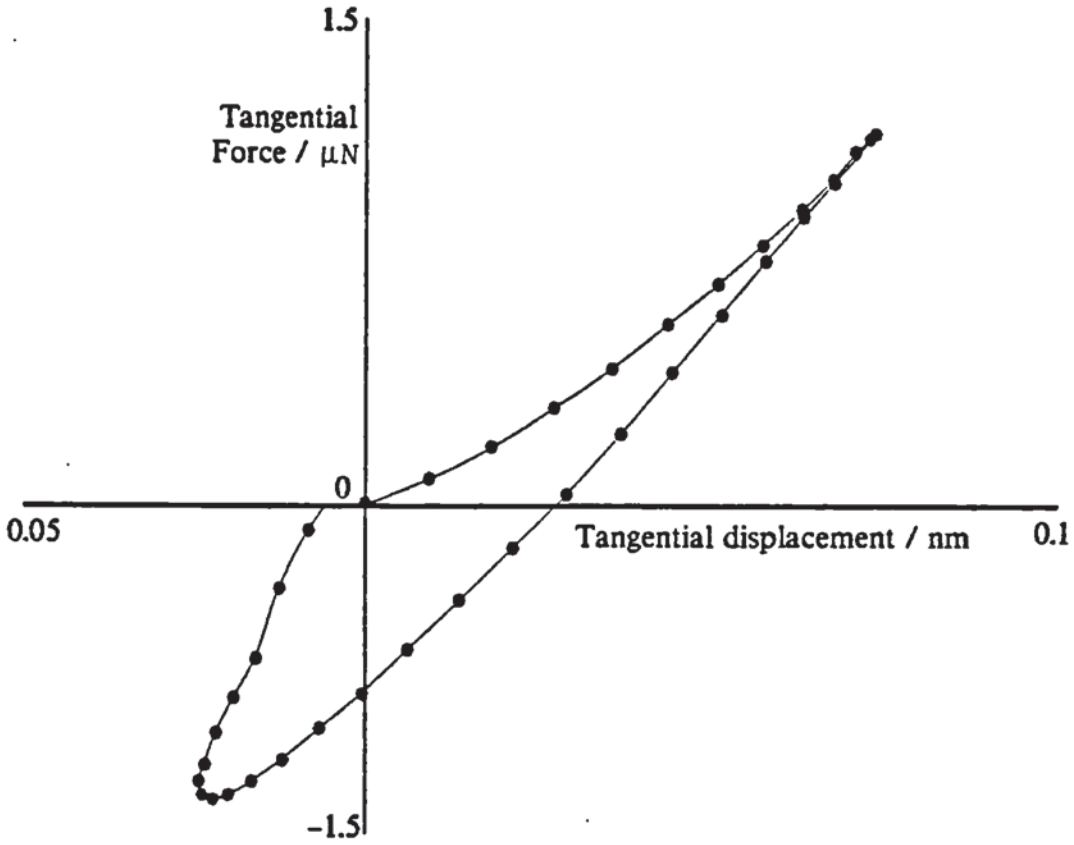

Fig. 5.14 Tangential force / displacement relationship.
Impact angle of 4°.

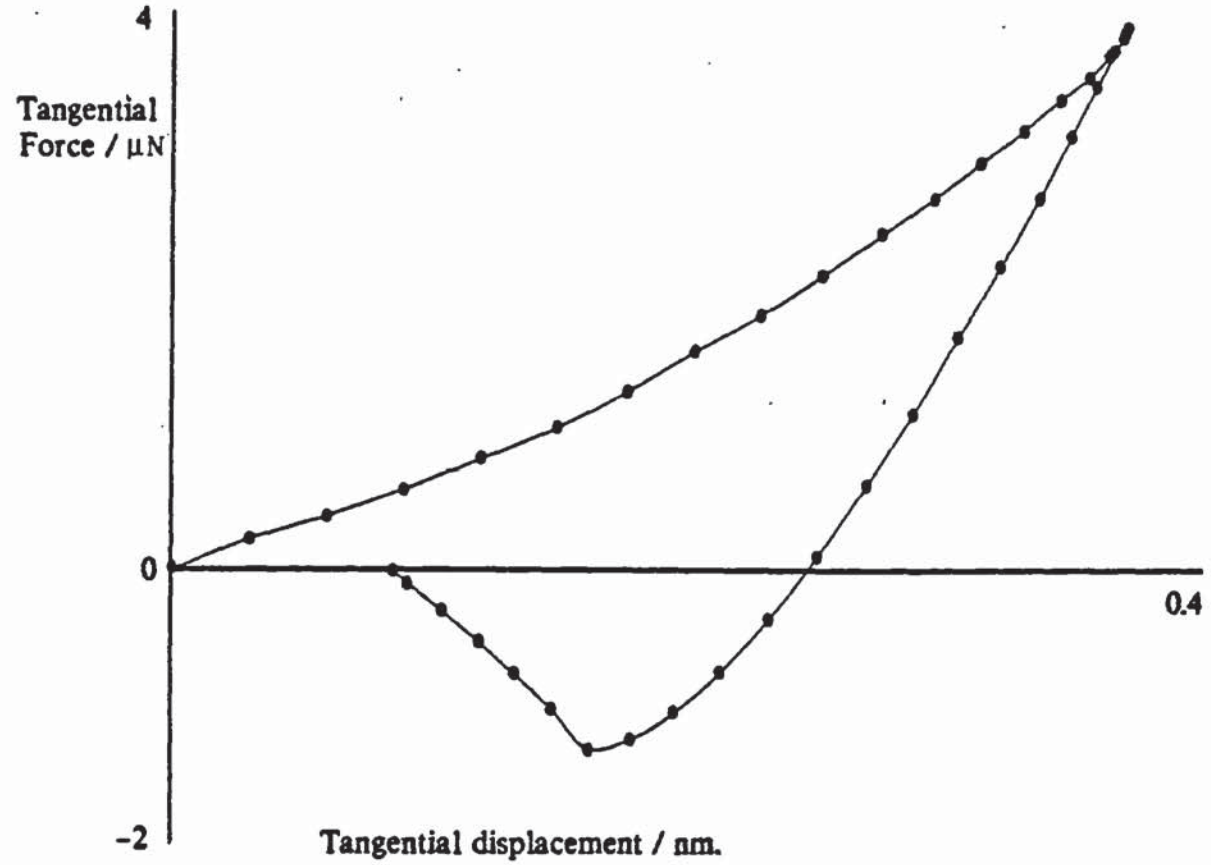

Fig. 5.15 Tangential force / displacement relationship.
Impact angle of 20°.

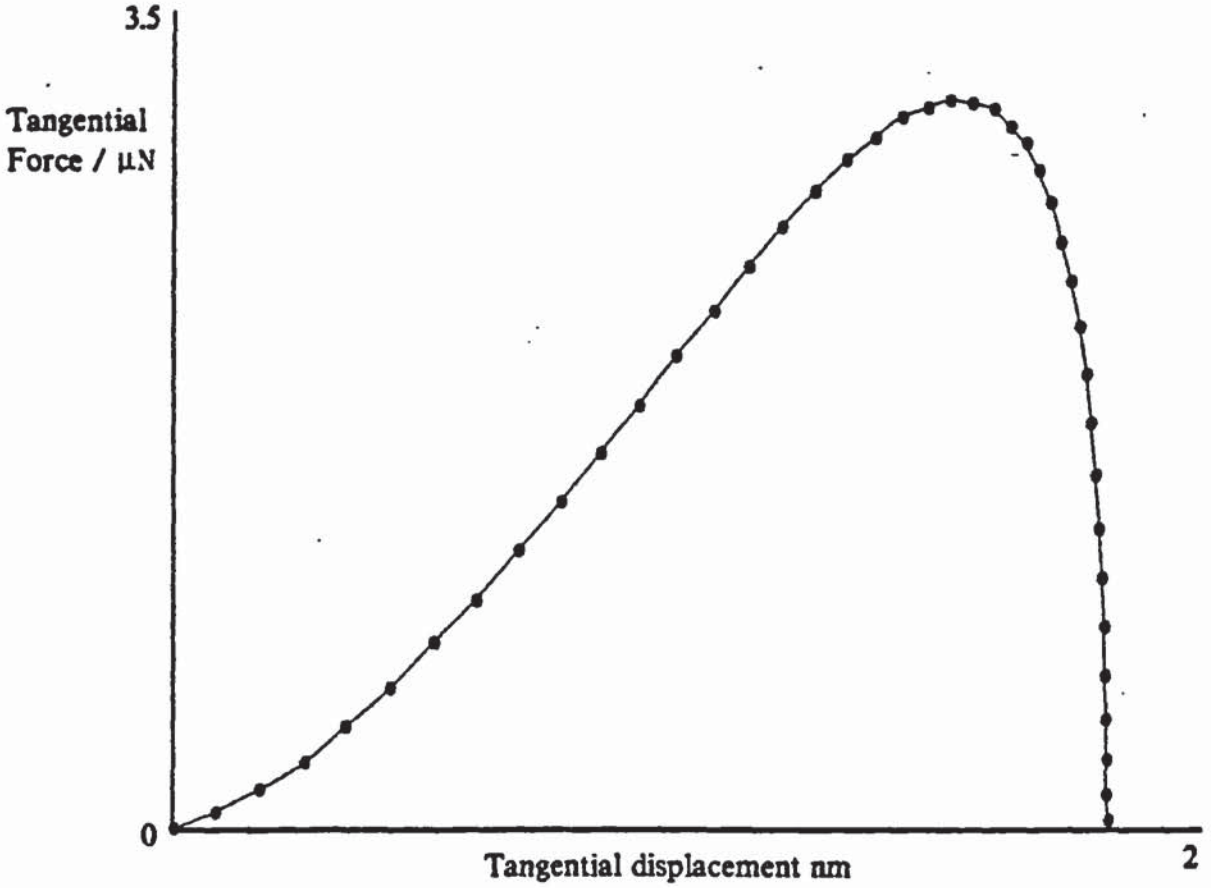

Fig. 5.16 Tangential force / displacement relationship.
Impact angle of 40°.

slip during the impact.

The behaviour of the intermediate region is illustrated in fig 5.15 for an impact angle of 20°. As the contact is initiated in rigid body sliding, which persists until the normal force has almost reached its maximum, irrecoverable strain energy is dissipated during this loading period. The tangential force reduces to zero and builds up in the negative loading direction which, upon reaching a maximum, initiates rigid body sliding once more in the opposite direction to the original. This causes further irrecoverable strain energy until the impact ends. It may be noted that, since the gradient of the curve indicates the sign of the tangential velocity, fig 5.15 confirms that the angle of reflection of the area on the sphere that forms the contact area is such that its position 'bounces back' towards the direction of impact. This was also reported by Maw (1976).

The behaviour for the third regime is typified by fig 5.16 which shows the tangential-force displacement curve for $\theta=40°$. For this case rigid body sliding occurs throughout the impact and fig 5.16 clearly shows no recoverable deformation.

Figure 5.17 shows the coefficient of restitution, calculated from the resultant particle velocities before and after contact, plotted against impact angle. The coefficient of restitution is equal to 1.0 for impact angles of 0 and 90°. Figure 5.17 indicates that for the properties used in the simulation the minimum coefficient of restitution occurs at an obliquity of 50°. This corresponds to a value of Ψ_1 approximately equal to $(4\chi-1)$ which is the boundary between impacts during which tangential force reversals occur due to sticking and impacts during which sliding occurs throughout.

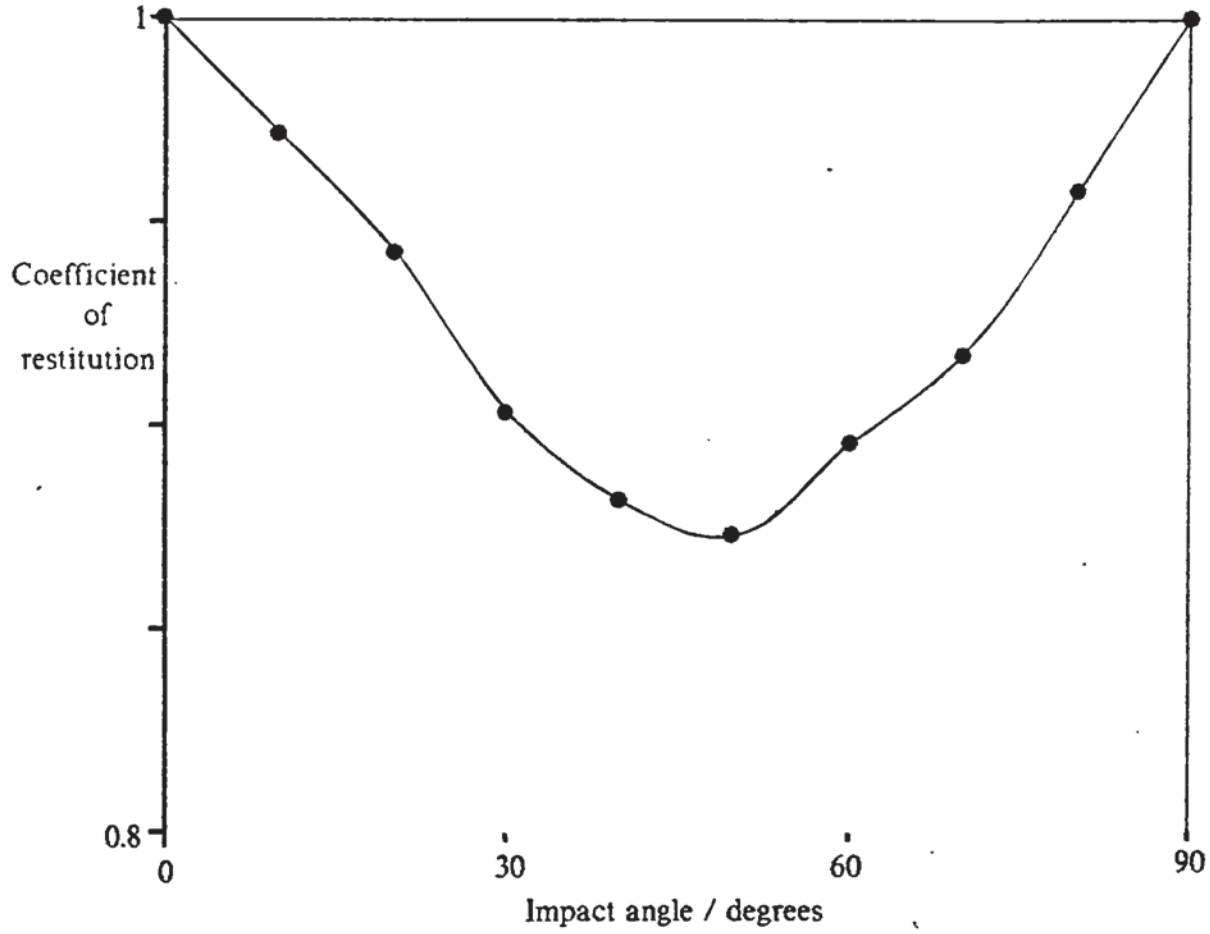

Fig 5.17 Coefficient of restitution against impact angle.

During an impact, the initial kinetic energy of the sphere is converted into three components of work done by the contact forces. The work done by the normal force is in the form of elastic strain energy which is fully recovered at the end of the impact. Work done by the tangential force is not fully recovered. Most of the energy dissipation is due to sliding but a small amount of energy loss occurs due to micro slip. In addition to the work done directly by the normal and tangential forces, the tangential force also produces a moment which results in the third component of work done in rotating the sphere.

For small angles of impact almost all the rotational and tangential work done is recovered, except for the tangential work done at the end of the impact when rigid body sliding occurs and thus more energy is dissipated. In addition, more rotational energy is expended due to the higher tangential force. When the obliquity is large enough to induce sliding throughout the impact duration then $T=\mu N$ and, since the normal force component decreases with increasing contact obliquity, the loss in kinetic energy decreases. Hence the coefficient of restitution increases until the limiting value of unity is reached at $\theta=90°$ when the normal force is zero.

In chapter 2 rigid particle simulations were reviewed which employ coefficients of restitution to simulate particle interaction laws, Campbell and Brennen (1982), (1985). The use of coefficients of restitution for particle simulations is appealing as it enables the adoption of coefficients obtained from experimental data. However, the implications of the work of Maw et al (1981) and the tests reported in this chapter show that for oblique impacts using a fixed

coefficient of restitution and calculating rebound angles from particle spin and impact angle is incorrect. In such simulations not only is the magnitude of the resultant velocity vector incorrect, but also its direction. Thus to accurately model the behaviour of oblique impacts in rigid particle simulations, functions must be introduced to represent rebound angles and velocities.

The oblique impact tests presented in this chapter give an average coefficient of restitution of 0.936 as compared to 0.93 over a similar range of impact angles which was reported by Maw et al (1981) as the average coefficient of restitution for the experiments using steel pucks.

It is concluded that the excellent agreement between the analytical and experimental results of Maw et al (1976), (1981) validate the program coding for dynamic impacts. It is worth noting that all the various loading and unloading cases for N increasing and N decreasing occurred in these 'simple' impact tests.

6. Applications to large systems of particles.

6.1 Introduction.

Having validated the program for quasi-static particle interactions and single particle oblique impacts, three test series were performed on large systems of particles in order to assess the performance of the program under conditions of rapid flow, arrested flow, and quasi-static deformation. The first two test series were carried out as final year undergraduate research projects and will only be briefly reported in sections 6.2 and 6.3. The third test series was performed as part of this research programme and will be covered in detail in the remainder of this chapter.

6.2 Hopper flow.

Platts (1989) simulated the flow of a monodisperse system of approximately 500 particles through wedge shaped hoppers with half angles of 45, 30 and 15°; and orifice widths of 5, 10 and 14mm. The spheres were of radius R=0.3mm and density $\rho=2.65Mg/m^3$, with elastic properties E=70Gpa, $\nu=0.25$ and the coefficient of inter-particle friction $\mu=0.35$. All the hopper walls had the following properties: E=210Gpa, $\nu=0.3$, $\rho=7.8Mg/m^3$, $\mu=0.15$.

The particles were randomly generated above the hopper wedge (fig 6.1a) and then subjected to a gravity field. Under the influence of gravity the particles fell to the bottom of the hopper (fig 6.1b). Flow was initiated by removing the horizontal wall at the orifice and is illustrated by the velocity vectors on the particles in fig 6.1c. The system was then cycled until all the particles had discharged from the hopper (fig 6.1d).

The simulations illustrated three regimes of particle flow.

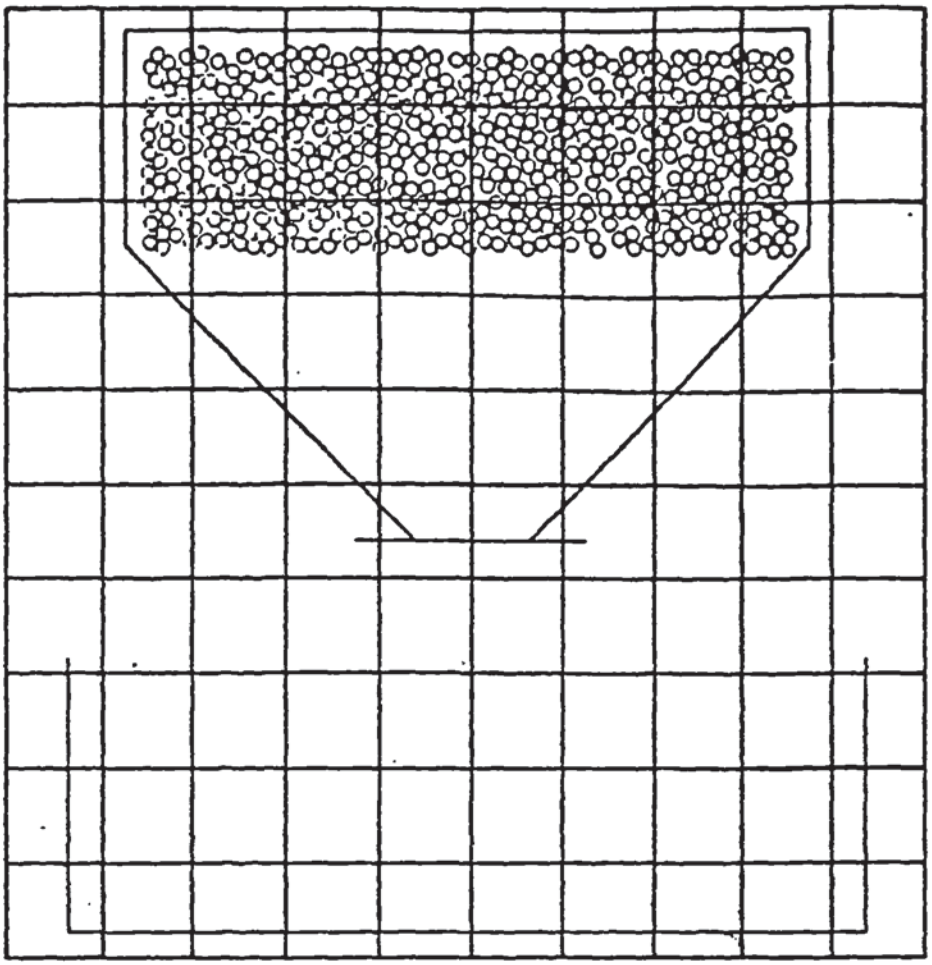

a) Initial generation

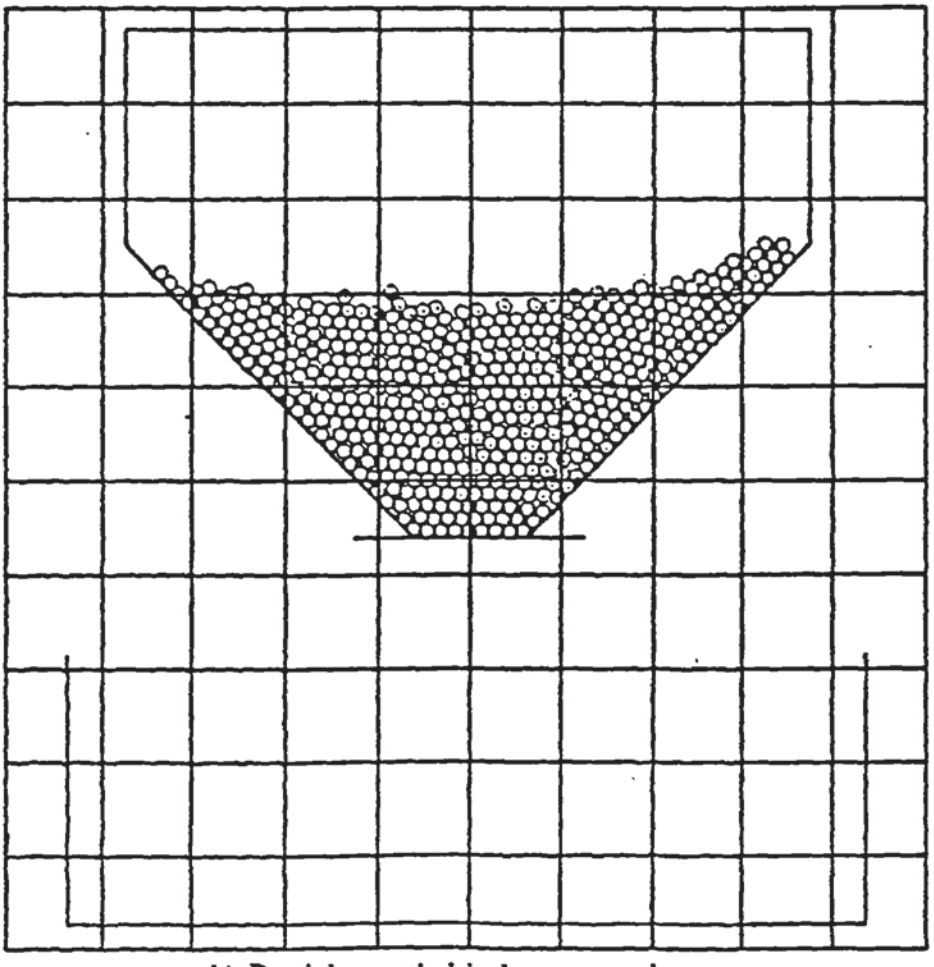

b) Particles settled in hopper wedge

Fig 6.1 Particles during hopper flow.

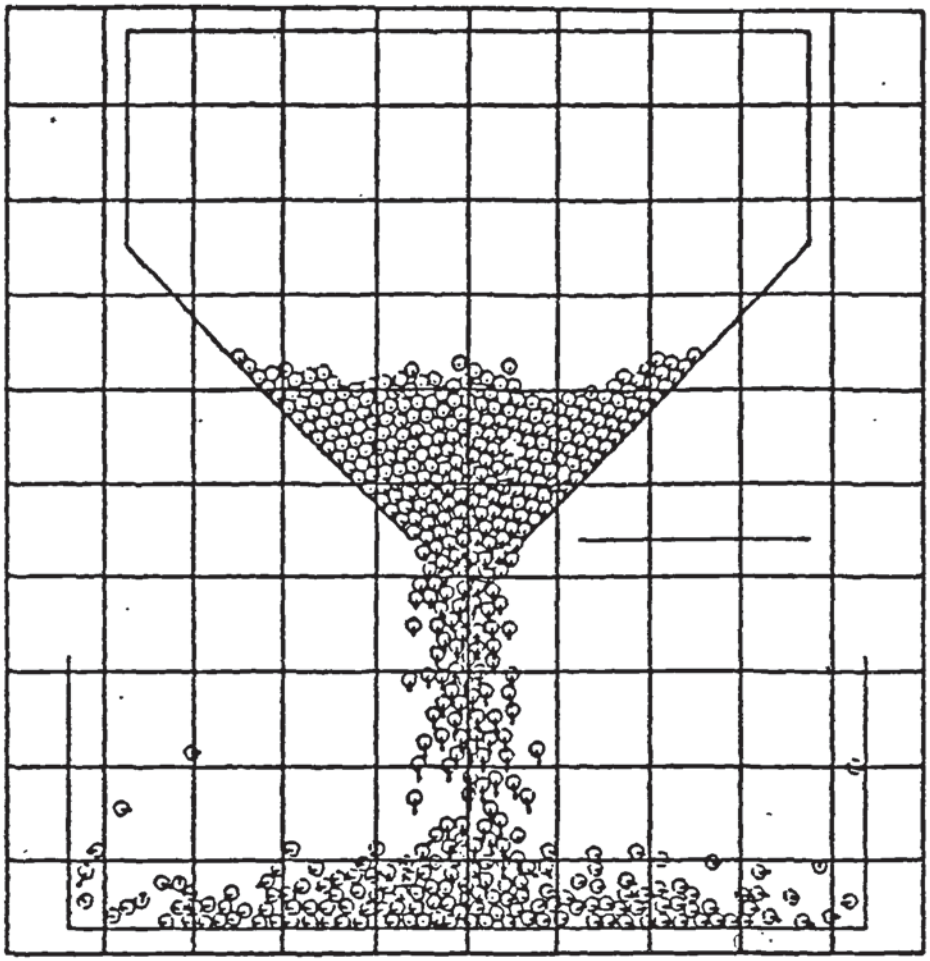

c) Initial flow stages

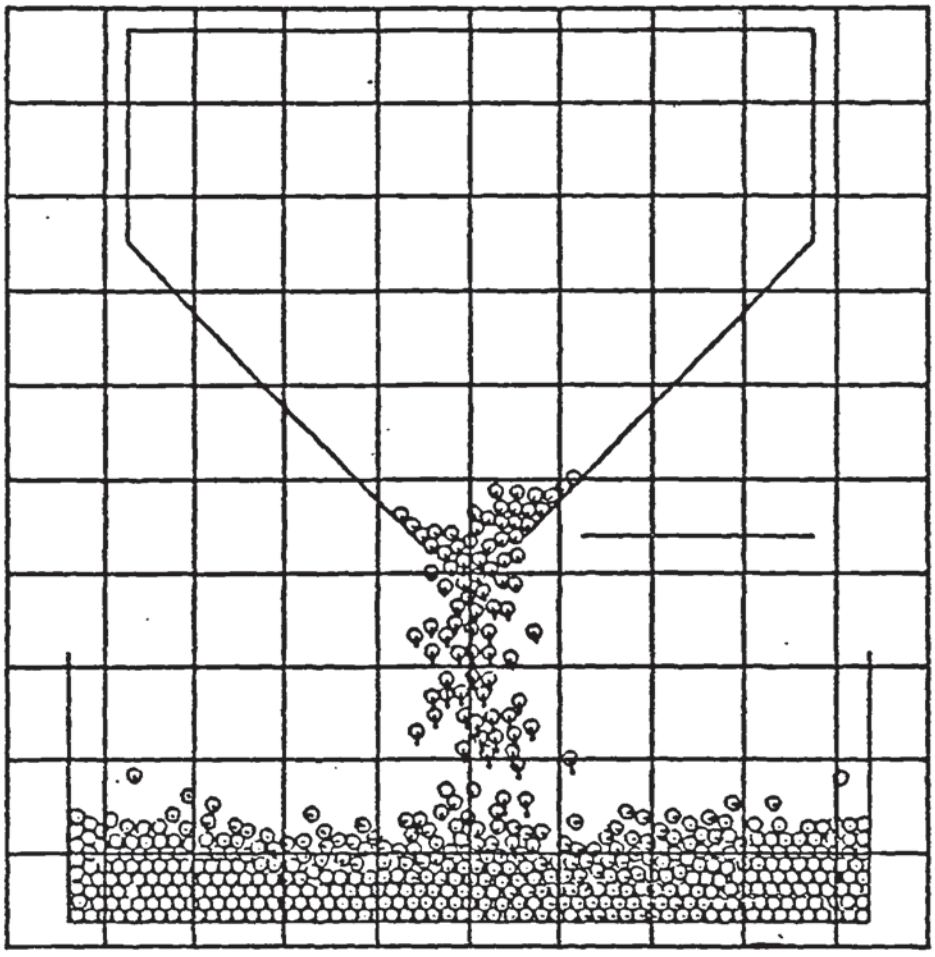

d) Final flow stages

Fig 6.1 Particles during hopper flow.

The initial acceleration stage, which then reaches a constant discharge rate which is maintained until the remaining particles are no longer sufficient to provide the required head for constant discharge, and the final flow stage where particles roll down the inclined hopper walls. It was also demonstrated that increasing the half-angle reduced the constant discharge rate and that there was a reduction in the time elapsed until constant discharge was achieved. Increasing the orifice width increased the discharge rate, although it did not seem to affect the duration of the initial acceleration stage.

The flow patterns observed in the simulations are illustrated in fig 6.2 by the velocity vectors of the particles. For small half-angles the flow of particles was radial with all particles flowing to the virtual apex of the inclined walls. For larger half-angles more complex flow behaviour was observed. Adjacent to the hopper walls slow moving zones of material were noted, whereas immediately above the hopper orifice a region of rapid particle motion occurred as particles fell from the hopper. This region was fed by the zone of particles immediately above.

For the hopper simulations it was necessary to add the facility to separately specify the contact damping for particle-wall contacts. This was in order to account for energy losses due to the 'massive' nature of the walls in comparison to the particle size. With this modification the program performed well and it was concluded that although a relatively small number of particles was used, the results gave good agreement with the phenomena reported for real hopper flows. Information on stress, strain and wall pressure distributions could not be made, due to the small

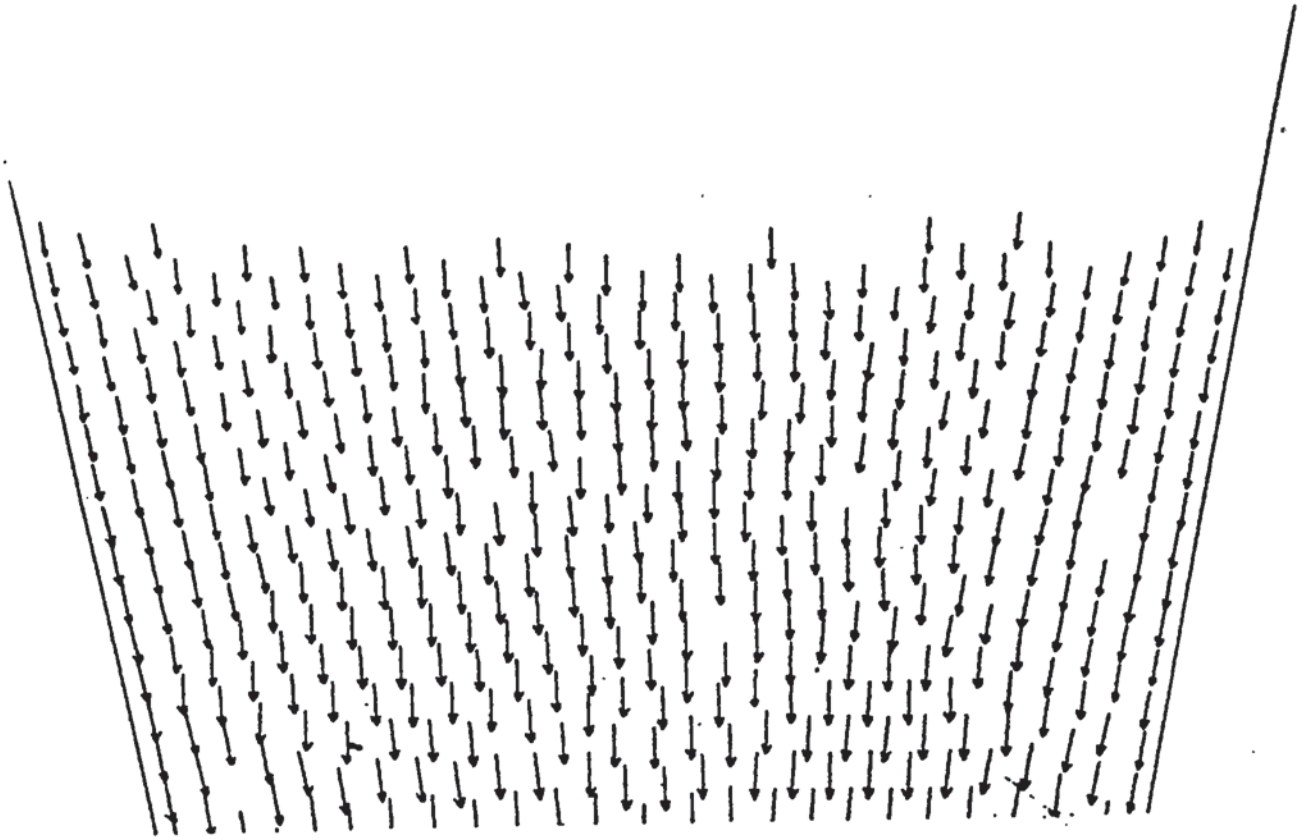

Particle velocities for a 15° half angle hopper

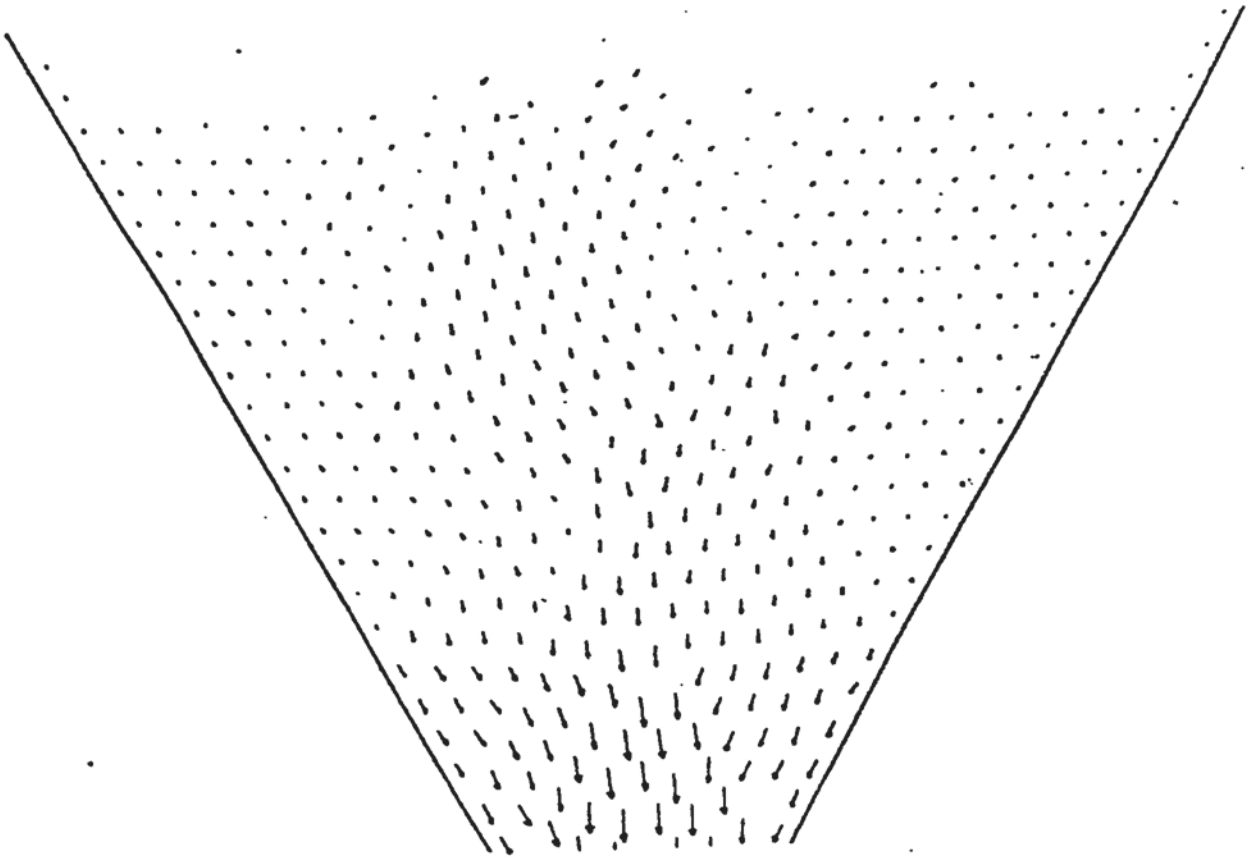

Particle velocities for a 45° half angle hopper

Fig 6.2 Flow patterns during hopper flow.

numbers of particles, but these initial tests indicate that simulations using many thousands of particles would be a useful future application.

6.3 Pluvial deposition.

Another application of the program is the simulation of the deposition of an assembly of particles into a container. Webster (1989) investigated the deposition of three different assemblies of approximately 500 particles. To simulate pluvial deposition the desired particle sizes and distribution were generated in a rectangular area. A gravity field was applied and the particles then fell as a rain into a previously defined container. As a consequence particle-particle and particle-wall interactions occurred and some of the phenomena reported by other researchers, such as arch formation and collapse at the corners of the container, were observed. During the deposition phase the time step was based on the Rayleigh wave speed. However, once the system approached equilibrium as the particles began to settle, the time step was too large and apparent numerical instabilities occurred which were avoided by reducing the time step. Figure 6.3 illustrates a pluvially deposited bed of particles.

6.4 Isotropic compression.

Most of the previous research on computer simulated experiments using the methodology of Cundall and Strack (1979) has been concerned with the quasi-static shear deformation of large assemblies of particles. However, it is first of all necessary to simulate the sample preparation stage. Initially particles are generated randomly within a prescribed

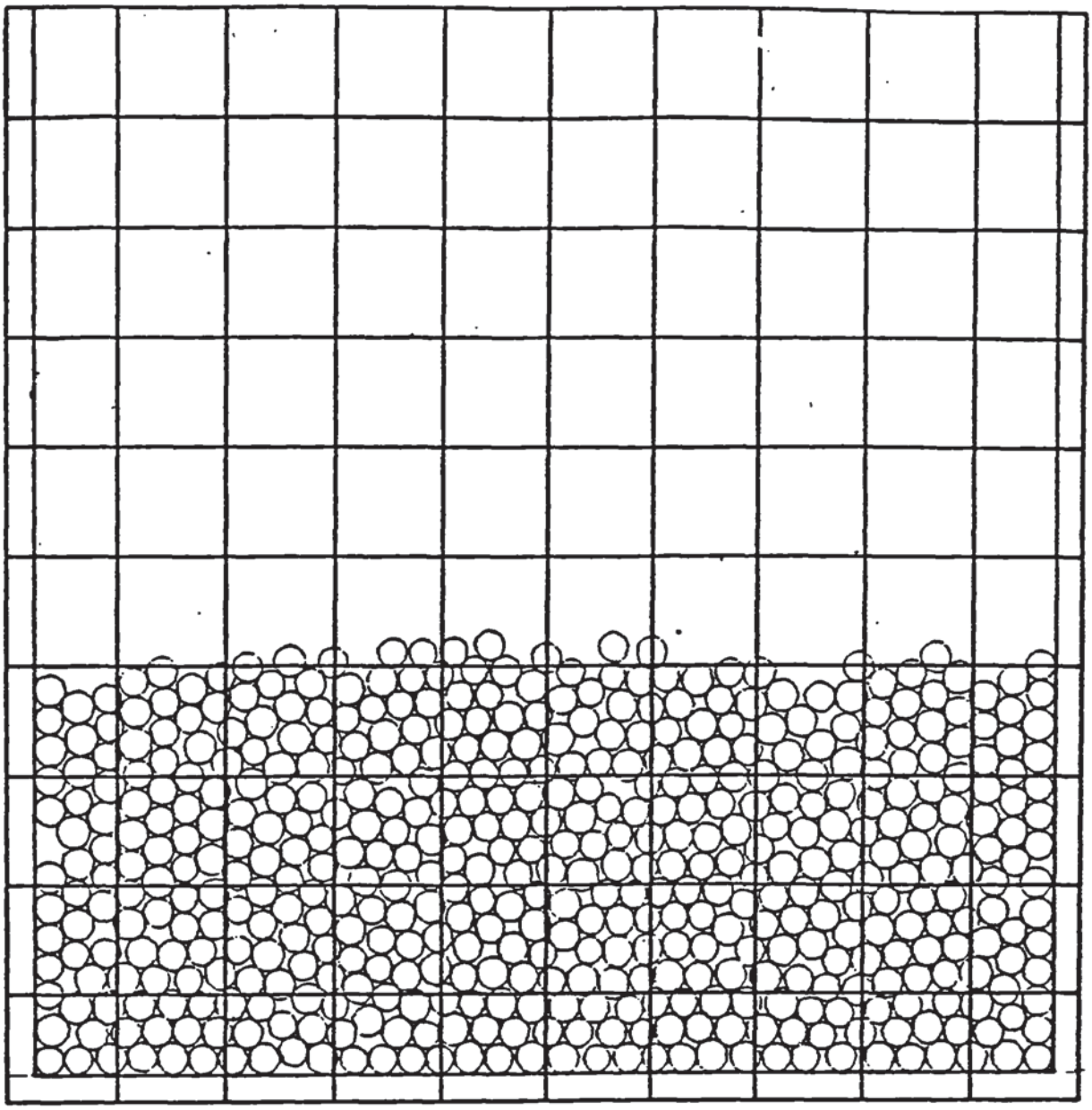

Fig 6.3 Pluvially deposited bed of particles.

area and in such a way that there are no initial contacts. The system of particles is then subjected to a simulated compression stage in order to create a compact assembly that can be subsequently sheared.

6.4.1 Choosing a boundary control.

The original method of particle generation produced assemblies of around 55% porosity. Compression was achieved by applying a strain controlled boundary to the assembly until the desired isotropic stress state was reached. At this stage the assembly would typically have a porosity of around 15%.

One drawback of using a strain controlled boundary is that due to the large amount of compaction required to reduce the porosity from 55% to 15% the overall assembly size decreased considerably. As the boundary is initially fixed at generation, and any particle that more than half crosses the boundary is then incorporated into it, once the assembly reaches 15% porosity there are so many 'boundary particles that the overlaps between them are orders of magnitude larger than those occurring within the assembly. The consequent large inter-boundary particle forces can affect the behaviour of particles adjacent to the boundary, and this is one of the reasons that the regions used for analysis are always well within the boundary and away from these effects. A further drawback of compacting the assembly with a strain controlled boundary is that once compacted, and with the high locked-in inter-boundary particle forces, changing to a stress controlled boundary for a constant mean stress test means that the stress applied must be sufficient to retain the high forces on the boundary, otherwise particles will be

ejected. Thus the applied stress must be much higher than the isotropic stress inside the assembly and hence will cause further compression.

Another consideration is the shape of the assembly after isotropic compression. With strain control the boundary remains circular. With a stress controlled boundary the boundary does not remain perfectly circular but becomes uneven in shape. This is due to a fixed force being applied to all boundary particles. Once contacts occur between boundary and internal particles resistance to the applied force will occur. The magnitude of the resistance to the applied boundary force will depend on the structure of the assembly in the region of the boundary particle under consideration. Thus as the assembly is not homogeneous some boundary particles will move farther in the applied force direction than others and an uneven boundary shape will result. This unevenness, especially when a strain controlled boundary is subsequently used, causes local shear instabilities close to the boundary.

Ideally the assembly at the end of the isotropic compression stage should be at the selected mean stress and have a circular boundary and as few high inter-boundary particle overlaps as possible.

6.4.2 Preliminary tests.

Preliminary tests were carried out prior to the successful implementation and validation of the tangential force-displacement laws of Mindlin and Deresiewicz (1953). In these tests the normal Hertzian force-displacement law was used, together with a linear approximation developed by Mindlin (1949) for the tangential force-displacement law

based on the initial stiffness of the contact.

In order to avoid particle congestion around the boundary, section 6.4.1, an alternative technique was adopted. The method used was to apply a centripetal gravity field to the system. Thus all the particles would travel together towards the centre. The centripetal gravity field was set up and the system cycled so that the compact assembly developed from the centre. Zero contact friction was employed as this stopped the build up of any oblique forces and thus enabled the assembly to more easily achieve its densest packing state, as reported by Barnes (1985). The use of the centripetal gravity field resulted in large forces in the centre of the assembly which decreased in magnitude as they radiated to the boundary, fig 6.4. Calculation cycles were continued until all particles had come into contact. A boundary was then defined, the gravity field was removed, damping was introduced, contact friction was added and the system was cycled to equilibrium. The density of the resultant assembly is illustrated by the porosity variation through the assembly in fig 6.5. This shows that the assembly was not uniformly dense, being denser in the centre of the assembly.

A boundary stress tensor was then prescribed to enable the assembly to reach an isotropic stress of 100kPa. The system was cycled until a quasi-equilibrium state was reached. The contact force distribution at this point is shown in fig 6.6. A quasi-equilibrium state was assumed when the out of balance forces in the assembly were an order of magnitude less than the contact forces.

The assembly was then subjected to an increasing deviator

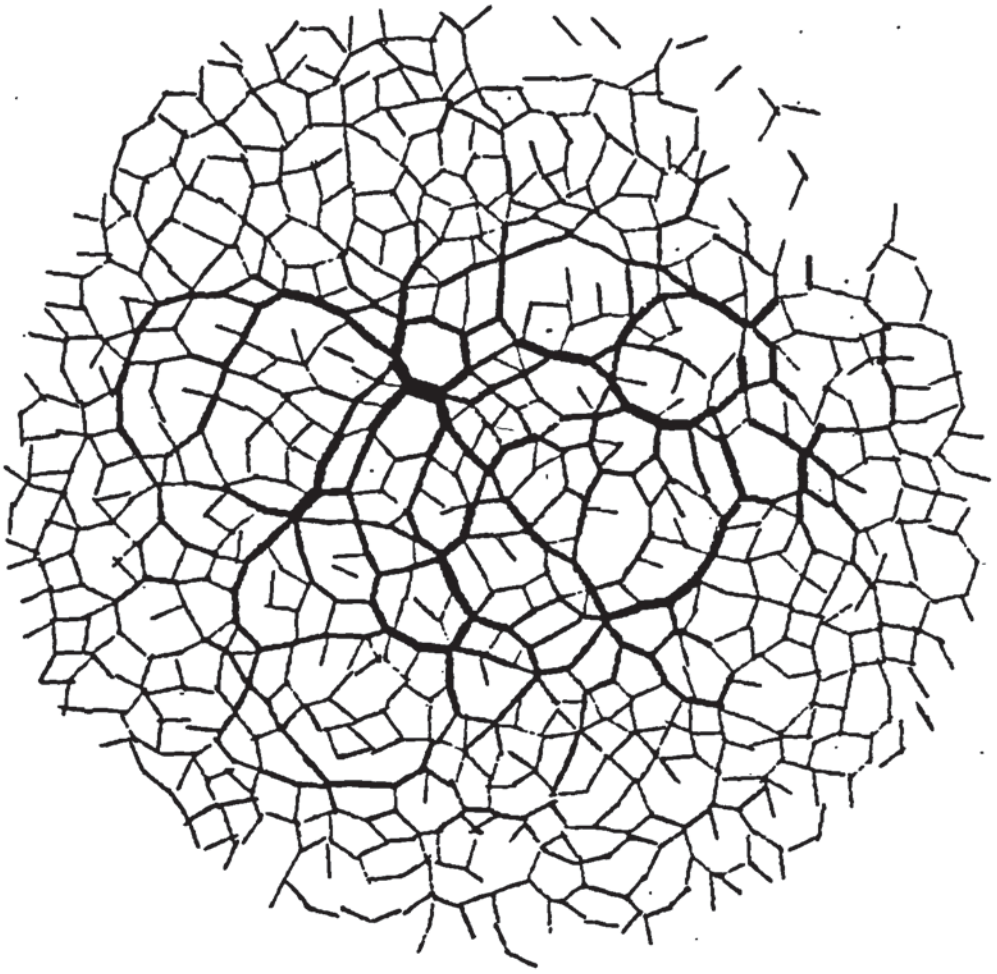

Fig 6.4 Contact force distribution after centripetal compression.

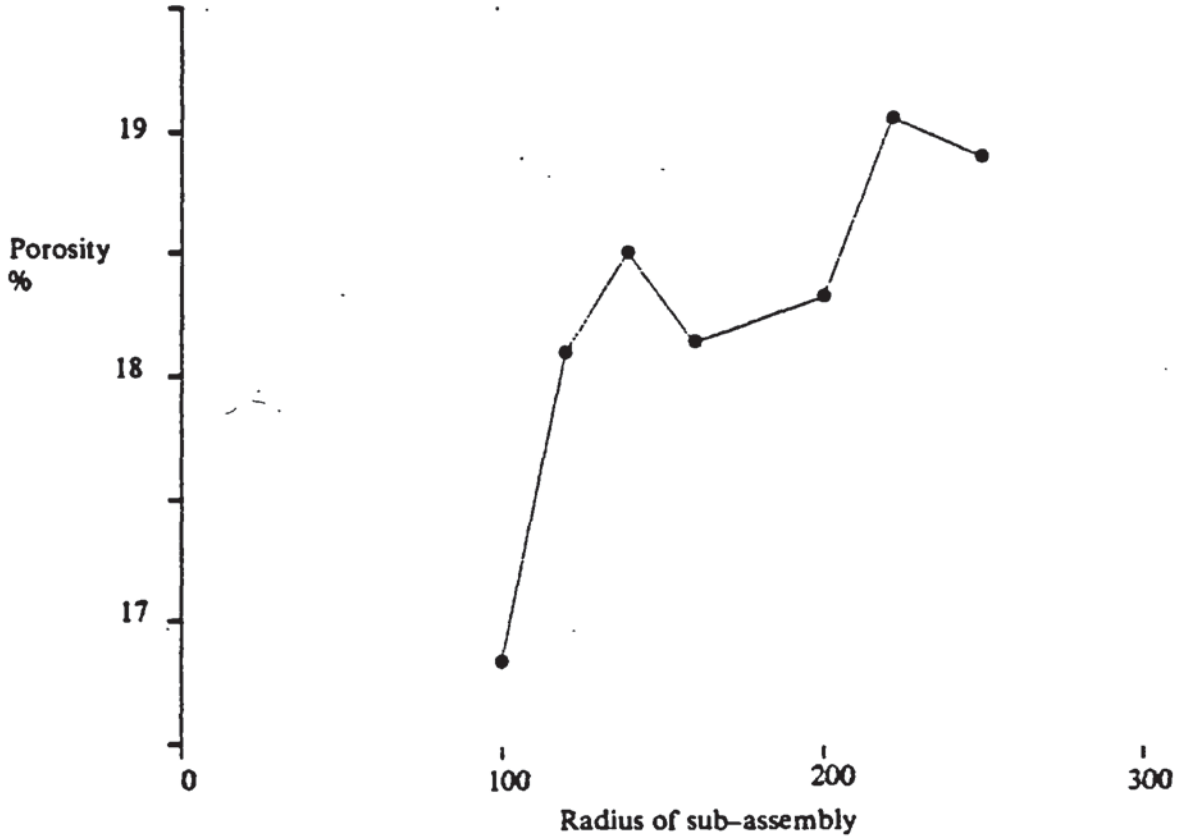

Fig 6.5

Porosity variation through assembly after centripetal compaction.

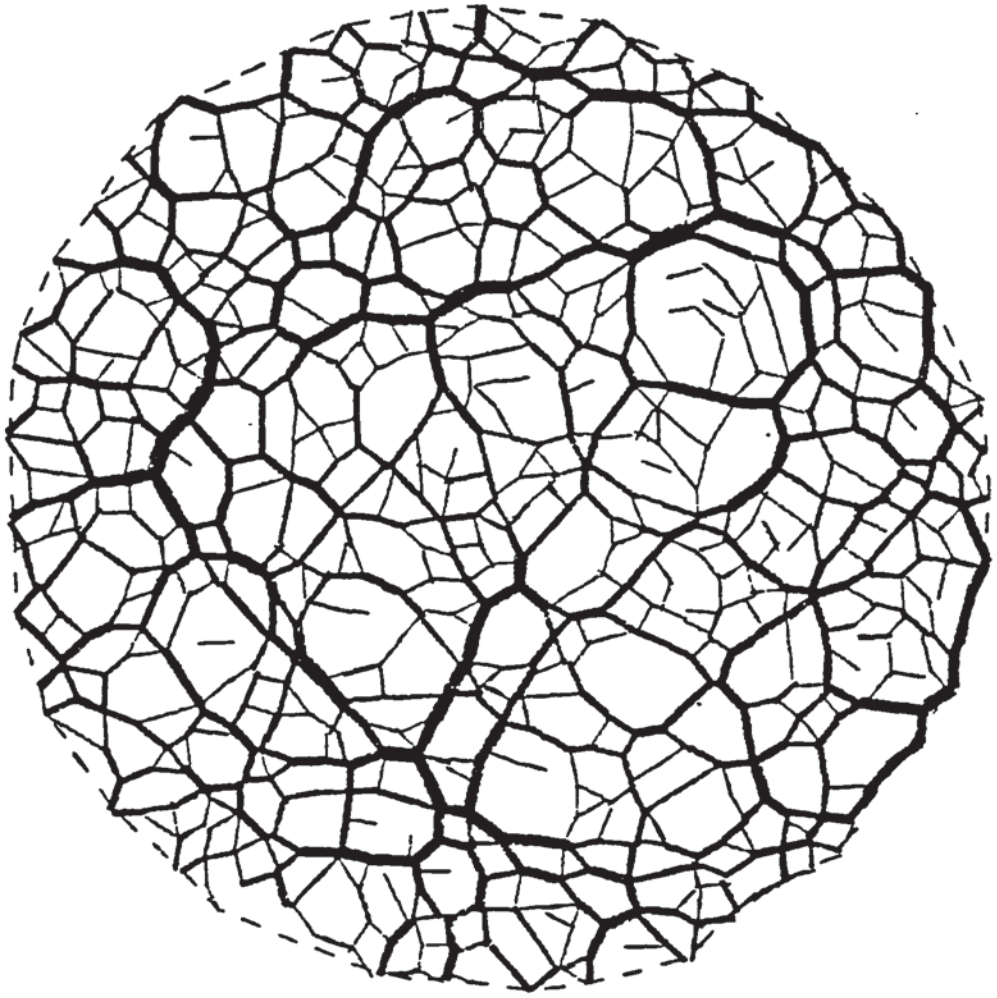

Fig 6.6 Contact force distribution of assembly at 100kPa isotropic stress.

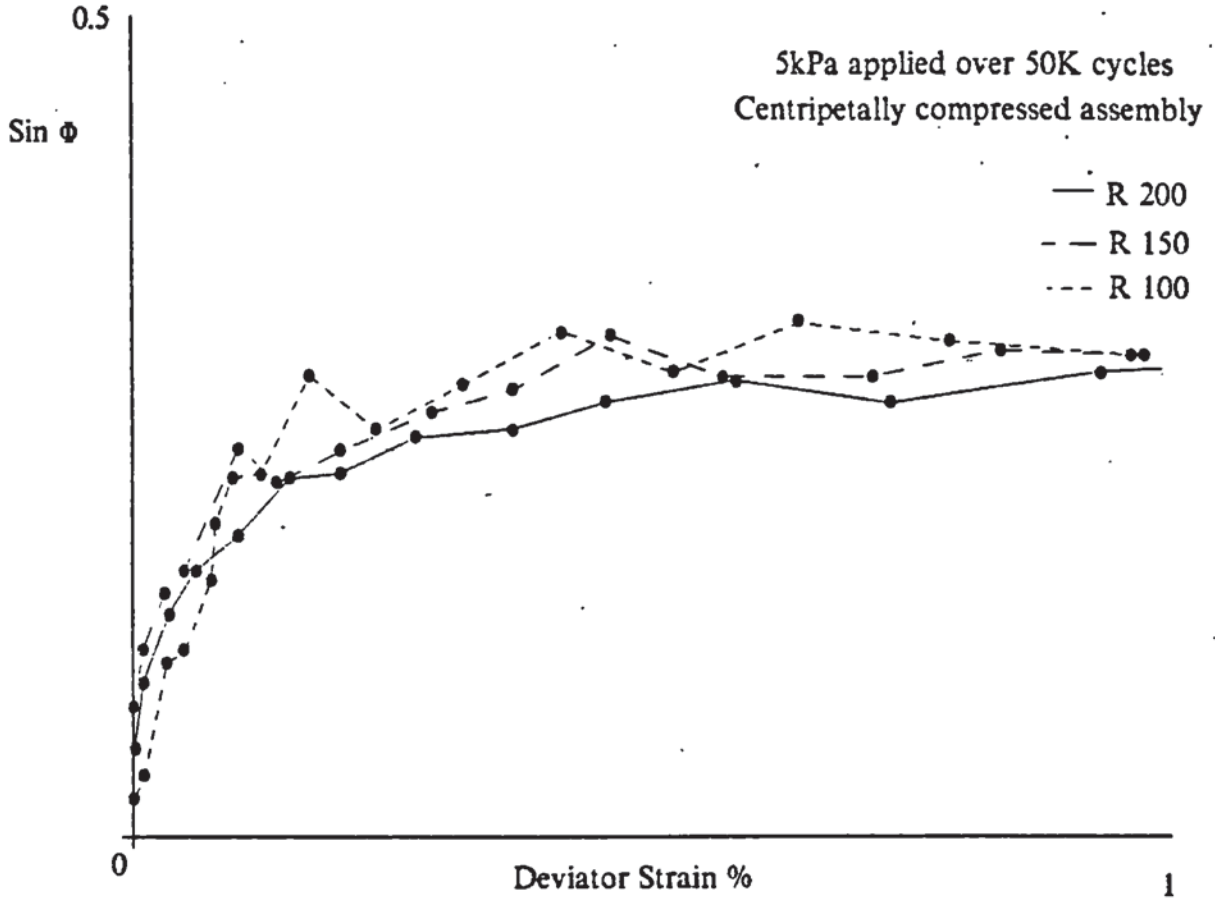

Fig 6.7 Sin Φ plotted against deviator strain for constant mean stress test.

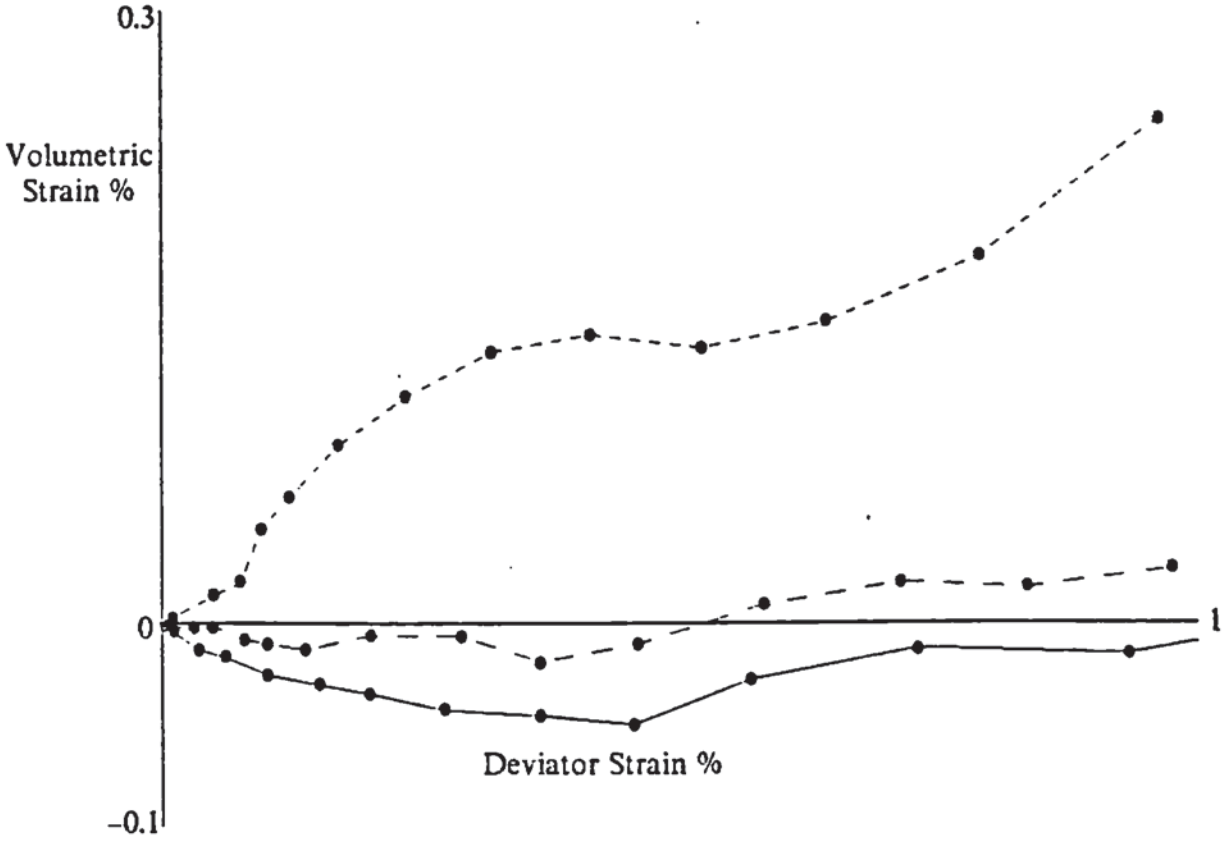

Fig 6.8 Volumetric strain plotted against deviator strain for constant mean stress test.

stress with the mean stress held constant. Figures 6.7 and 6.8 illustrate the variation in the mobilized angle of shear resistance (sin Φ) and the volumetric strain plotted against the deviator strain. Three different circular regions of radii 100, 150 and 200mm were used for analysis. These represent 15, 34 and 62% of the total number of particles in the assembly respectively. The effect of the centripetal compaction on the behaviour of the assembly is best illustrated by fig 6.8. This shows that the volumetric strain, as measured inside the largest radius, indicates that the assembly undergoes initial contraction, which once the system reaches a value of around 0.5% deviator strain then begins to expand. This expansion continued until the end of the test. In contrast, the smallest region expanded from the start of shear. This is because the central region was so dense that expansion was necessary for the particles to accommodate the shear deformation, a phenomena well documented in the shearing of dense granular media. Although the evolution of sin Φ illustrated in fig 6.7 shows reasonable close agreement for the three regions it is clear from fig 6.8 that the centripetal compaction did not lead to uniform volumetric strain behaviour due to the density variation. The centripetal compaction option was therefore not subsequently used in the research programme.

In order to prepare a dense assembly of particles more efficiently the particle generation algorithm was re-coded, as described in section 4.4. This produced a much more dense assembly on generation and using this technique in conjunction with increasing the number of small particles resulted in an assembly with very few large voids, as shown in fig 6.9. At the same time as these new methods were introduced

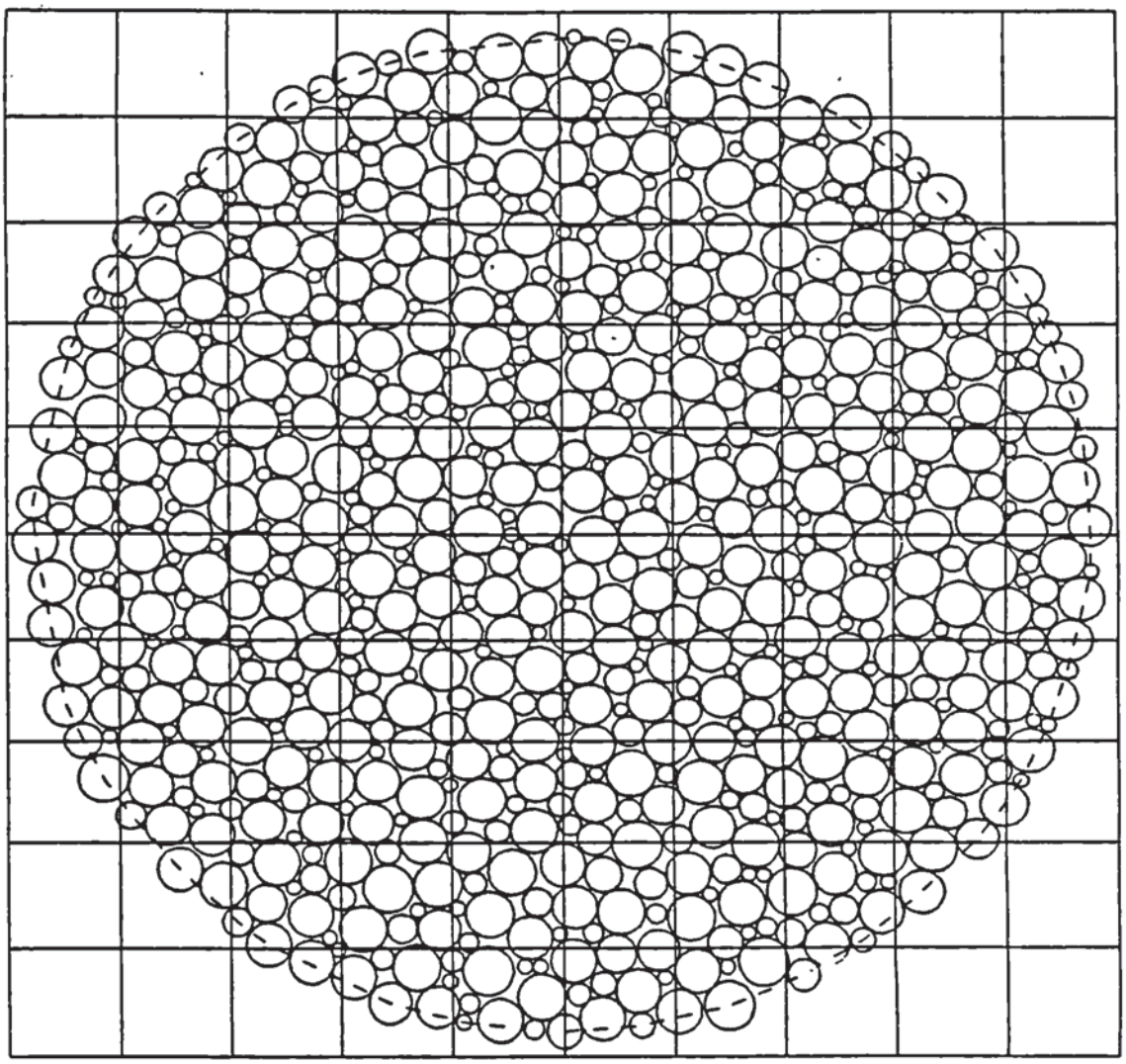

Fig 6.9 Assembly generated using new generation algorithm.

the program was re-coded to use the equations of Mindlin and Deresiewicz (1953), a time step based on the Rayleigh wave speed, and the adoption of S.I. units, as described in Chapter 4.

Once the new assembly had been generated, to achieve the desired isotropic stress the boundary was then subjected to an isotropic strain rate tensor. However, instabilities occurred. The mechanism that caused these instabilities was that, as force chains developed through the assembly, a particle would be caught in the chain and the particle, due to the buckling of the chain as the assembly was compressed and the lack of lateral restraint from adjacent particles, would be ejected at a high velocity. The particle would then impact other particles which, if not sufficiently laterally restrained, would also start to move at high velocity impacting other particles thus causing the effect to 'snow-ball'. For a particle moving at a high velocity, given its elastic properties and the momentum of the particle, the impact force (represented by particle overlap) and duration of the contact can be calculated. However, if the time step for the simulation is too large the simulation will cause the particle to travel too far in one time step such that the inter-particle overlap generated is larger than that which would occur from momentum considerations. This in effect adds energy to the system and the resultant momentum of the particles after impact would be larger than before. This further compounds the instability of the assembly and chaos ensues. These instabilities occurred with assemblies with various gradings although as the max/min particle size ratio was increased the instabilities occurred more frequently. For assemblies with a more uniform grading lateral

restraint is more readily available.

It was anticipated that these instabilities could only occur when there was a lack of lateral restraint in the system i.e. a relatively unloaded system. Thus for a system with an essentially uniform grading, once the desired mean stress of around 100kPa has been achieved, it was not anticipated that these problems would occur. However, it was not possible to achieve the desired mean stress without this phenomena occurring, even when very small boundary strain rates were applied.

6.4.3 Isotropic compression of uniform and graded assemblies.

In an attempt to achieve the goals detailed in section 6.4.2 and to avoid the instabilities which occurred with previous assemblies, a new form of assembly control was developed which was termed the continuum coding, section 4.5.2. In addition it was decided that, as the current simulation program can not fully handle plastic deformation, for contacts which approach the initiation of plastic yield it was necessary to suppress the contact development. This was achieved by determining the overlap for each contact and if the overlap was greater than 7% of the diameter of the smallest particle in contact, the value of the contact damping was set to the critical value. The number of times this was done during a period of cycling was then printed out as a warning to the user that the system was not operating in the elastic range.

Two tests were initiated using the new coding. In both assemblies the particle properties were identical, E=70Gpa,

ν=0.25, μ=0.3, ρ=2.65Mg/m^3. For both tests 10% contact damping was used. The particle size distributions are given below and the assemblies, as generated, are illustrated in figs 6.10-6.11.

'Uniform' assembly

Particle radius mm	Number of particles
0.6	70
0.59	80
0.58	100
0.57	100
0.56	120
0.55	120
0.54	26
0.53	11
0.52	11
0.51	7
	645

'Graded' assembly

Particle radius mm	Number of particles
0.92	30
0.76	138
0.61	172
0.46	230
0.31	30
	600

The first assembly had 645 particles with ten different particle sizes, and a max/min particle size ratio of 1.2, hence simulating a polydisperse but very uniformly graded assembly. The second assembly had 600 particles with five different particle sizes with a max/min particle size ratio of approximately 3, such that the sizes and proportions of each were the same as those used by Barnes (1985) in his 1000 disc assembly. This is so comparison can be more easily drawn between the behaviour reported by Barnes (1985) and the current tests.

Both assemblies were isotropically compressed, with zero inter-particle friction, to approximately 100kPa using a strain controlled boundary with a corresponding continuum strain rate tensor. Once a value close to the desired isotropic stress had been attained both strain rate tensors were set to zero and the system cycled until a quasi-equilibrium state was reached. This state was characterised by out of balance forces an order of magnitude less than

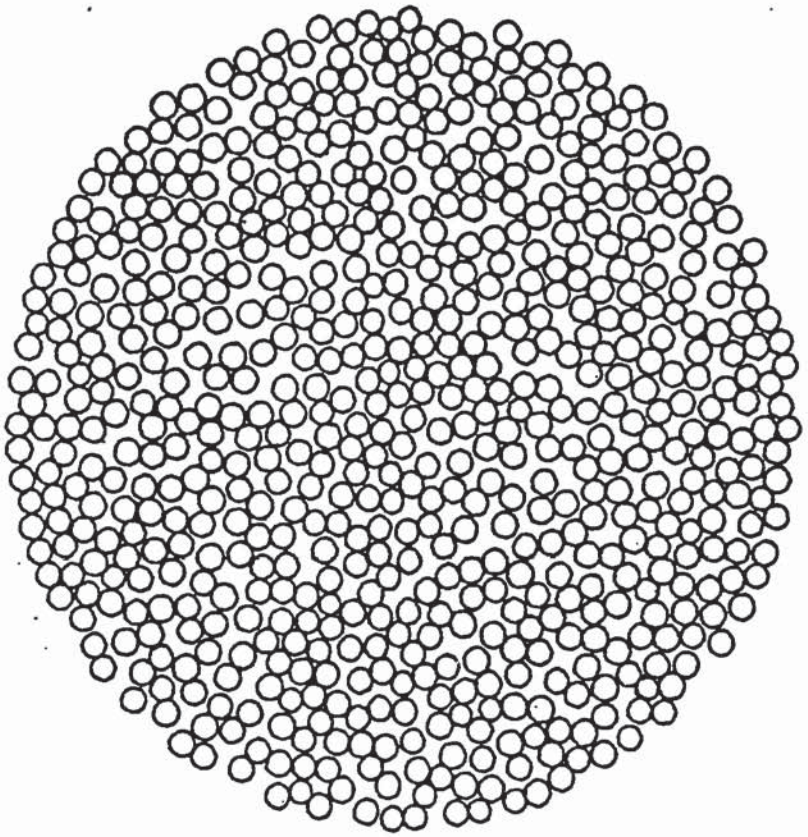

Fig 6.10 Uniform assembly as generated.

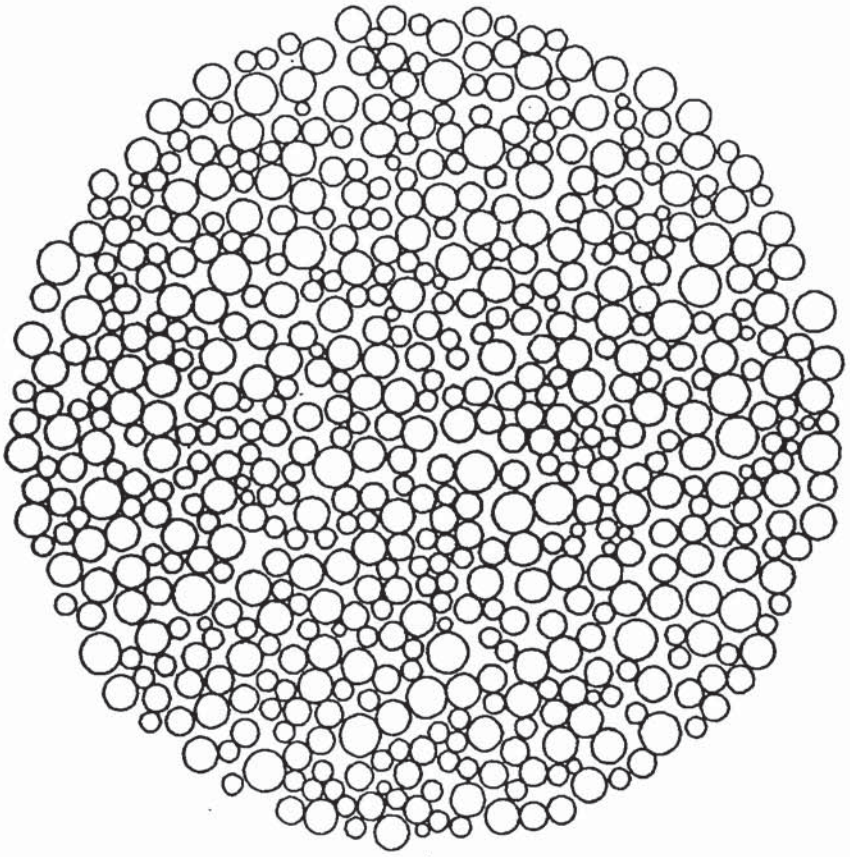

Fig 6.11 Graded assembly as generated

contact forces and extremely small velocities. Inter-particle friction of 0.3 was then added and the system cycled and checked for continuation of quasi-equilibrium. The assemblies in this state are illustrated in figs 6.12 and 6.13. Figure 6.14 shows the 1000 disc assembly of Barnes (1985) for comparison.

For an applied isotropic stress of approximately 100kPa the maximum and average contact force for the uniform and graded assemblies are: 0.53N, 0.143N, 0.59N and 0.123N respectively. No quantitative comparison can be drawn with the 1000 disc assembly since Barnes (1985) used linear springs to model the particle interactions. The average coordination number was 3.15 for the uniform and 3.57 for the graded assembly. The difference is due to the large particles in the graded assembly which can easily accommodate five to six contacts. Comparing the distribution of contact forces in fig 6.13 to the 1000 disc test, illustrated in fig 6.14, similarities can be noted. The force chains are randomly distributed and form curves, generally without abrupt changes in direction. In contrast the force distribution for the uniform assembly, shown in fig 6.12, is dominated by straight chains with sudden direction changes. The domination of the straight force chains in assemblies of uniform particles was also reported by Petrakis et al (1988), reviewed in section 2.3. Due to the existence of zones of regular packing the alignment of particles in the uniform assembly enables the transmission of forces in roughly straight chains, whereas the graded assembly can be seen to have very few particles whose centroids lie on a straight line.

Figures 6.15-6.17 illustrate the distribution of contact

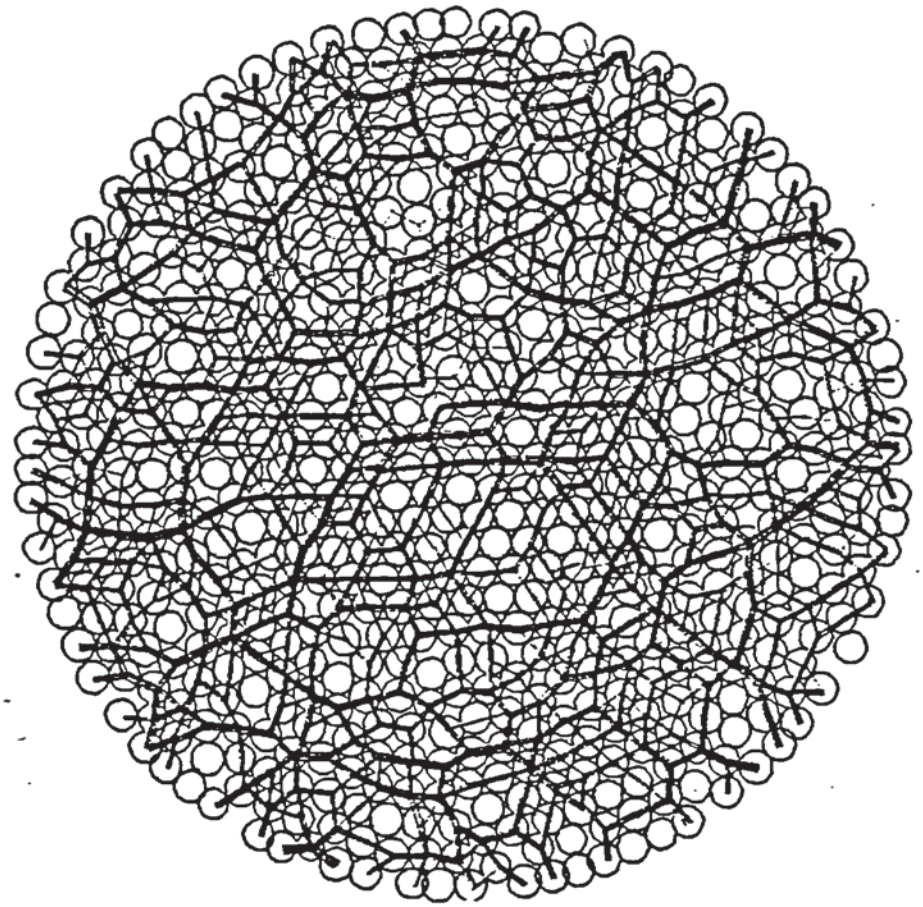

Fig 6.12 Contact force distribution for uniform assembly in quasi-equilibrium.

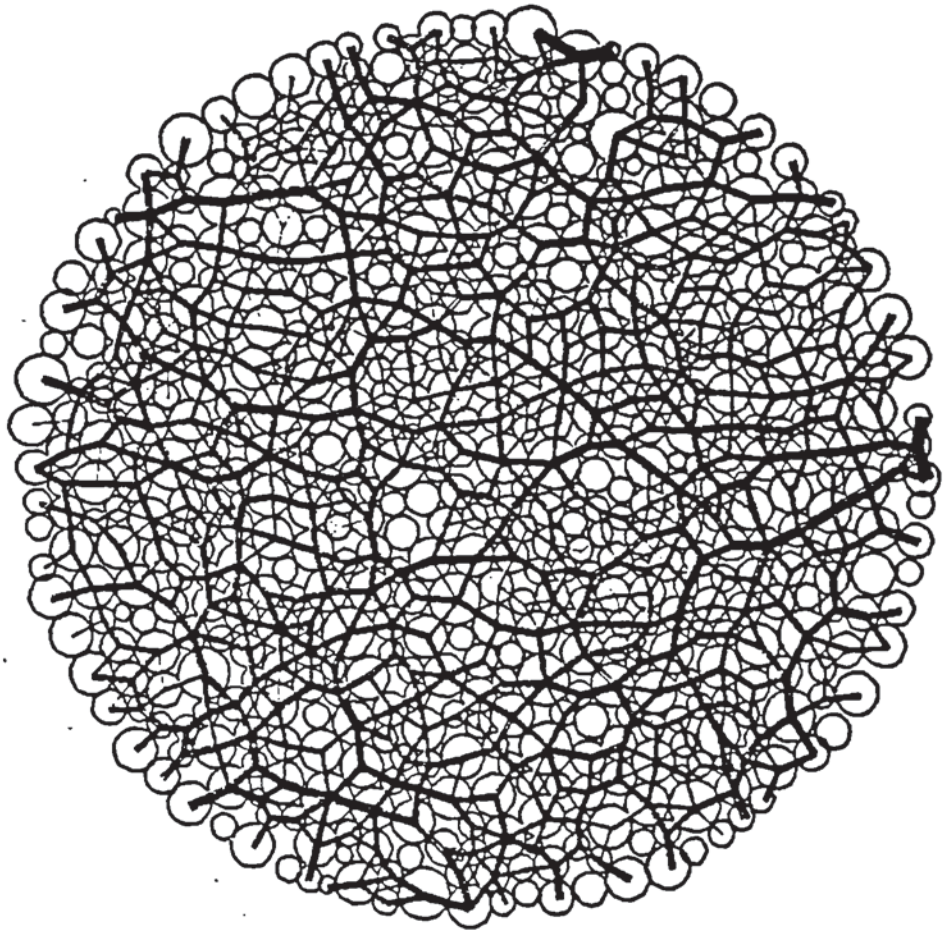

Fig 6.13 Contact force distribution for graded assembly in quasi-equilibrium.

Fig 6.14 Contact force distribution for 1000 disc assembly in quasi-equilibrium Barnes (1985).

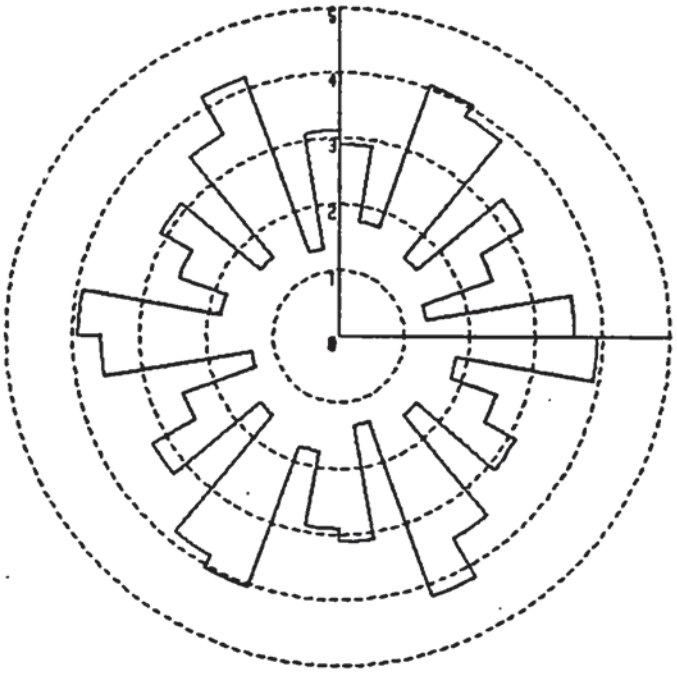

Contact normal vectors

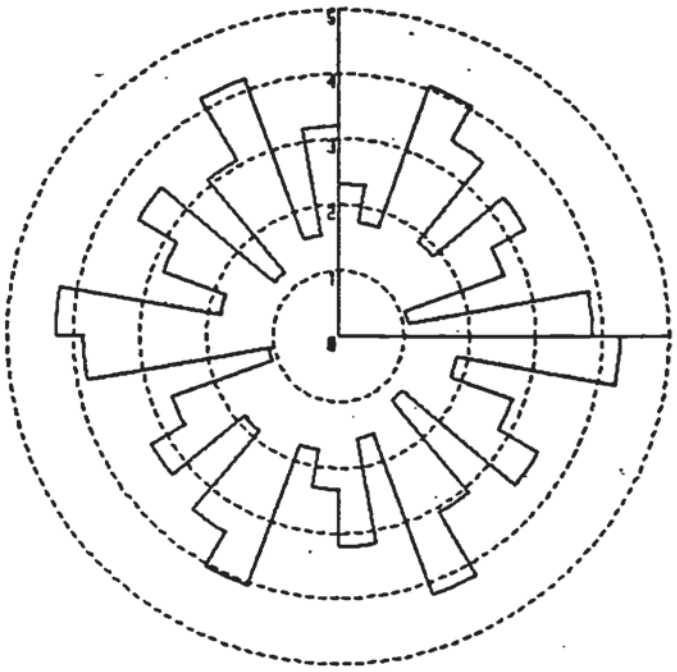

Weighted contact normal vectors

Fig 6.15 Distribution of contact normal vectors and contact normal vectors weighted to the normal force for uniform assembly in quasi-equilibrium.

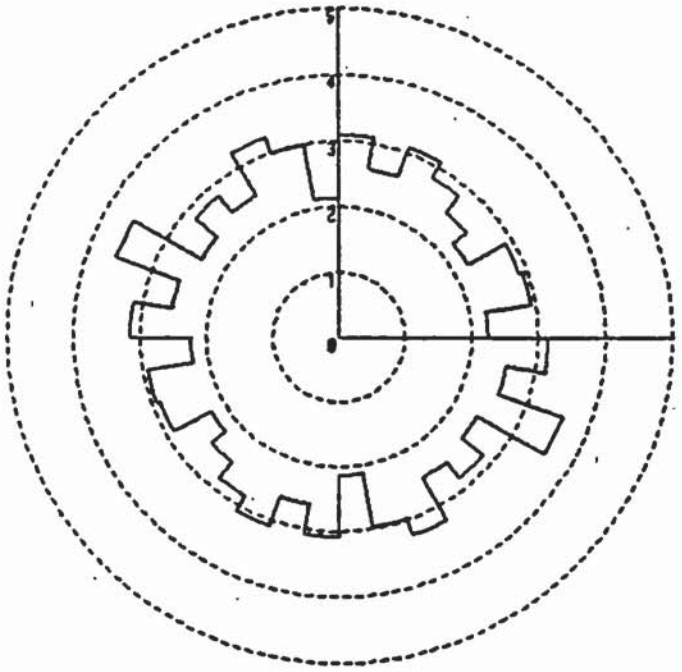

Contact normal vectors

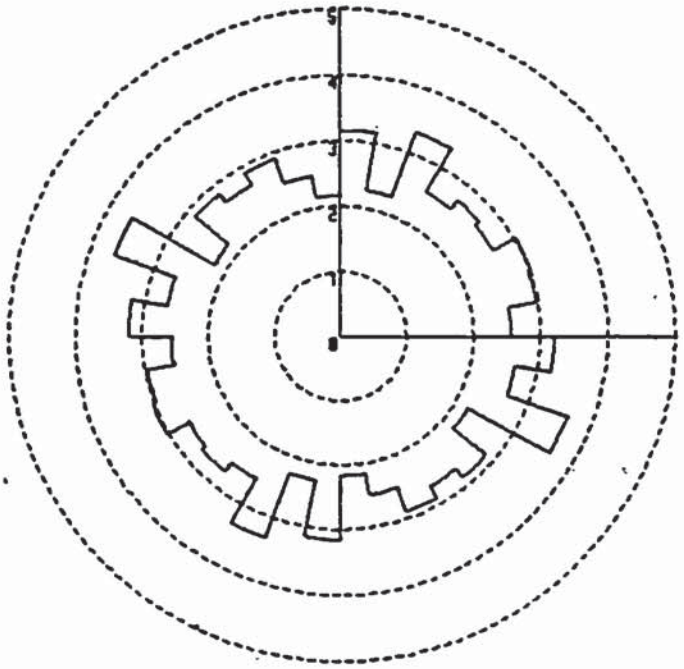

Weighted contact normal vectors

Fig 6.16 Distribution of contact normal vectors and contact normal vectors weighted to the normal force for graded assembly in quasi-equilibrium.

Fig 6.17 Distribution of contact normal vectors and contact normal vectors weighted to the normal force for 1000 disc assembly in quasi-equilibrium, Barnes (1985).

normal vectors and contact normal vectors weighted to the normal force for the uniform, graded and 1000 disc assemblies. All these figures give a fair approximation to a circular distribution indicating no significant structural anisotropy. The most notable difference between the figures is that the distribution for the uniform assembly is less smooth, which is an indication that certain force orientations are preferred. This is a result of the linear force chains with sudden direction changes exhibited in fig 6.12. The distribution of contact force obliquities for the uniform, graded and 1000 disc assemblies are illustrated in figs 6.18-6.20. These figures indicate how the structure of the assembly has altered since adding friction. Sliding contacts are indicated in the histograms by values at ±1 and in the scatter diagram by points occurring at the maximum obliquity. These figures show that for all assemblies hardly any contacts are sliding, but greater force obliquities occur within the uniform assembly.

It had been noted that, once the uniform and graded assemblies had achieved the desired mean stress and were cycled until their out of balance to contact force ratios were less than 10% after which friction was added and figs 6.18-6.19 were produced, the graded assembly was closer to quasi-equilibrium. This was demonstrated by a more uniform velocity distribution and a lower out of balance to contact force ratio. Thus the wider distribution of force obliquities could be due to the uniform assembly not being in as stable a configuration as the graded assembly when friction was added. The distribution of force obliquities from the 1000 disc test in fig 6.20 illustrate more force obliquities than the graded assembly, fig 6.19. This would indicate that

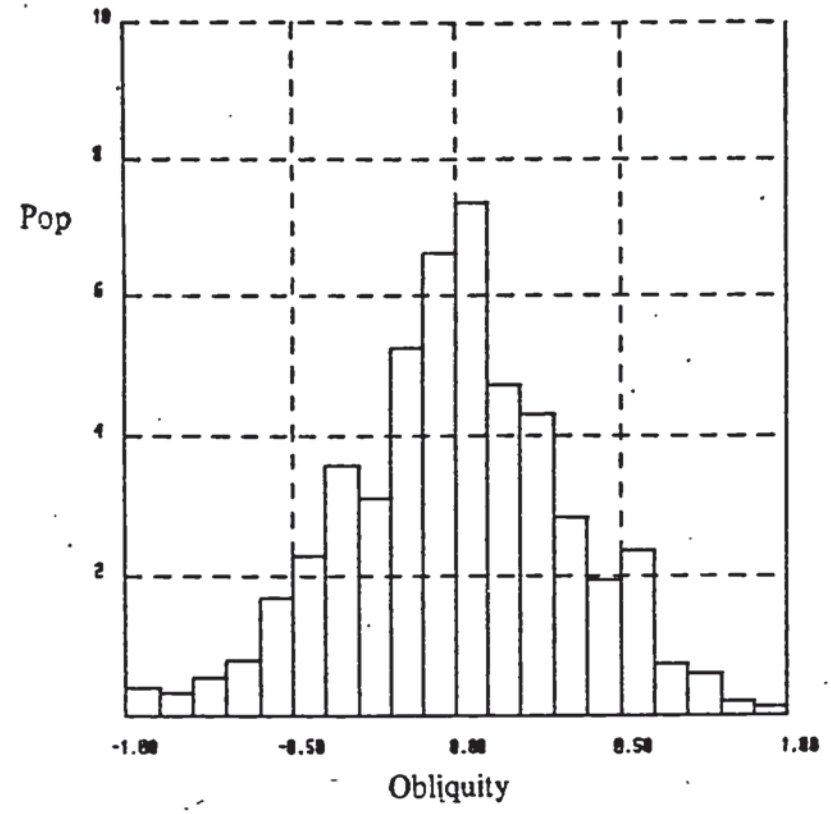

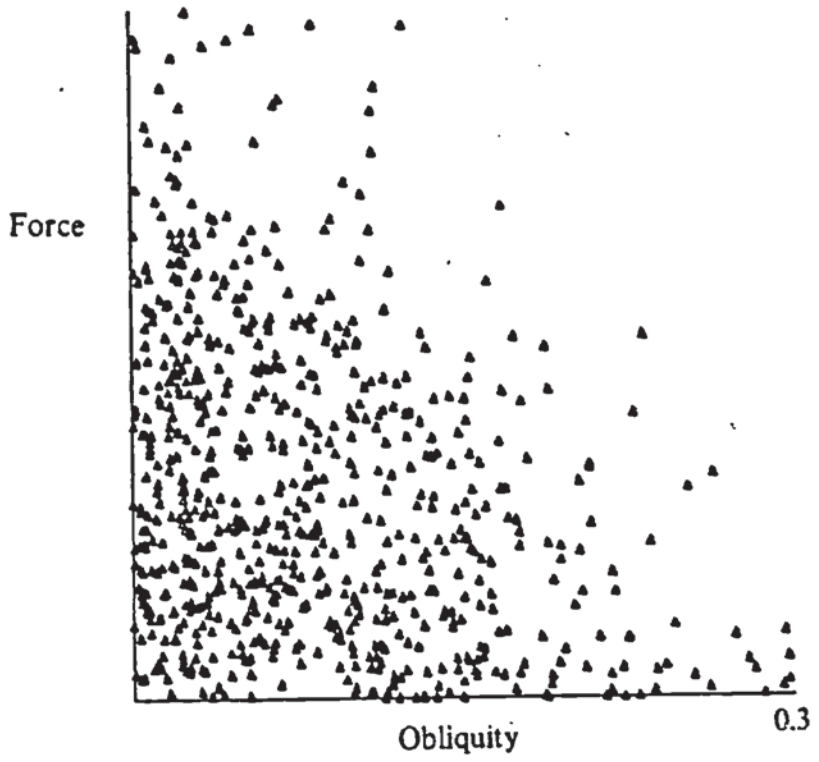

Fig 6.18 Distribution of contact force obliquities for uniform assembly in quasi-equilibrium.

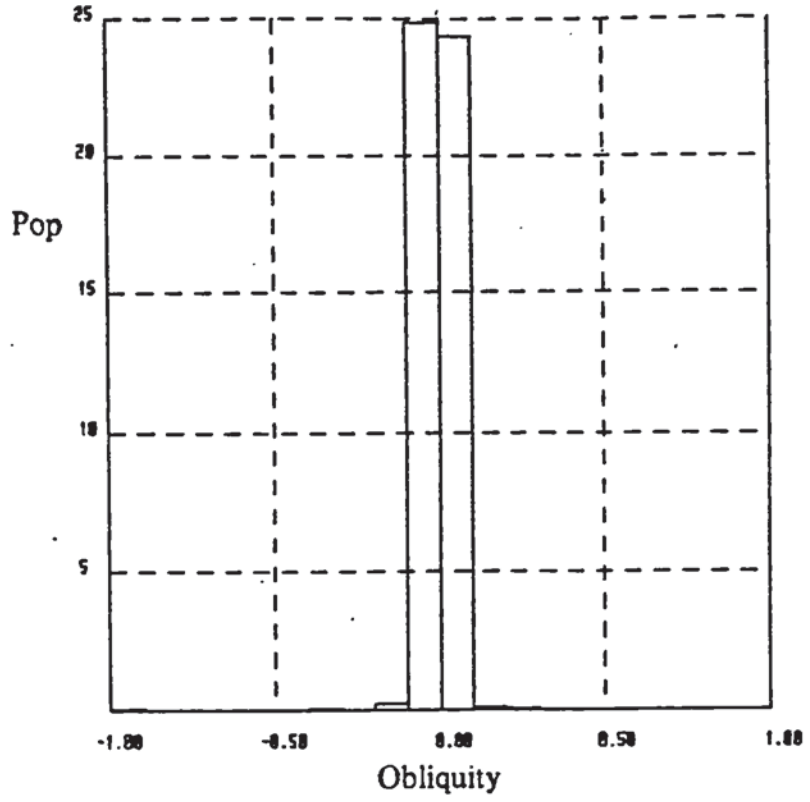

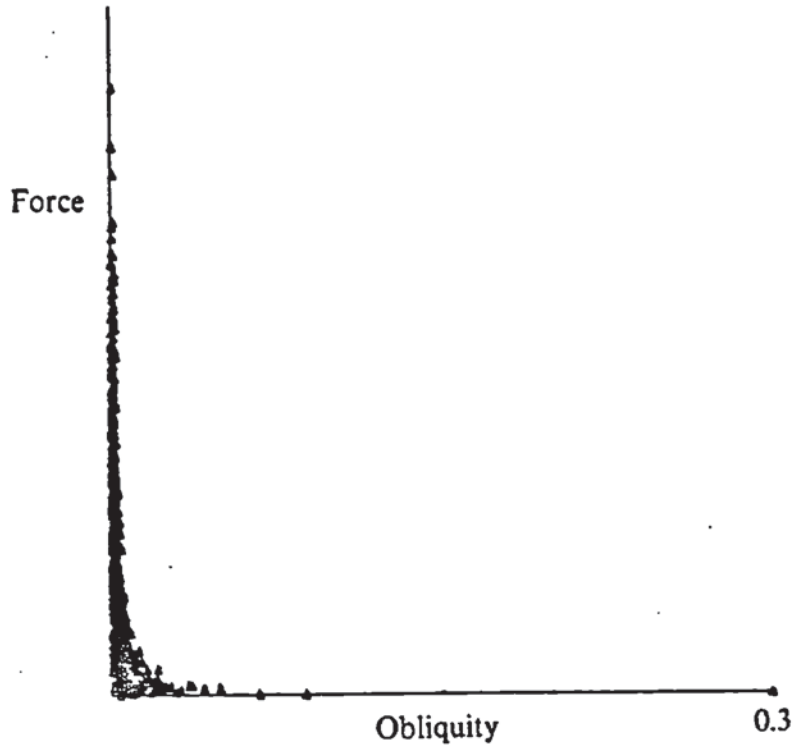

Fig 6.19 Distribution of contact force obliquities for graded assembly in quasi-equilibrium.

Fig 6.20 Distribution of contact force obliquities for 1000 disc assembly in quasi-equilibrium, Barnes (1985).

the graded assembly was closer to quasi-equilibrium when friction was added and the system cycled. This may be due to the greater number of cycles used to allow the graded assembly to reach quasi-equilibrium than used by Barnes (1985) in the 1000 disc test.

6.5 Quasi-static shear deformation.

6.5.1 Preliminary tests.

Once the desired mean stress had been achieved for both the uniform and graded assemblies by the use of the continuum tensor to overcome assembly instabilities, it appeared logical that the same control technique would be necessary for the simulation of the shear deformation stage. However, this was not the case.

Using equal boundary strain rate and continuum strain rate tensors both the uniform and graded assemblies were subjected to constant volume shear deformation. However, in both simulations instabilities occurred, similar to those experienced during the unsuccessful attempts at isotropic compression. A simulation was performed using the uniform assembly and 10% of the time step based on the Rayleigh wave speed. This managed to suppress the build up of unrealistically high dynamic inter-particle forces but did not prevent large particle velocities occurring. Reducing the strain rate merely delayed the seemingly inevitable development of high velocities within the assembly. The particle interactions were effectively transient dynamic collisions similar to interactions in rapid flow simulations but 'trapped' within the constrained boundary. Consequently it was not possible to generate a significant deviator stress, as indicated by the evolution of sin Φ given in fig 6.21,

whereas the isotropic stress increased by an order of magnitude due to the dynamic inter-particle forces.

When using the continuum tensor the velocity of each particle consists of two parts: a fixed velocity component dependant on the value of the imposed strain rate tensor, and a perturbation velocity resulting from out of balance forces acting on the particle generated from particle interactions. The perturbation velocities accumulated over successive time steps to such an extent that they became orders of magnitude larger than the imposed fixed velocities. It was decided that numerical instability had occurred and that it was necessary to re-introduce mass proportional damping, developed by Cundall (1971), into the velocity algorithms in subroutine MOTION. This would have the effect of suppressing the development of the perturbation velocities.

Mass proportional damping is controlled by the parameter CON1 employed in subroutine MOTION. When CON1 equals 1.0 then no damping is applied. For a CON1 value of 0.0 then the perturbation velocities are completely damped out and the particle moves under the influence of the fixed imposed velocity only. A series of tests were performed to appraise the effect of mass proportional damping on the shear behaviour of the assembly. It was found that when CON1 was less than 0.5 the out of balance force tended to be between 50-75% of the contact force. For CON1 values between 0.2 and 0.8 the ratio of the perturbation velocities to the fixed imposed velocities reduced from just under 20% at 0.5% applied deviator strain to just over 5% at 2% strain. Higher values of CON1 allowed the perturbation velocities to accumulate such that they were continually greater than the

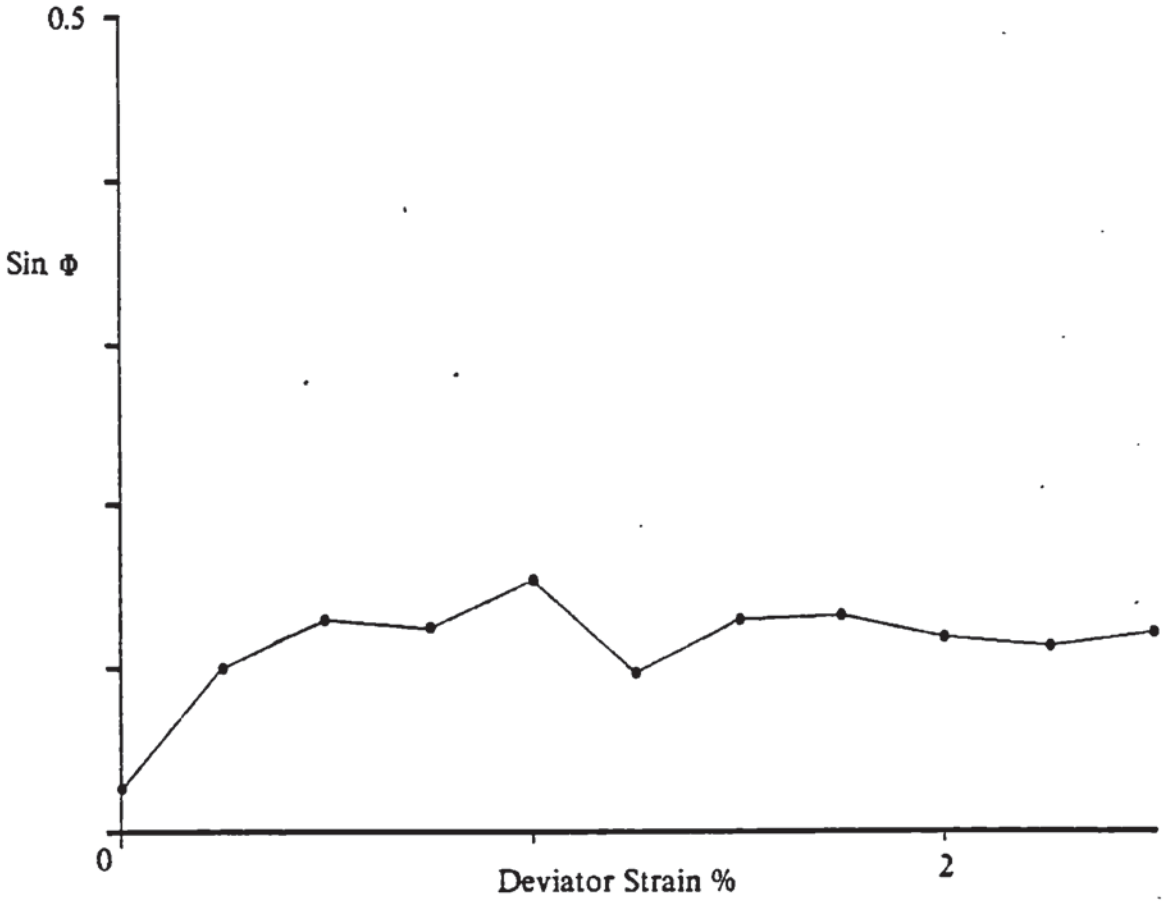

Fig 6.21 Evolution of sin Φ for constant volume test, uniform assembly, no mass proportional damping, FRAC=0.1.

fixed velocities imposed by the continuum strain rate tensor. The effect of the parameter CON1 on the evolution of sin Φ and the isotropic stress is illustrated in fig 6.22 for values of CON1 equal to 0.99 and 0.8. The most significant effect of varying CON1 was on the isotropic stress evolution. The sensitivity of the isotropic stress to the amount of mass proportional damping used is clearly seen from the rapid increase in isotropic stress obtained for CON1 equal to 0.25, also shown in fig 6.22. From fig 6.22 and the comments above it is clear that a satisfactory simulation had not been possible. The out of balance to contact force ratios obtained were too high for the assemblies to be considered in quasi-equilibrium. In an attempt to overcome this lower strain rates were applied.

Thornton and Barnes (1986b) report results from a constant volume shear test on a dense assembly of discs in which it was observed that there was no significant decrease in isotropic stress at the start of the shear stage. Since the areal porosity of the uniform, graded and dense assemblies were comparable, and excessive damping was not desirable, it was decided that a value of CON1 equal to 0.75 would be used for the slow strain rate test. Figure 6.23 illustrates this test which used a strain rate of 1% deviator strain applied over one million calculation cycles. Even with such a slow strain rate the test could not be considered to be in quasi-equilibrium as the out of balance to contact force ratio rapidly reached approximately 60% at 0.1% applied strain, which was then maintained around that level.

As a result of the extensive investigation reported in this section it was concluded that, although the continuum strain rate tensor in conjunction with the boundary strain rate

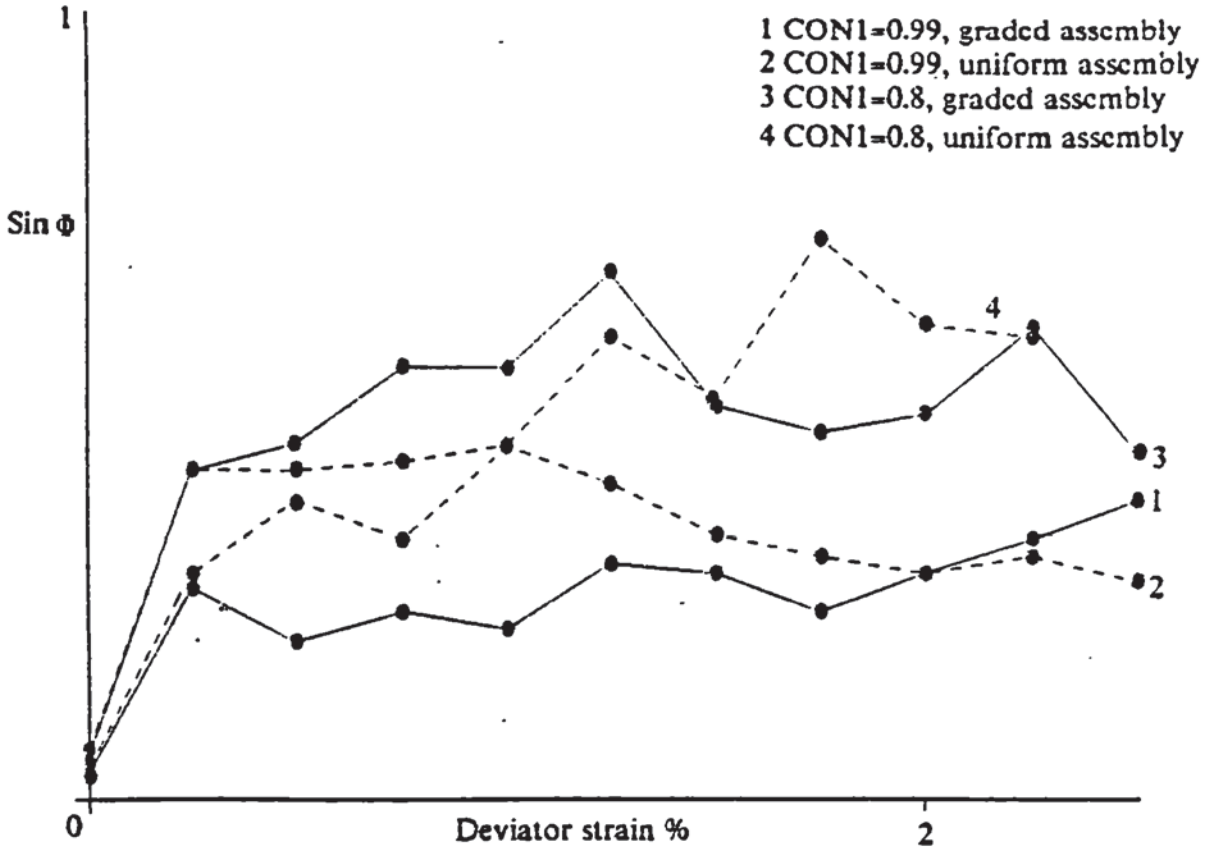

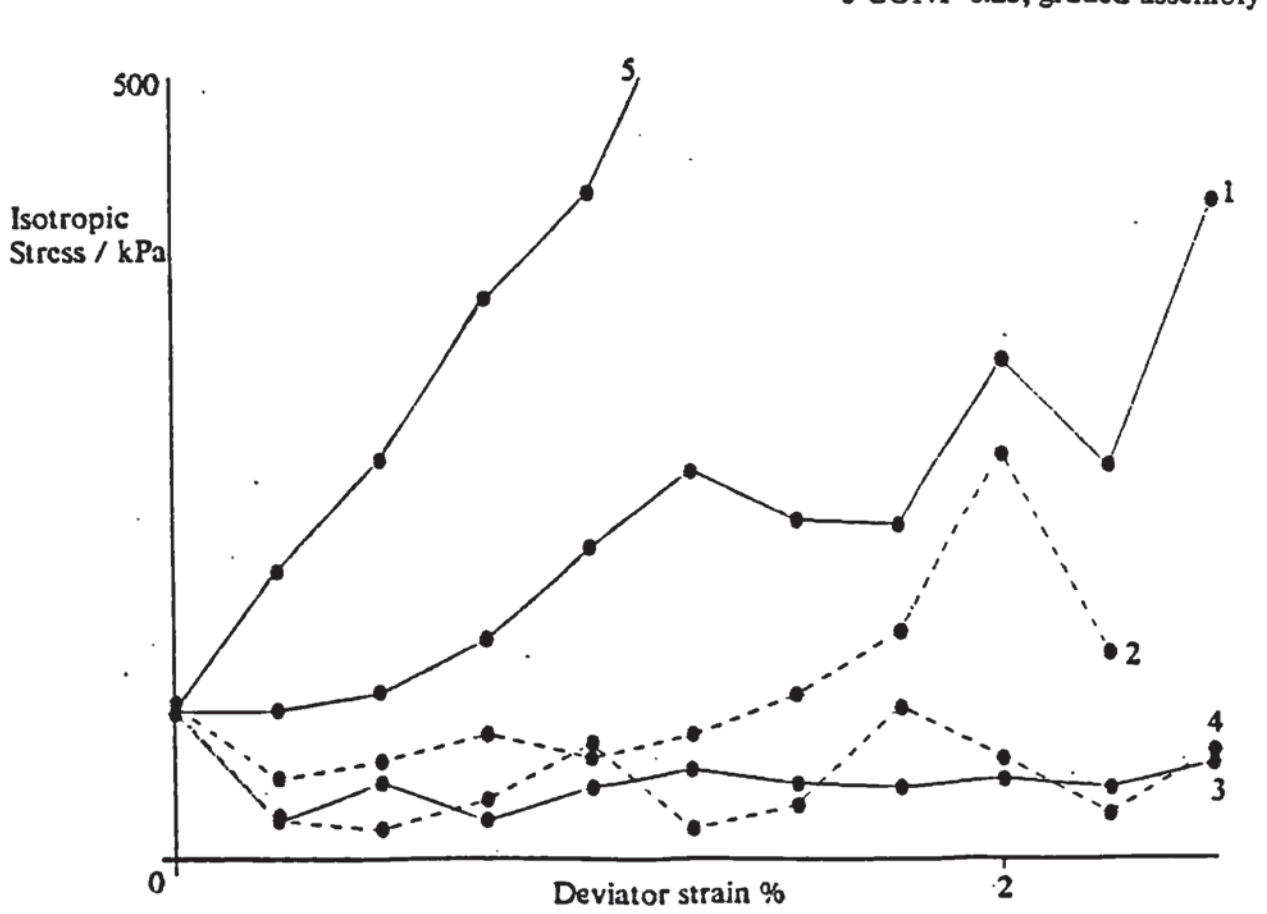

Fig 6.22 Constant volume tests, effect of mass proportional damping.

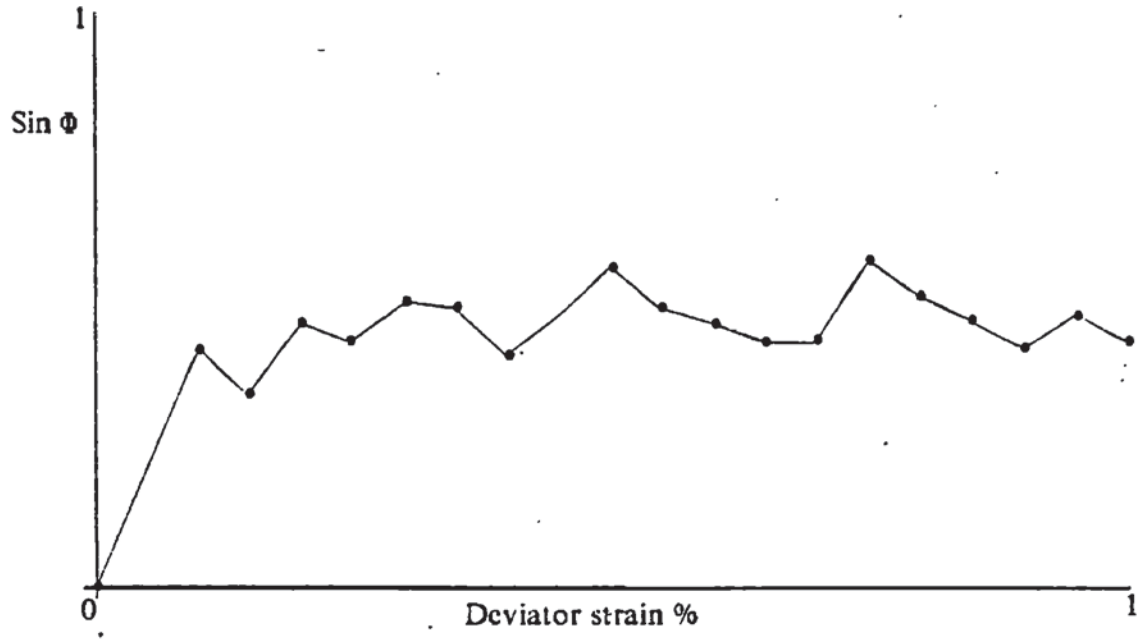

a) evolution of sin Φ

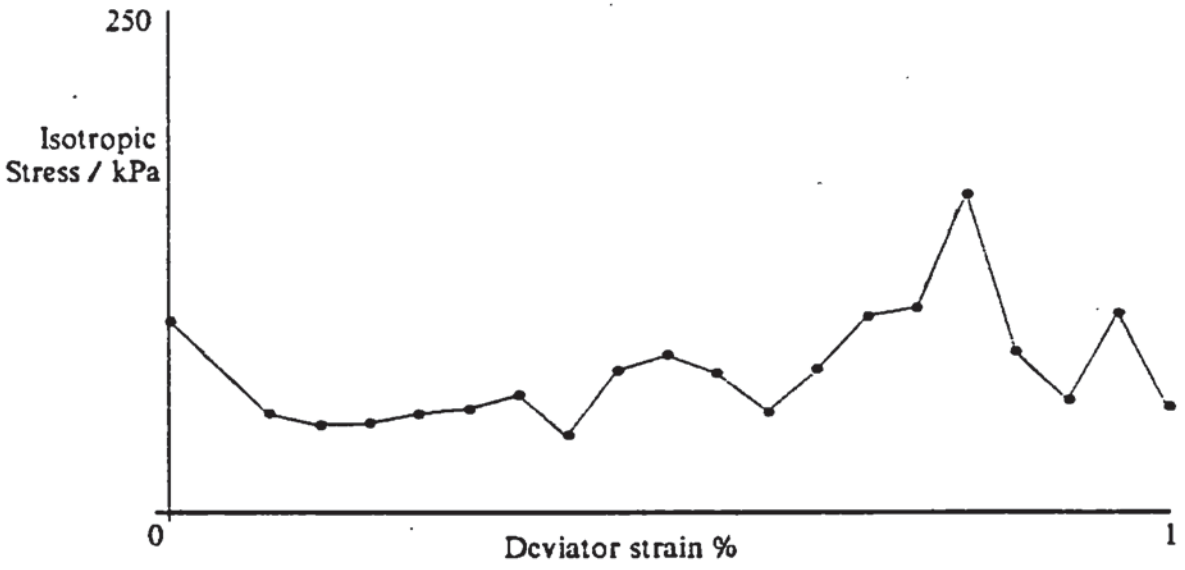

b) evolution of isotropic stress

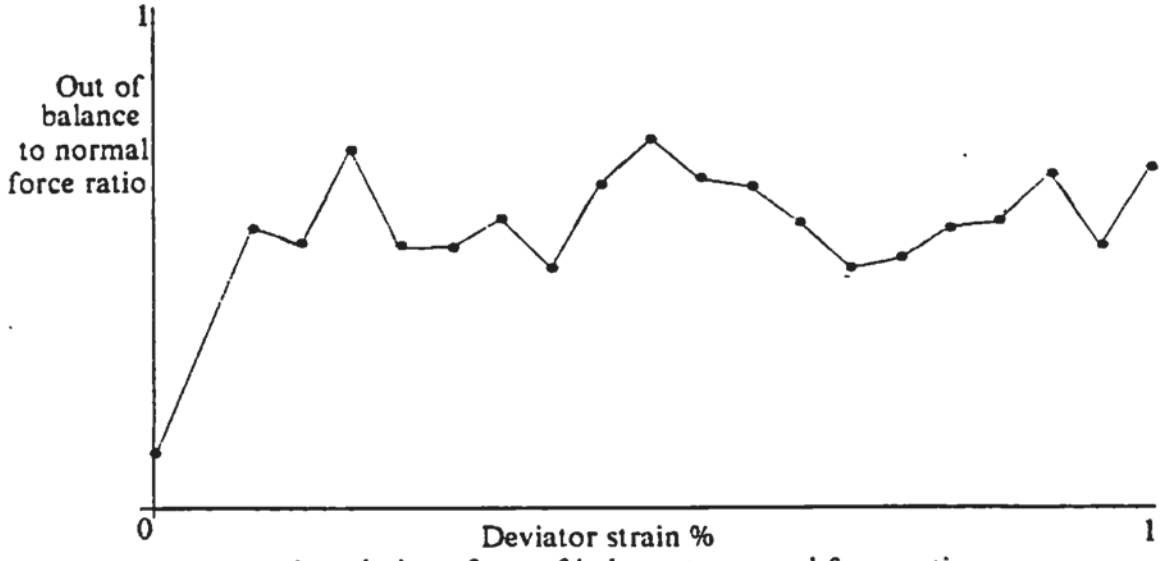

c) evolution of out of balance to normal force ratio

Fig 6.23 Constant volume test, applied strain rate of 1E-5 m/s
CON1=0.75, graded assembly.

tensor could be used to successfully compress an assembly to a desired mean stress, this combination cannot be used for simulations of shear deformation. This is due to the constrained boundary being unable to accommodate the additional perturbation velocities which result from particle interactions.

Cundall (1988) reports the use of a continuum strain rate tensor used in the control of shear deformation in his three dimensional version of BALL. However, periodic boundaries are employed which do not create the absolute fixed constraint that occurs due to the boundary control used for circular two dimensional particle systems in program BALL.

The following section presents two constant volume shear tests in which quasi-equilibrium conditions were successfully maintained by using a strain controlled boundary only.

6.5.2 Quasi-static shear deformation of uniform and graded assemblies.

Both constant volume shear tests were performed using a boundary strain control which applied 1% deviator strain in two million cycles, 10% of the time step based on the Rayleigh wave speed, 10% contact damping and a value for inter-particle friction of 0.3. A CON1 value of 0.99 was adopted, a value which was shown to have little effect on the isotropic stress, section 6.5.1. The average porosity of the graded and uniform assemblies was 14% and 16% respectively. Throughout the tests the assemblies were close to equilibrium since the out of balance to contact force ratios were always less than 0.5%.

The evolution of sin Φ and the isotropic stress for both

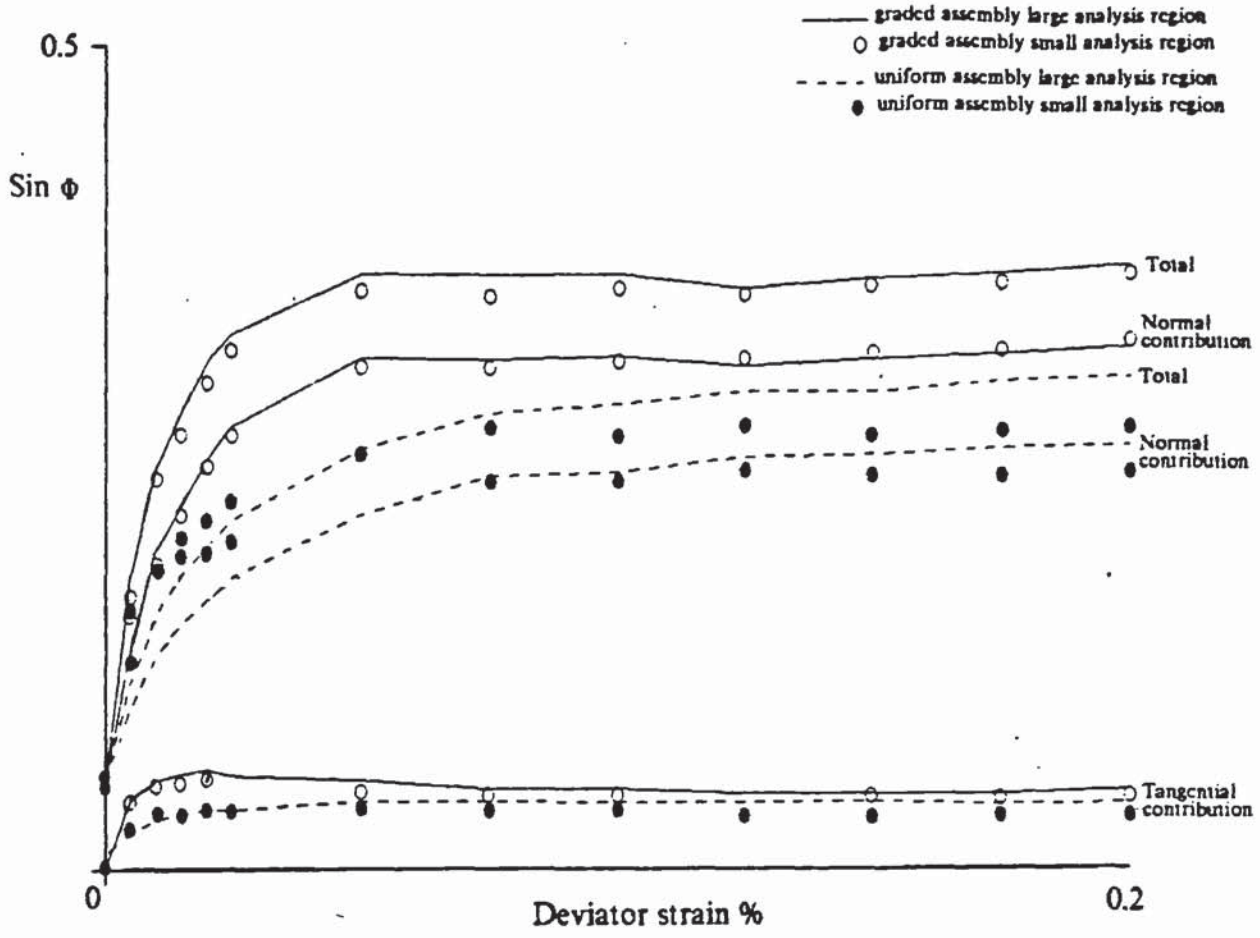

Fig 6.24 Evolution of sin Φ for constant volume test, applied strain rate of 5E-6m/s, CON1=0.99

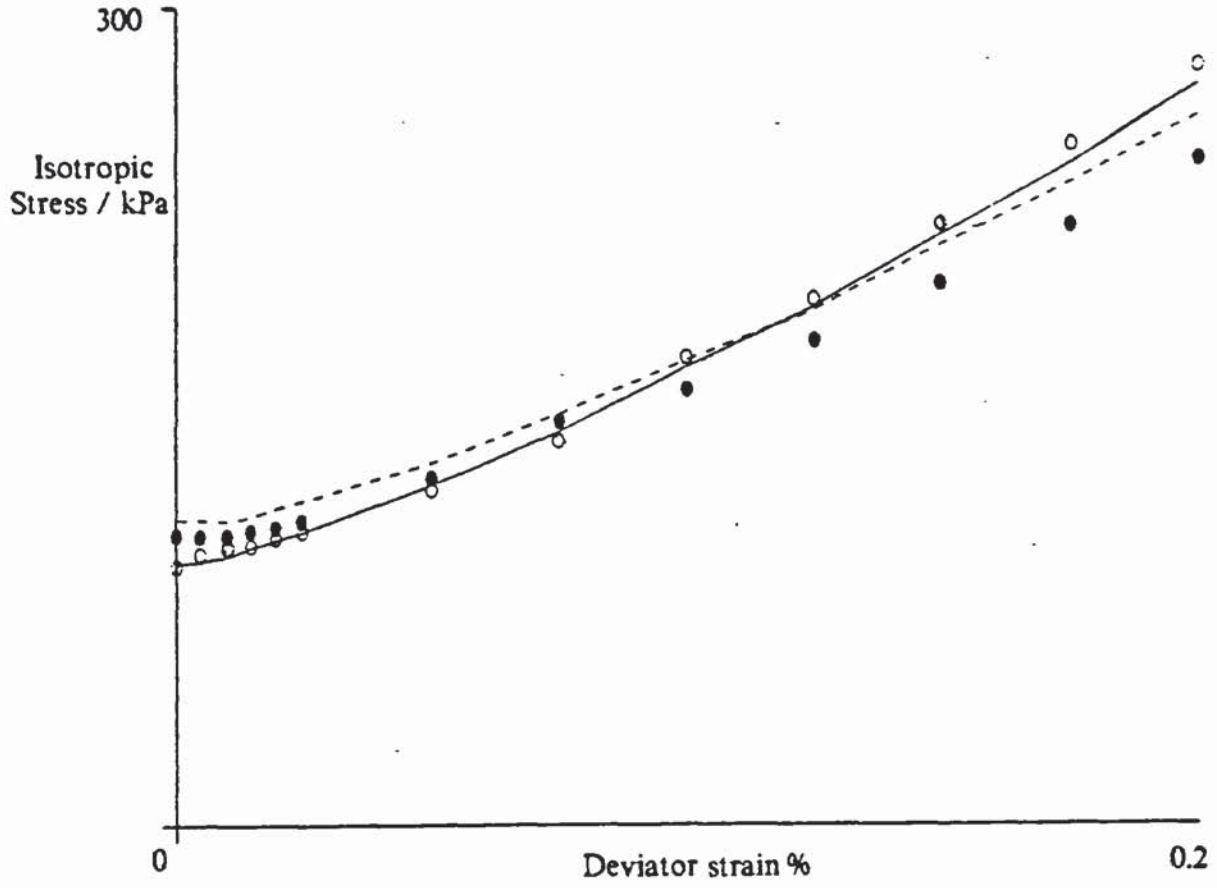

Fig 6.25 Evolution of isotropic stress for constant volume test, applied strain rate of 5E-6m/s, CON1=0.99

tests are illustrated in figs 6.24-6.25. Two analysis regions were used which represent 87 and 64% of the graded assembly and 70 and 40% of the uniform assembly. For the graded assembly both analysis regions can be seen to give excellent agreement with one another indicating a homogeneous response within the assembly. Results from the uniform assembly give slightly more scatter but still give good agreement. This slight scatter is due to the smaller analysis regions used. The sin Φ curves in fig 6.24 show the graded assembly to be extremely stiff, the system having reached its maximum sin Φ value of around 0.36 by 0.05% deviator strain. The uniform assembly is not quite so stiff and reaches its maximum sin Φ value of approximately 0.3 just after 0.1% deviator strain.

The tangential force contribution to the deviator stress can be seen to be small, in the order of 14% for the graded and 15% for the uniform assembly. This can be compared to the sin Φ evolution from the 1000 disc test of Barnes (1985), fig 6.26, which reached approximately 0.46 at 3% deviator strain and still appeared to be increasing slightly. Also a higher tangential force contribution to the deviator stress was obtained of around 18%. Both the uniform and graded assemblies are much stiffer than the 1000 disc assembly. This is due to the Hertzian normal contact interaction law.

The isotropic stress curves in fig 6.25 illustrate a smooth build up of isotropic stress for both the uniform and graded assemblies. The corresponding stress paths are shown in fig 6.27. The evolution of isotropic stress and the stress path is similar to the results of the constant volume test reported by Thornton and Barnes (1986b).

For both assemblies, the percentage of sliding contacts

Fig 6.26 Evolution of sin Φ for constant mean stress test on 1000 disc assembly, Barnes (1985).

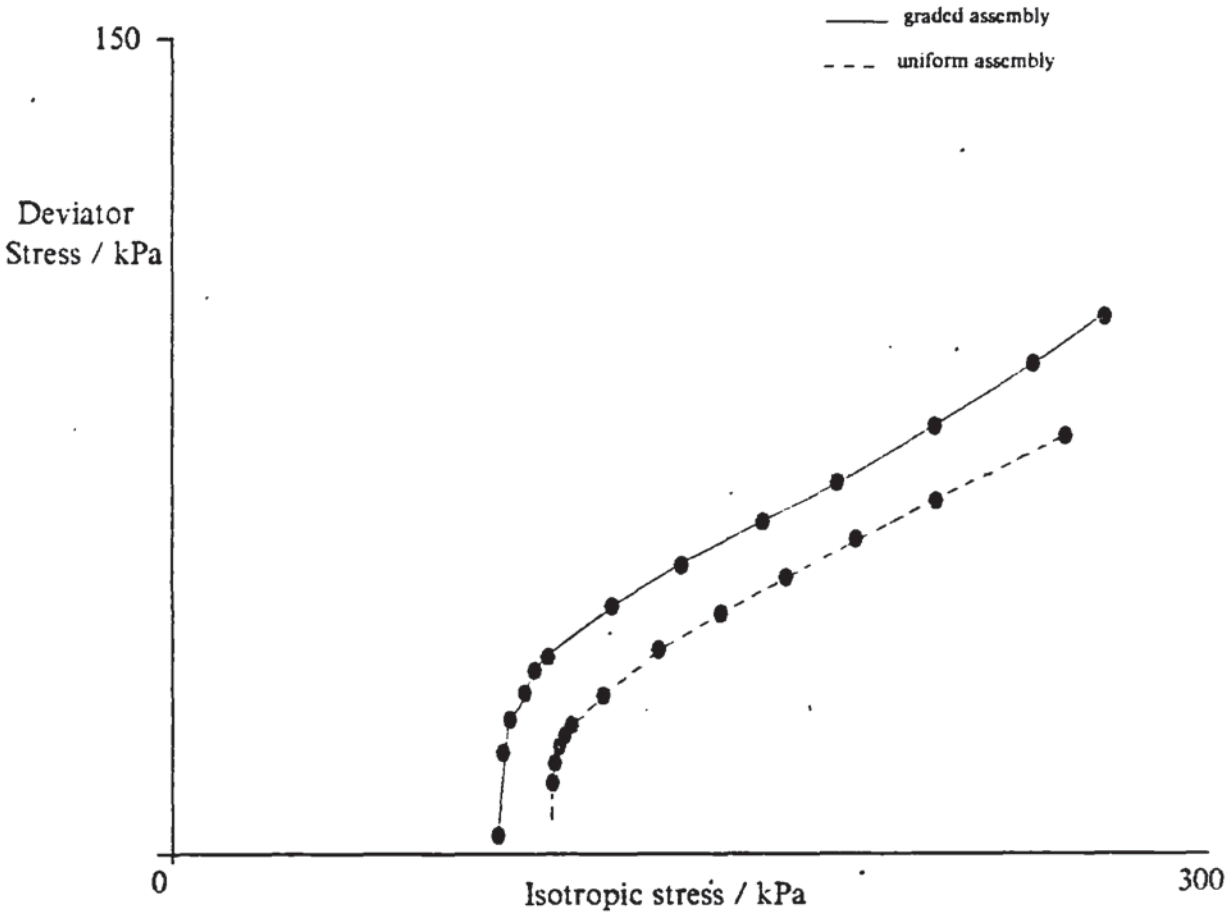

Fig 6.27 Evolution of stress paths.

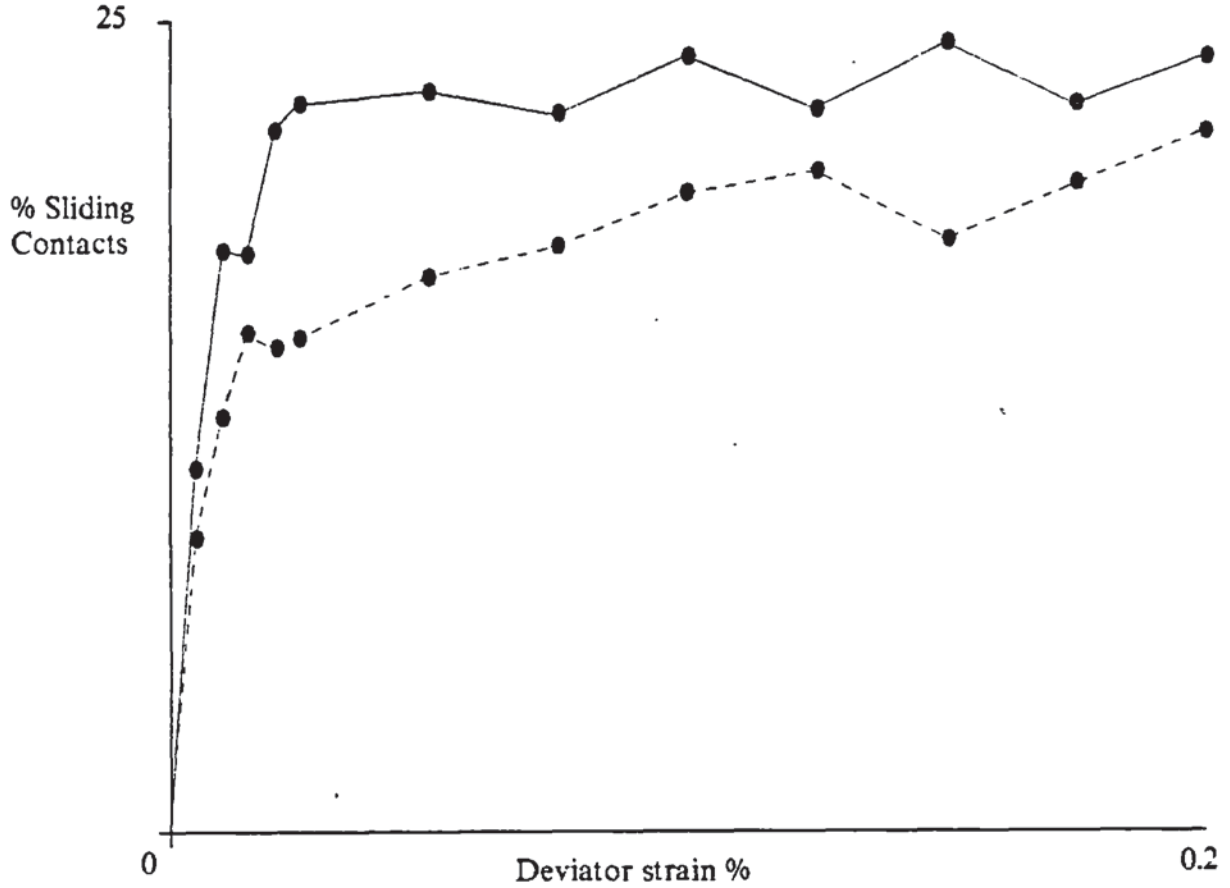

Fig 6.28 Percentage of sliding contacts.

illustrated in fig 6.28 reaches a maximum at approximately the same deviator strain as the tangential force contribution to sin Φ and, as reported by Barnes (1985) for the 1000 disc test, never more than 25% of contacts are sliding at any one time.

The degree of structural anisotropy induced may be defined by the parameter f=Φ1-Φ2, Thornton (1987a), where Φ1 and Φ2 are the principal components of the structural anisotropy tensor Φij, section 4.6. The evolution of induced structural anisotropy is shown in fig 6.29. It can be seen that, for both assemblies of spheres, the structural anisotropy increases at a relatively uniform rate until a maximum is reached at around 0.1% strain. The degree of structural anisotropy then remains essentially constant.

Barnes (1985) also observed that the structural anisotropy evolved gradually at an essentially uniform rate for the 1000 disc assembly. However, the simulation was terminated with sin Φ still slowly increasing. Comparing figs 6.24 and 6.29 it can be seen that the degree of structural anisotropy reaches its maximum value once the maximum sin Φ value has been attained. For the 1000 disc assembly, Barnes (1985) obtained a maximum degree of anisotropy of around 0.15. The difference between this value and the two sphere assemblies may be attributed to the non-linear Hertzian contact interaction law.

Barnes (1985) observed a continuous decrease in the average coordination number during loading. For the graded assembly fig 6.30 shows a similar decrease in average coordination number but illustrates that once sin Φ has reached its maximum value, the average coordination number remains essentially constant. However, for the graded assembly, due

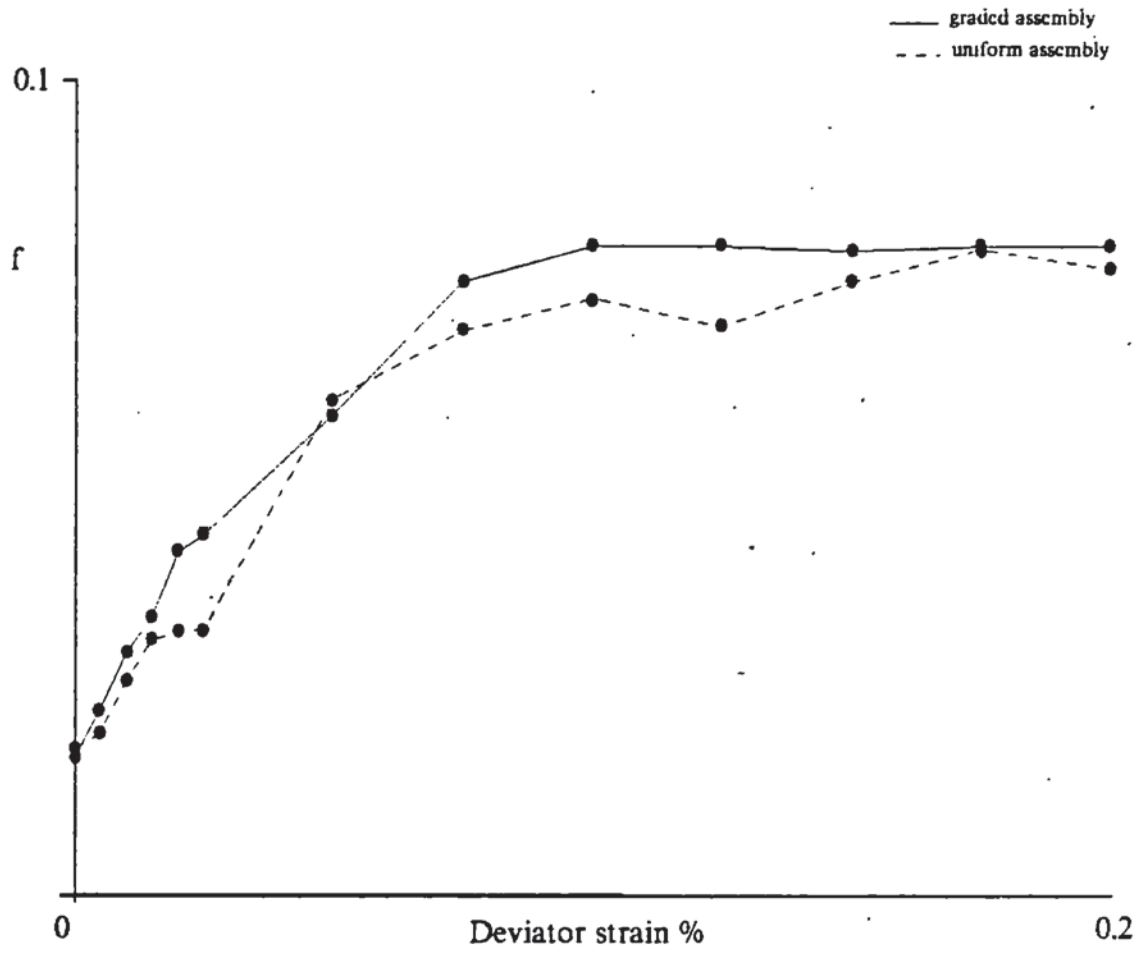

Fig 6.29 Evolution of the structural anisotropy tensor.

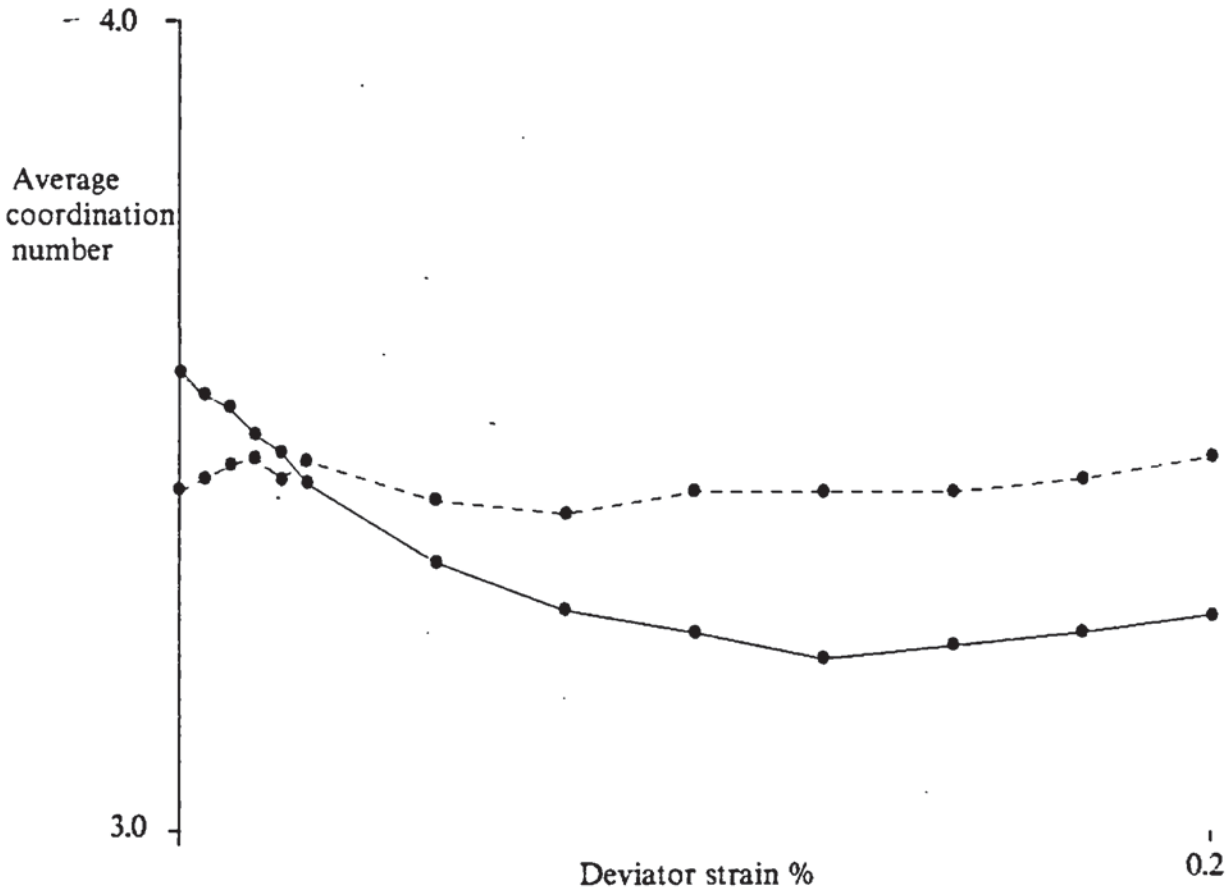

Fig 6.30 Variation in average coordination number.

to the regular packing, the number of contacts and therefore the average coordination number was little effected during the test.

The pictorial representation of the assembly at the start of the shear test was illustrated in section 6.4.3. The velocity distribution for the graded assembly is shown in fig 6.31 after 0.005% deviator strain had been applied. These velocities are extremely small, the maximum being in the order of 1E-7m/s. However, fig 6.31 gives an excellent representation of the movements of particles during shear deformation of the assembly.

The distribution of contact forces throughout the graded and uniform assemblies are shown in figs 6.32 and 6.33 for an applied deviator strain of 0.1%, when the sin Φ value was around its maximum. This can be compared with fig 6.34 which is the distribution of the contact forces for the 1000 disc test of Barnes (1985) at 3% deviator strain when the assembly was close to attaining its maximum sin Φ value. For all assemblies the major force chains can be seen to be orientated in the direction of compression.

Figure 6.35 represents the structure of the graded assembly by lines joining the centres of contacting particles for the same stage of the test as that illustrated in fig 6.32. The dashed grey lines represent contacts that have been broken, and the dark thick lines indicate new contacts that have occurred since the start of shear deformation. This clearly indicates that the majority of contacts which are broken during shear are in the direction of extension, which was also shown by the uniform assembly and 1000 disc assembly reported by Barnes (1985).

The distribution of contact normal vectors and contact

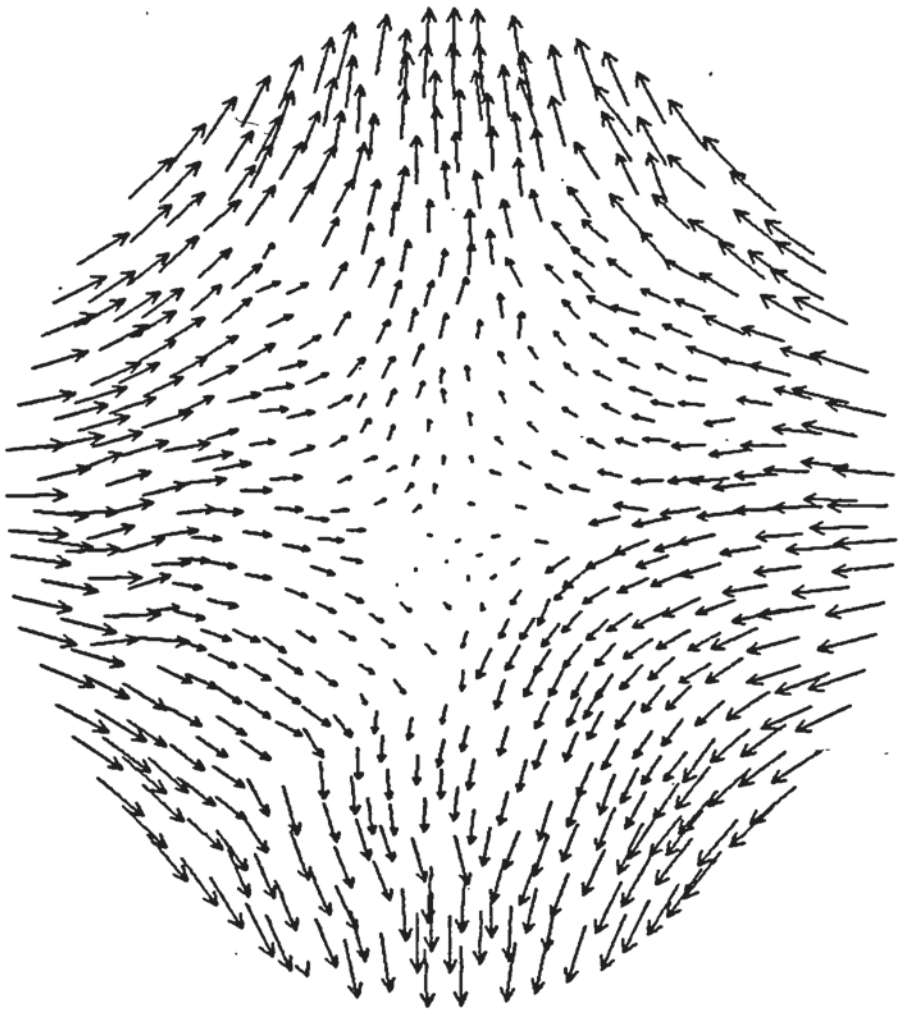

Fig 6.31 Velocity distribution within the graded assembly at 0.005% deviator strain.

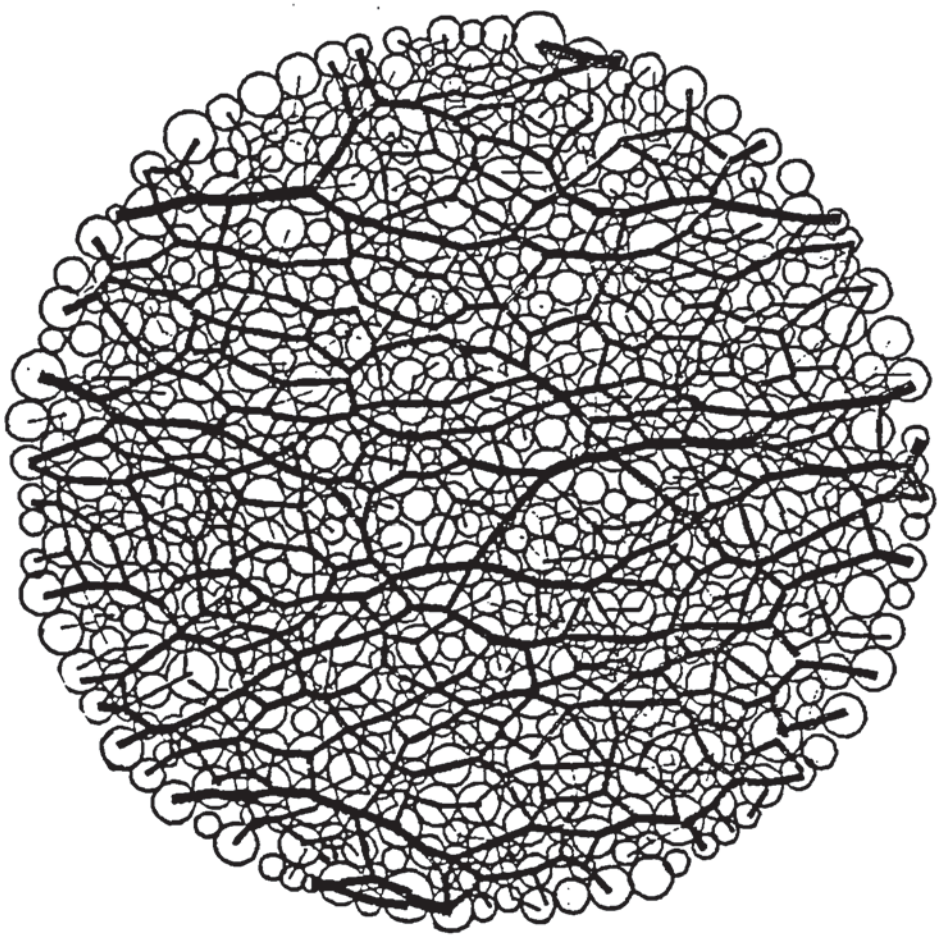

Fig 6.32 Distribution of contact forces within the graded assembly at 0.1% deviator strain.

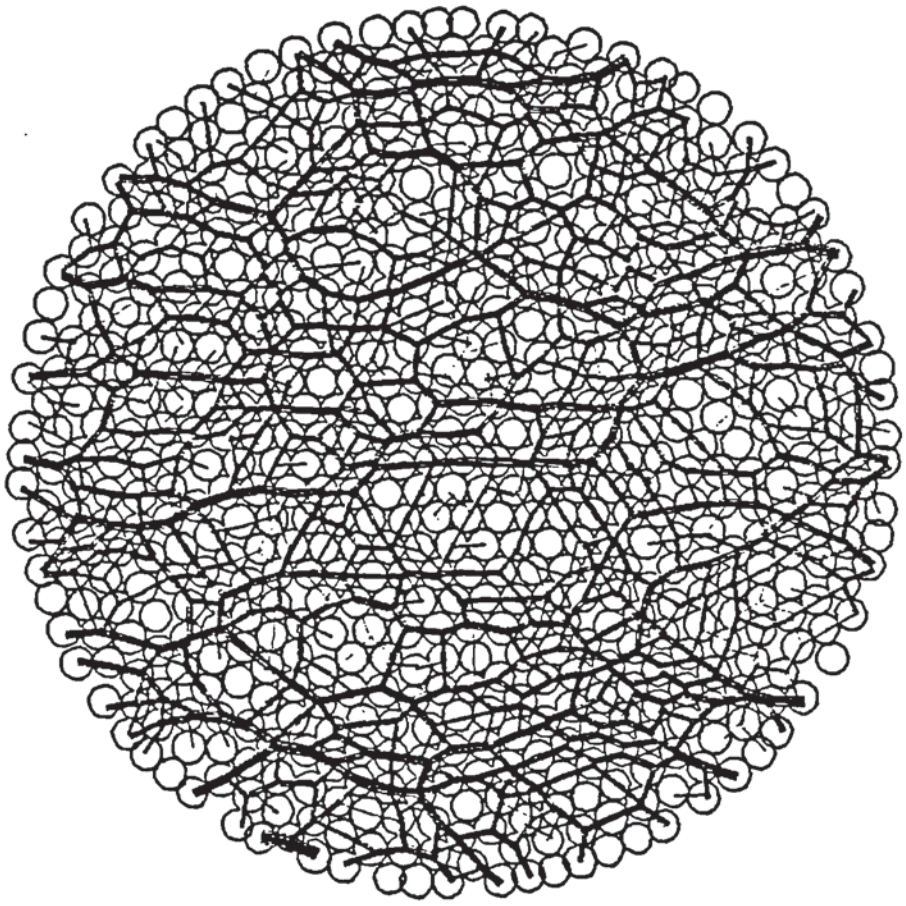

Fig 6.33 Distribution of contact forces within the uniform assembly at 0.1% deviator strain.

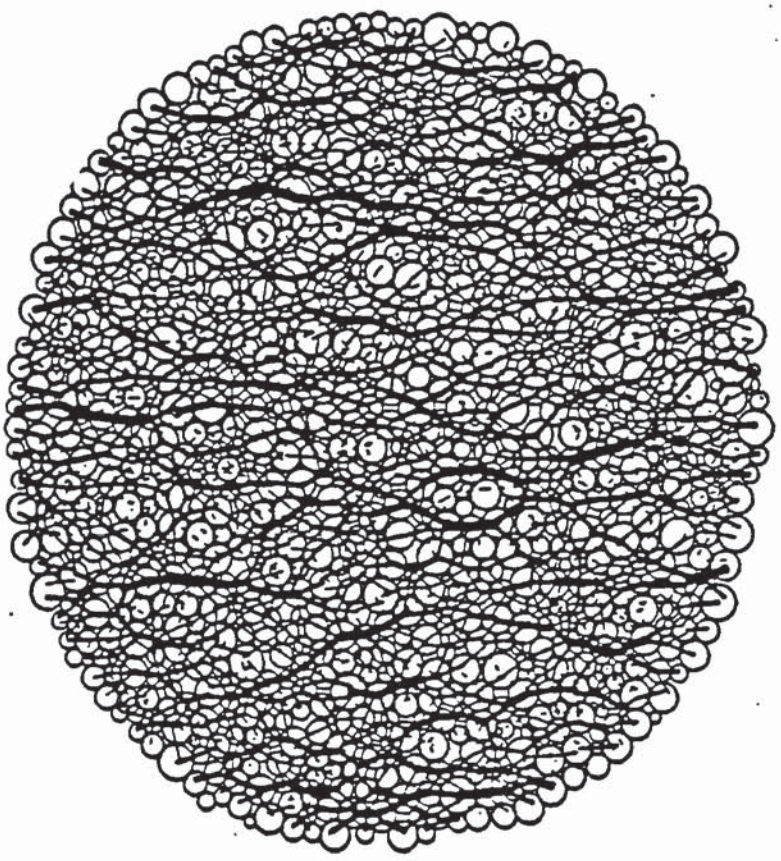

Fig 6.34 Distribution of contact forces with the 1000 disc assembly at 3% deviator strain.

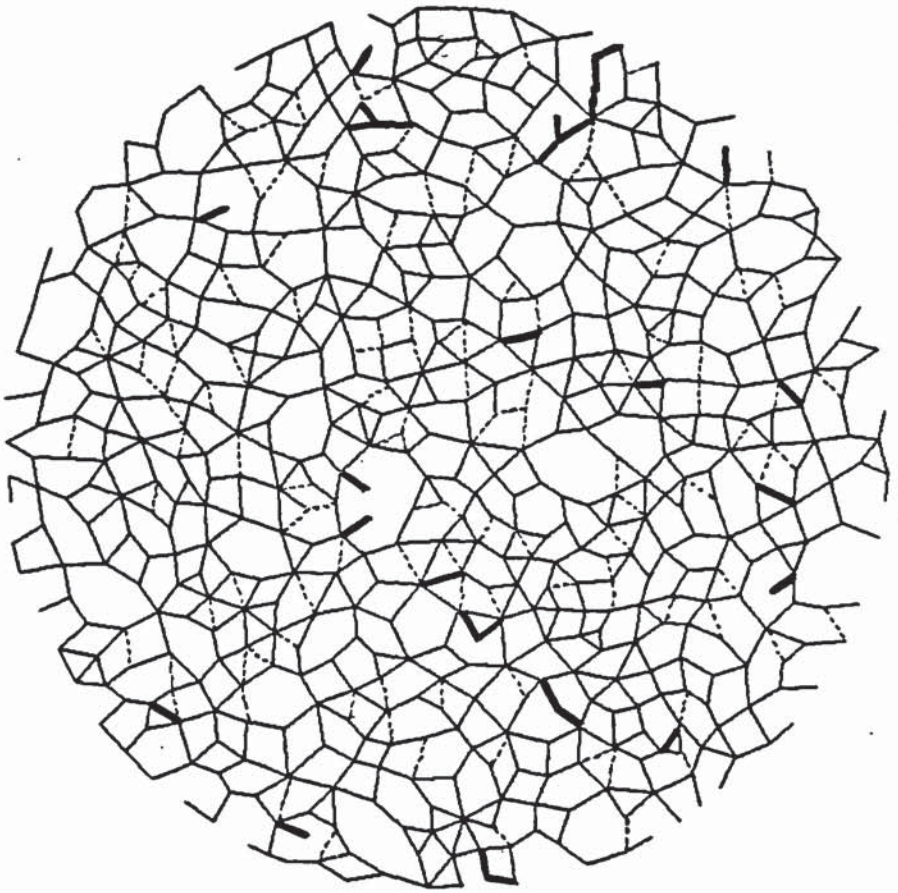

Fig 6.35 Equivalent space lattice diagram of graded assembly at 0.1% deviator strain.

normal vectors weighted to the normal force for the graded and uniform assemblies for an applied deviator strain of 0.015% are shown in fig 6.36 and 6.37. The distribution of the contact normal vectors indicate that little alteration in the structure of the assembly has occurred since the start of shear, figs 6.15 and 6.16. This observation is supported by the evolution of the structural anisotropy given in fig 6.29 which shows little change at this imposed deviator strain. However, the contact normal vectors weighted to the normal force show that the forces in the direction of extension have fallen, whilst those in the direction of compression have risen. With further increase in strain the distribution of weighted contact normal vectors becomes more pronounced in its bias toward the direction of compression.

The distribution of the contact normal vectors for sliding contacts for both assemblies are given in figs 6.38 and 6.39 for 0.005% deviator strain. The distribution indicates that most sliding contacts are oblique contacts and that few contacts are sliding in the principal direction of extension. Once the assembly has reached 0.2% deviator strain the structural anisotropy has reached a maximum and it is observed that the distribution of the contact normal vectors of the sliding contacts does illustrate significant numbers of particles sliding in the principal direction of extension, figs 6.40 and 6.41.

The distribution of mean normal contact stresses for both the uniform and graded assemblies at 0, 0.1 and 0.2% deviator strain are illustrated in figs 6.42 and 6.43. These show that at the start of shear the distribution of mean normal contact stress approximates a normal distribution.

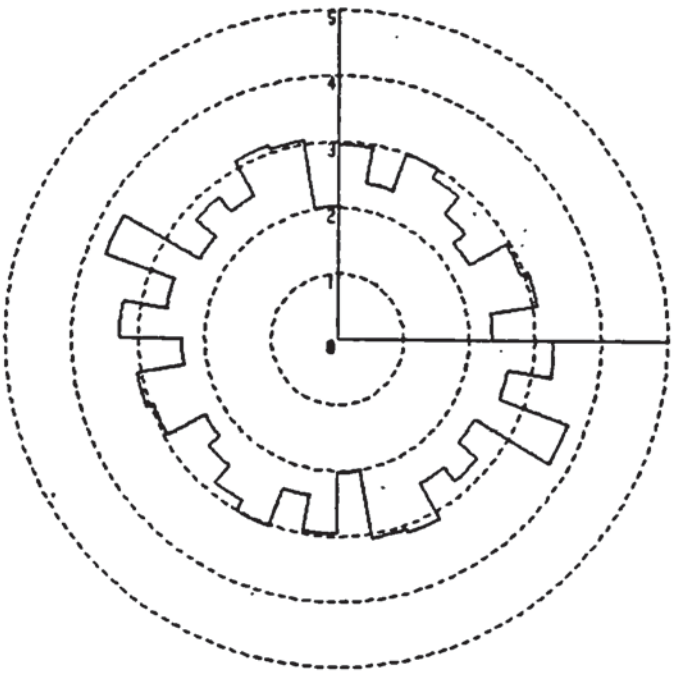

Contact normal vectors

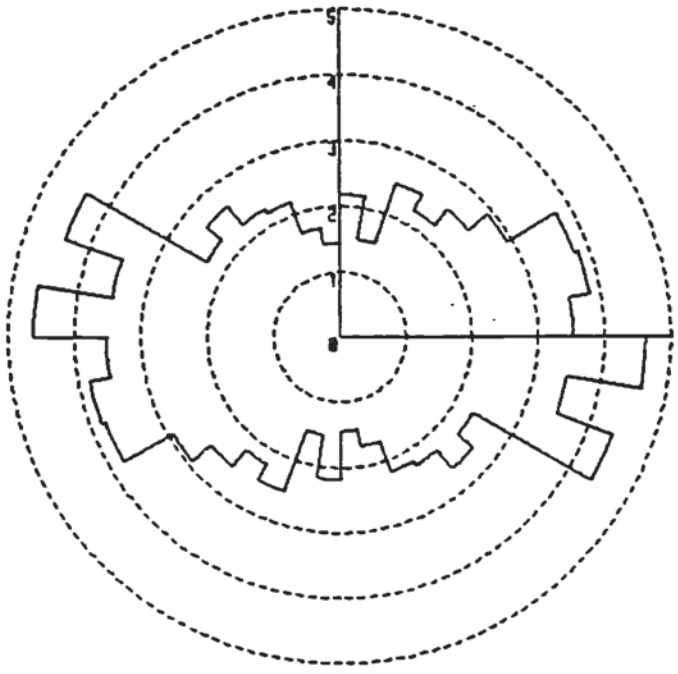

Weighted contact normal vectors

Fig 6.36 Distribution of contact normal vectors and contact normal vectors weighted to the normal force for the graded assembly at 0.015% deviator strain.

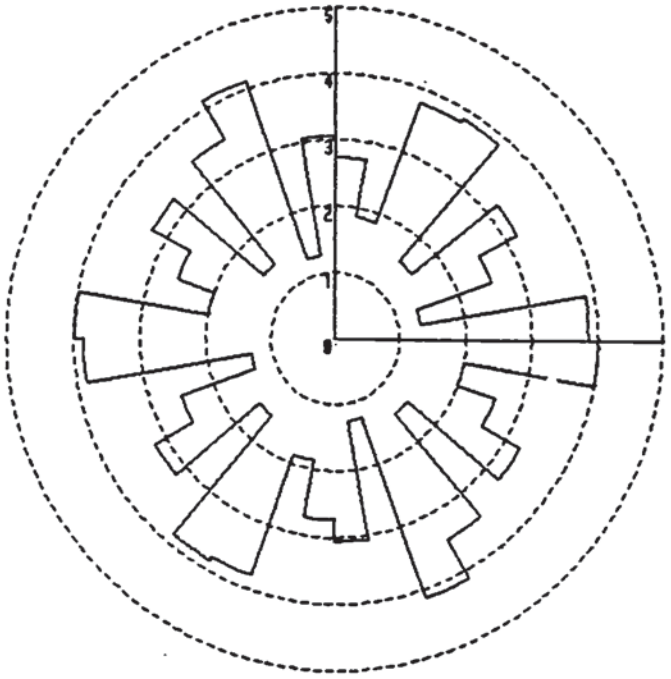

Contact normal vectors

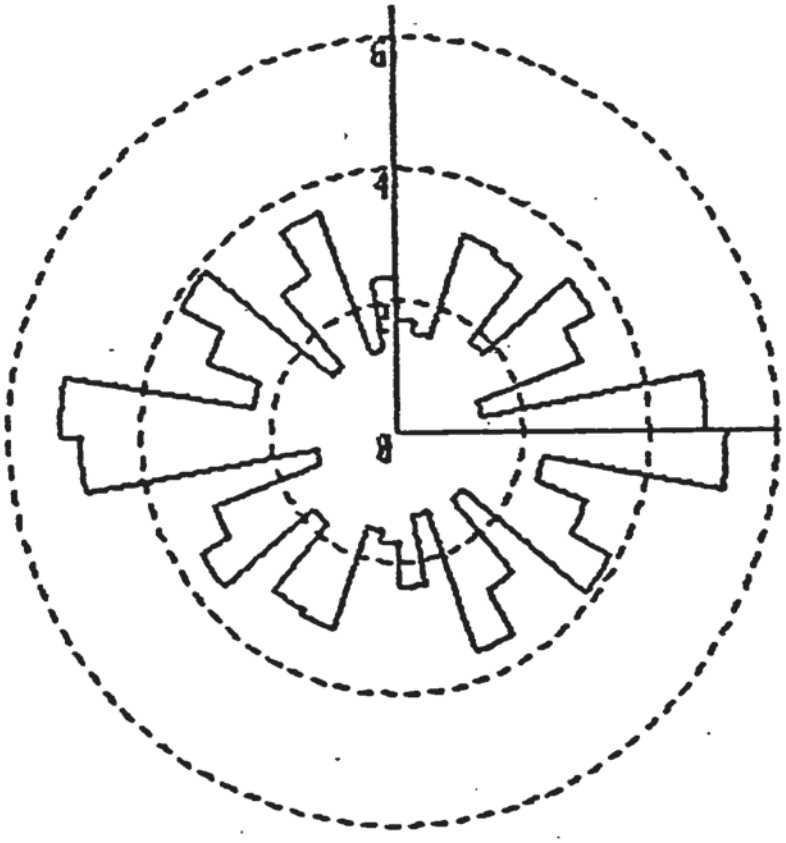

Weighted contact normal vectors

Fig 6.37 Distribution of contact normal vectors and contact normal vectors weighted to the normal force for the uniform assembly at 0.015% deviator strain.

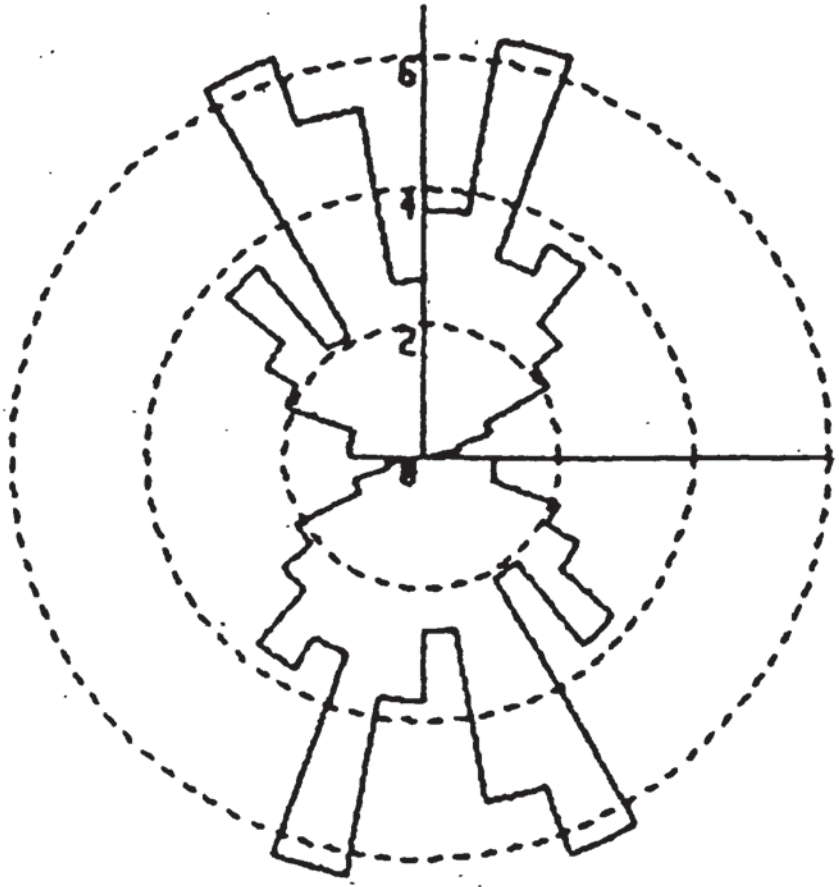

Fig 6.38 Distribution of contact normal vectors for sliding contacts for the graded assembly at 0.005% deviator strain.

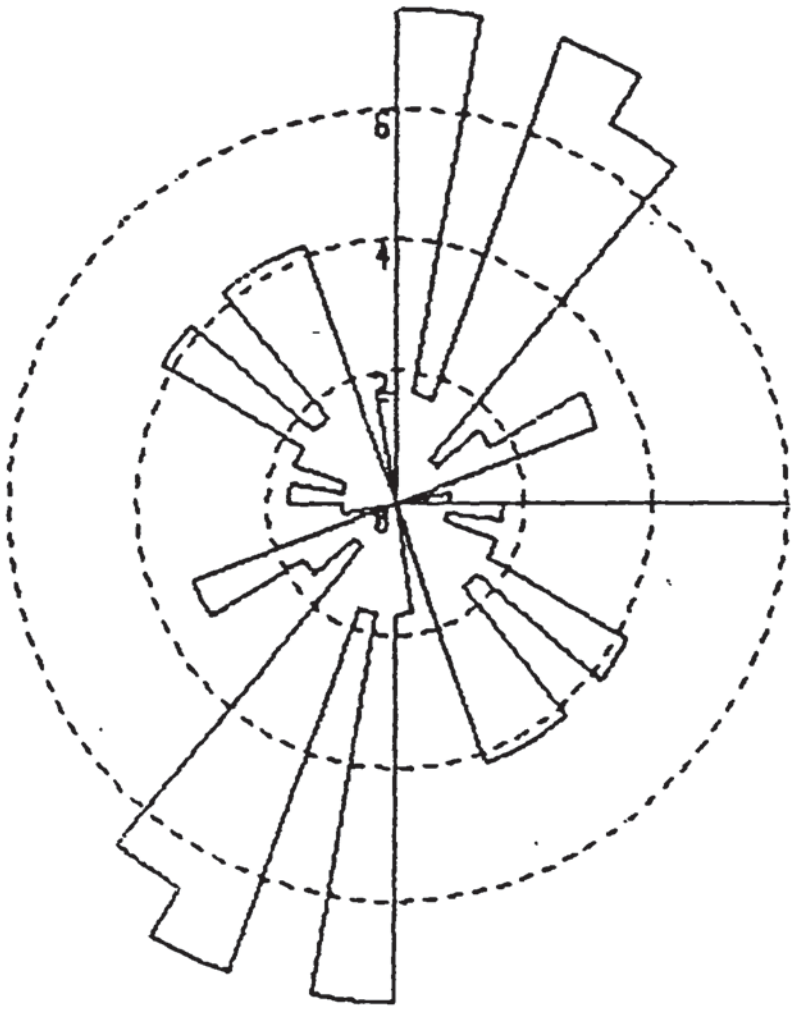

Fig 6.39 Distribution of contact normal vectors for sliding contacts for the uniform assembly at 0.005% deviator strain.

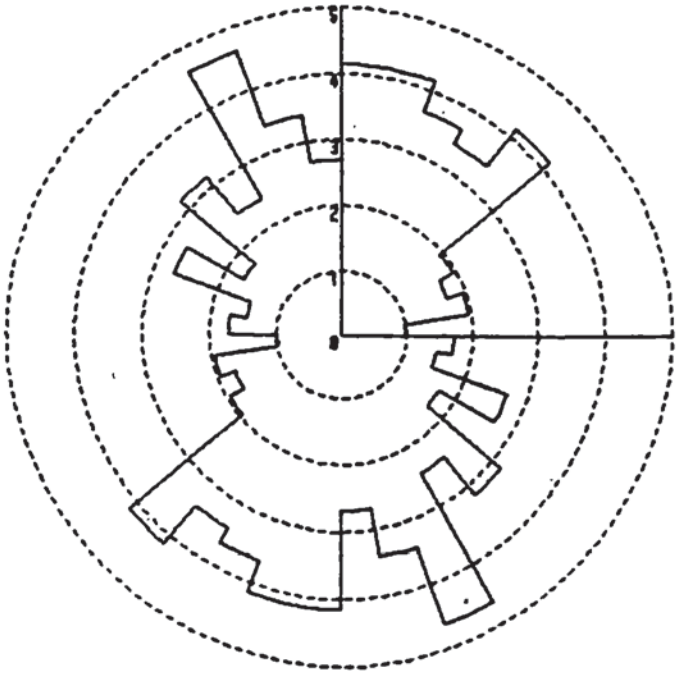

Fig 6.40 Distribution of contact normal vectors for sliding contacts for the graded assembly at 0.2% deviator strain.

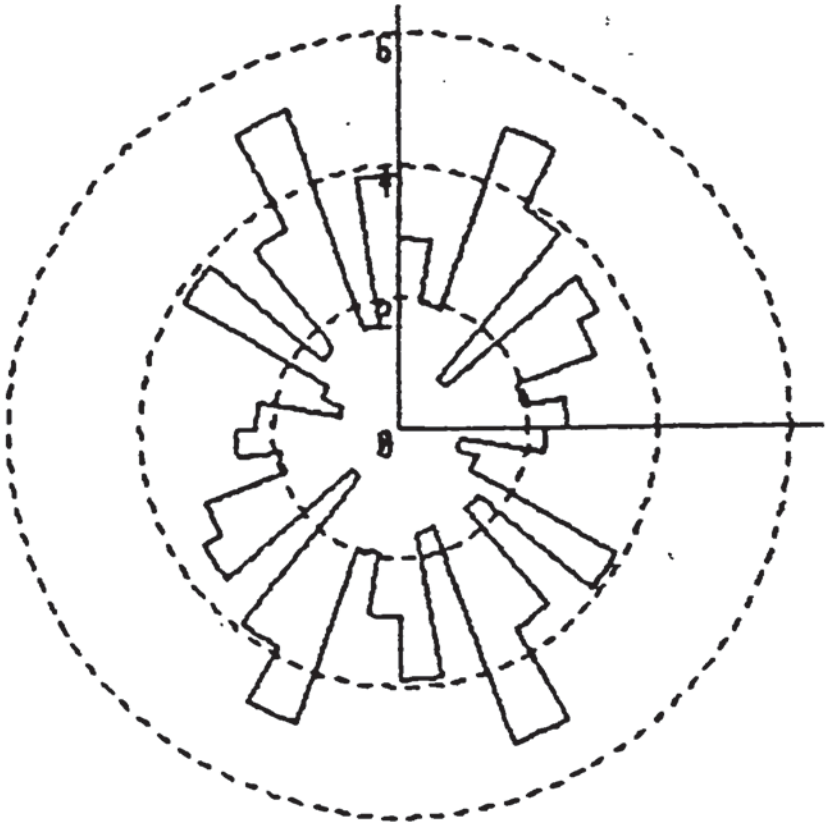

Fig 6.41 Distribution of contact normal vectors for sliding contacts for the uniform assembly at 0.2% deviator strain.

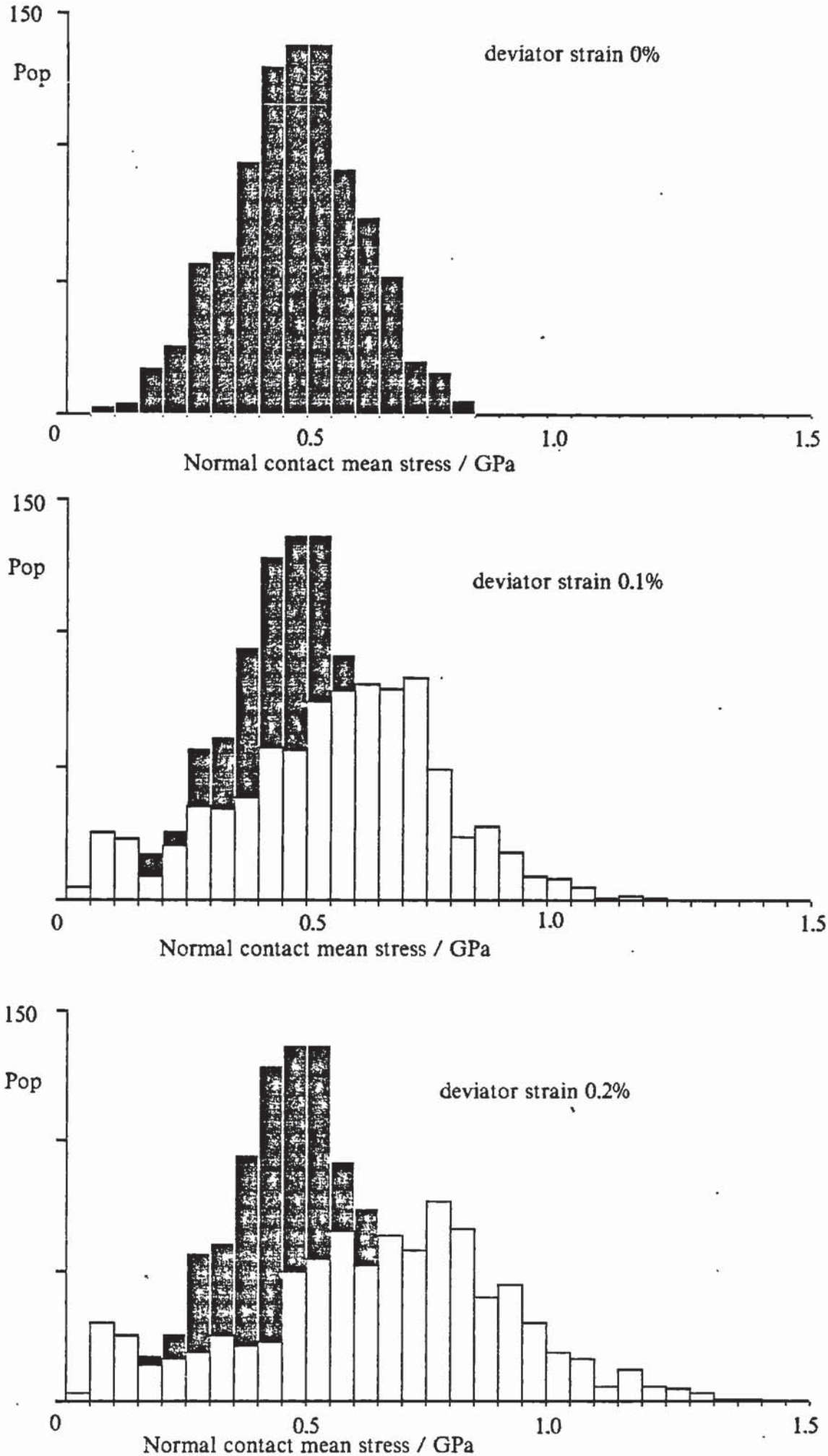

Fig 6.42 Histogram of the distribution of normal mean contact stress for graded assembly at 0%, 0.1% and 0.2% deviator strain.

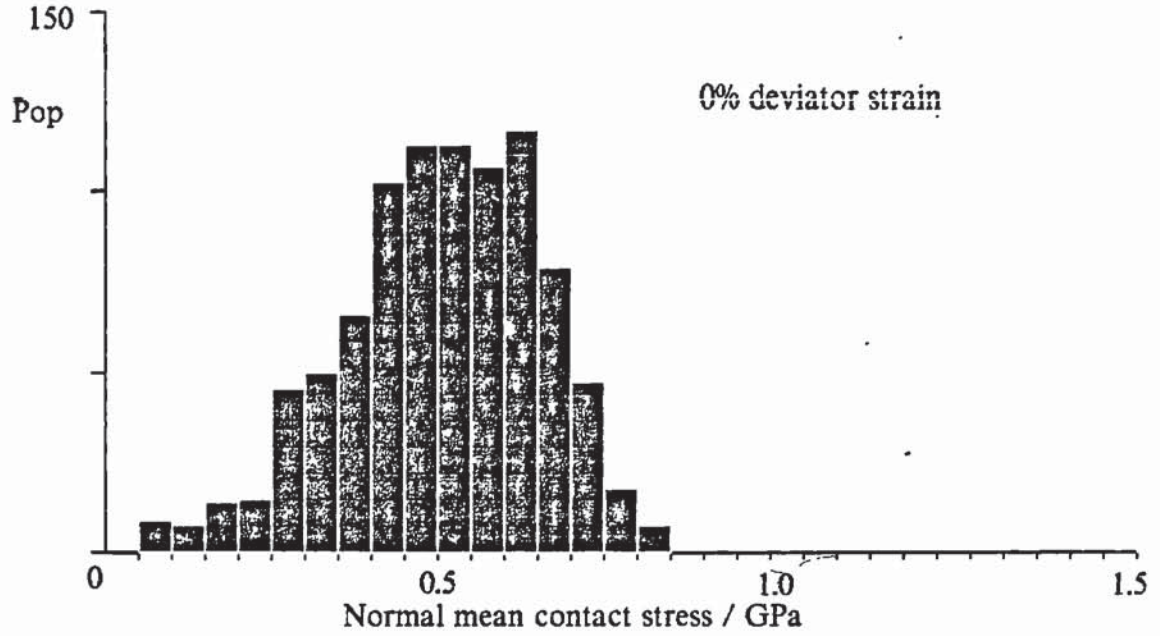

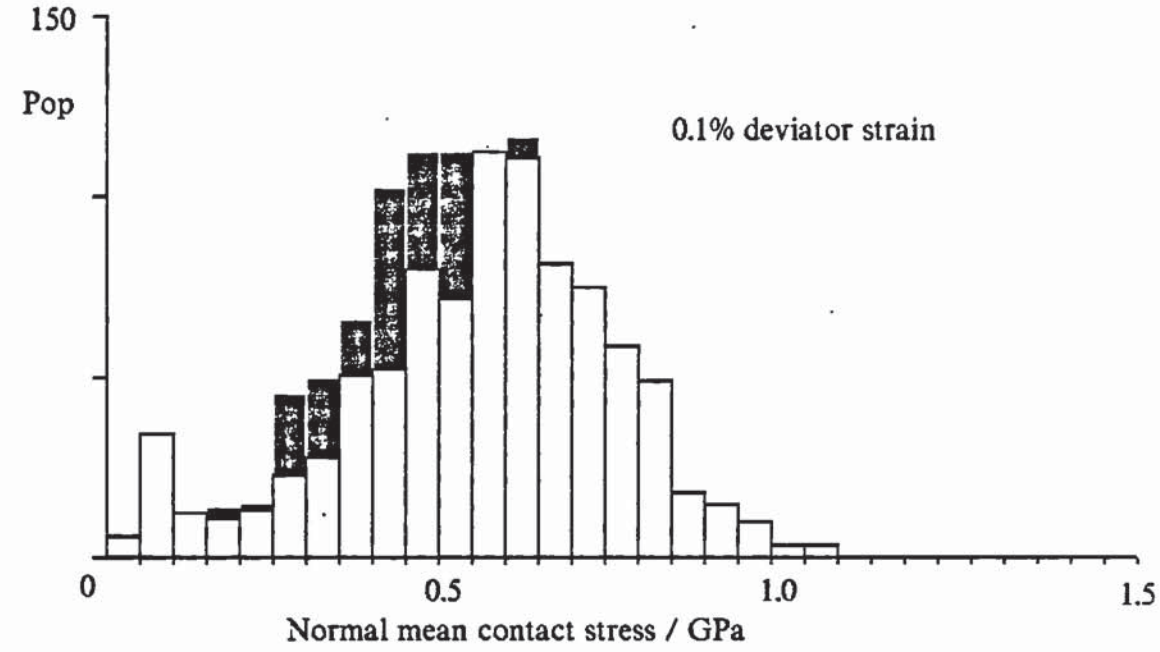

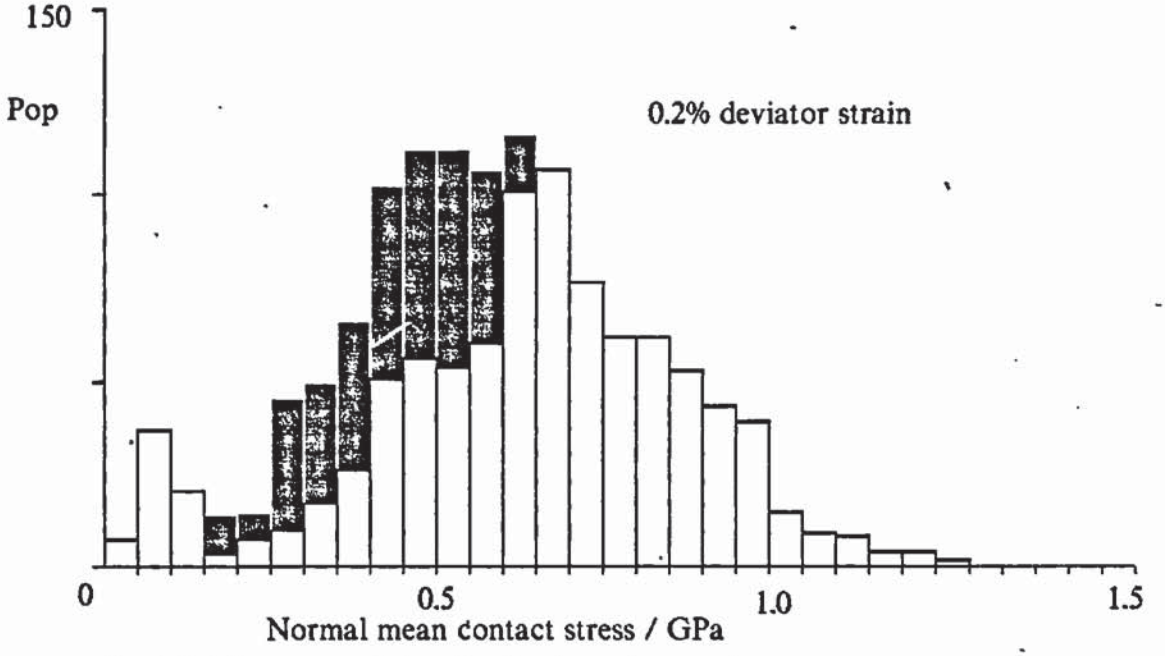

Fig 6.43 Histogram of the distribution of normal mean contact stress for uniform assembly at 0%, 0.1% and 0.2% deviator strain.

Both assemblies have the same range of stress variation and similar numbers of contacts, but the uniform assembly has slightly less contacts in the mid range of the histogram. Also the uniform assembly exhibits a large number of contacts with mean normal contact stresses, and therefore contact forces, close to the average. This is due to the localised zones of regular packing reported earlier in this section. With both assemblies as the deviator strain is applied the spread of the distributions increases with a small increase in the average mean normal contact stress. With the exception of contacts carrying very small normal forces the distribution remains essentially normal.

The two constant volume shear tests reported in this section exhibit very similar behaviour. The difference the grading had on the behaviour of the two assemblies was characterised by the establishment of the linear force chains produced by regular packed zones in the uniform assembly.

The consequence of incorporating the force-displacement laws of Hertz (1882) and Mindlin and Deresiewicz (1953) was that the two assemblies were very stiff. Both reached their maximum sin Φ values before 0.2% applied deviator strain, whereas the 1000 disc test reported by Barnes (1985) had not quite reached its maximum sin Φ by 3% strain. This difference is primarily due to the introduction of the non-linear Hertzian normal force-displacement law. Due to the small contribution to sin Φ by the tangential force it can be concluded that in the simulation of quasi-static shear deformation the implementation of the tangential force-displacement laws of Mindlin and Deresiewicz (1953) has little effect.

7. Summary and Conclusions.

The work presented in this thesis is concerned with the computer simulation of two dimensional systems of smooth elastic spheres employing contact friction. The objective of the research programme was to incorporate contact mechanics based algorithms into the computer simulation program BALL in order to more realistically model particle interactions, to validate these new algorithms, and to apply the amended program to simulate the behaviour of large systems of particles.

The force-displacement laws of Hertz (1882) and Mindlin and Deresiewicz (1953) are covered in Chapter 3. It was shown that all possible tangential force-displacement loading situations can be modelled by one general expression, equation 3.94, with appropriate substitutions for loading, unloading or reloading tangentially.

Chapter 4 describes in detail the logic of the new coding necessary to implement the contact mechanics interaction laws. Many other alterations and additions to the computer program are also explained. Of these the most significant are the automatic scaling of certain fixed parameters to a function of the maximum particle size and the introduction of S.I. units. This enables a wide range of problems to be simulated with particle sizes varying by orders of magnitude.

In order to validate the contact mechanics algorithms simple quasi-static and dynamic tests were simulated, which are described in Chapter 5. Results from simulations of single particle oblique impact showed excellent agreement with the theoretical and experimental work of Maw et al (1976)

(1981). Consequently it can be concluded that the program is capable of producing quantitatively realistic information when applied to problems involving large systems of particles.

Applications of the program to the simulation of large systems of particles are reported in Chapter 6. Results obtained from simulations of hopper flow and pluvially deposited packed beds demonstrated the satisfactory performance of the program. Further research on hopper flow simulations, using several thousand particles, could be a rewarding area for future applications of the program.

In Chapter 6 a detailed discussion of different methods of isotropic compression of circular assemblies is given. It was shown that the successful compression of an assembly could only be achieved by the joint use of the continuum strain rate tensor and a compatible boundary strain rate tensor. However, when using the same control in attempting to shear the assemblies instabilities occurred. These instabilities were suppressed with the introduction of mass proportional damping, developed by Cundall (1971). An investigation into the optimum value of mass proportional damping for the suppression of assembly instabilities was then undertaken. As a result it was concluded that although the continuum strain rate and boundary strain rate tensors could control the shear stage, provided sufficient mass proportional damping was used to suppress assembly instabilities, such high out of balance to contact force ratios occurred that the assembly could not be considered to be close to equilibrium. The shear control was then simplified to the boundary strain rate tensor only and the quasi-static shear deformation of two assemblies was simulated.

From the successful constant volume shear tests reported in section 6.5.2, performed on uniform and graded assemblies of particles, the effect of the addition of contact mechanics algorithms into the simulation was demonstrated. It was shown that the Hertzian normal force-displacement law resulted in a very stiff assembly when compared with a similar simulation using linear spring force-displacement laws, reported by Barnes (1985). The maximum sin Φ values were less than the maximum sin Φ value obtained by Barnes (1985), this may be a consequence of the slightly higher porosity of the assemblies used in the new tests. However, implementation of the tangential force-displacement laws of Mindlin and Deresiewicz (1953) had little effect on the shear deformation of the assembly, as the percentage of sliding contacts and the tangential force contribution to sin Φ were similar to the values obtained from the test employing linear springs, Barnes (1985).

The adaptation of the program BALL to simulate particles with sizes from microns to metres, the addition of real units, and the incorporation of dynamic contact mechanics algorithms make the simulation program ideally suited to problems associated with process engineering, such as rapid shear flow. For these dynamic simulations the effect of the incorporation of the force-displacement laws of Mindlin and Deresiewicz (1953) would have a much more significant advantage over linear spring force-displacement laws.

As a result of the incorporation of contact mechanics algorithms into the simulation program, validation of the coding and the successful simulation of dynamic flow, arrested flow and quasi-static shear deformation of large

assemblies of particles, all the objectives of the research programme have been fulfilled.

References

Alder, B.J. and Wainwright, T.E. (1959), Studies in Molecular Dynamics. I. General Method, The Journal of Chemical Physics, Vol. 31,2: 459-466.

Andersen, H.C. (1980), Molecular Dynamics Simulations at Constant Pressure and/or Temperature, The Journal of Chemical Physics (February 1980), Vol. 72, 4: 2384-2393.

Ashurst, W.T. (1974), Dense Fluid Shear Viscosity and Thermal Conductivity via Non-Equilibrium Molecular Dynamics, Ph.D. thesis, University of California, Davis.

Ashurst, W.T. and Hoover, W.G. (1972), Non-Equilibrium Molecular Dynamics: Shear Viscosity and Thermal Conductivity, Bulletin American Physical Society (1972), Vol. 17: 1196-1197.

Babic, M. (1988), Discrete Particle Numerical Simulation of Granular Material Behavior, Report No. 88-11, Department of Civil and Environmental Engineering, Clarkson University, Potsdam, New York.

Barnes, D.J. (1985), A Study of the Micro-mechanics of Granular Media, Ph.D. thesis, University of Aston in Birmingham.

Bathurst, R.J. and Rothenburg, L. (1988), Micromechanical Aspects of Isotropic Granular Assemblies With Linear Contact Interactions, Journal of Applied Mechanics (March 1988), Vol. 55: 17-23.

Blackburn, D.J. (1983), An Investigation into the Mechanics of Regular Arrays of Discs and Spheres, Ph.D. thesis, University of Aston in Birmingham.

Campbell, C.S. and Brennen, C.E. (1982), Computer Simulation of Chute Flows of Granular Materials, IUTAM Conference on Deformation and Failure of Granular Materials, Delft, 31 Aug.- 3 Sept. 1982. 515-521.

Campbell, C.S. and Brennen, C.E. (1985), Chute Flows of Granular Material: Some Computer Simulations, Transactions of the ASME (March 1985), Vol. 52: 172-178.

Cape, J.N. and Woodcock, L.V. (1980), Soft-sphere Model for the Crystal-liquid Interface: A Molecular Dynamics Calculation of the Surface Stress, The Journal of Chemical Physics (September 1980), Vol. 73, 5: 2420-2429.

Ciccotti, G. and Jacucci, G. (1975), Direct Computation of Dynamical Response by Molecular Dynamics: The Mobility of a Charged Lennard-Jones Particle, Physical Review Letters (September 1975), Vol, 35, 12: 789-795.

Ciccotti, G., Jacucci, G. and McDonald, I.R. (1979), "Thought-Experiments" by Molecular Dynamics, Journal of Statistical Physics, Vol. 21, 1: 1-22.

Cundall, P.A. (1971), A Computer Model for Simulating Progressive Large-scale Movements in Blocky Rock Systems, Proc. Symp. Int. Soc. Rock Mech., Nancy II, Art 8.

Cundall, P.A. (1974), A Computer Model for Rock-mass Behaviour Using Interactive Graphics for the Input and Output of Geometrical Data, report prepared under Contract No. DACW 4S-74-C-006, for the Missouri River Division, U.S. Army Corps of Engineers, University of Minnesota.

Cundall, P.A. (1976), Explicit Finite-Difference Methods in Geomechanics, 2nd International Conference on Numerical Methods in Geomechanics, Blacksburg V.A., 132-150.

Cundall, P.A. (1978), BALL- A Program to Model Granular Media using the Distinct Element Method, Dames and Moore, Advanced Technology Group, London.

Cundall, P.A. (1988), Computer Simulations of Dense Sphere Assemblies, Micromechanics of Granular Materials, (Eds. M. Satake and J.T. Jenkins), Elsevier, Amsterdam (1988), 113-123.

Cundall, P.A. and Strack, O.D.L. (1979a), A Discrete Numerical Model for Granular Assemblies, Geotechnique (1979), Vol. 29, 1: 47-65.

Cundall, P.A. and Strack, O.D.L. (1979b), The Distinct Element Method as a Tool for Research in Granular Media, Part II, Dept. Civ. Min. Engng. Univ. Minnesota.

Cundall, P.A., Drescher, A. and Strack, O.D.L. (1982), Numerical Experiments on Granular Assemblies: Measurements

and Observations, IUTAM Conference on Deformation and Failure of Granular Materials, Delft, 31. August- 3. September 1982.

Cundall, P.A. and Strack, O.D.L. (1983), Modelling of Microscopic Mechanisms in Granular Material, Mechanics of Granular Materials: New Models and Constitutive Relations, (Eds. J.T. Jenkins and M. Satake), Elsevier, Amsterdam (1988), 137-149.

Deresiewicz, H. (1968), A Note on Hertz's Theory of Impact, Acta Mechanica (1968), Vol. 6: 110-112.

De Josselin de Jong, G. and Verruijt, A. (1969), Etude Photo-elastique d'un Epilement de Disques, Cah. Grpe fr etud. Rheol. Vol 2: 73.

Erginsoy, C., Vineyard, G.H. and Englert, A. (1964), Dynamics of Radiation Damage in a Body-Centered Cubic Lattice, Physical Review (January 1964), Sect. A, Vol. 133, 2: 595-606.

Evans, D.J. (1979), The Frequency Dependent Shear Viscosity of Methane, Molecular Physics (1979), Vol. 37, 6: 1745-1754.

Evans, D.J. (1981), Rheological Properties of Simple Fluids by Computer Simulation, Physical Review (April 1989), Sect. A, Vol. 23, 4:1988-1997.

Evans, D.J. and Hanley, H.J.M. (1979), Viscosity of a Mixture of Soft Spheres, Physical Review (October 1979),

Sect. A, Vol. 20, 4: 1648-1655.

Gosling, E.M., McDonald, I.R. and Singer, K. (1973), On the Calculation by Molecular Dynamics of the Shear Viscosity of a Simple Fluid, Molecular Physics (1973), Vol. 26, 6: 1475-1484.

Haff, P.K. and Werner, B.T. (1985), The Collisional Interaction of a Small Number of Confined Inelastic Grains, Brown Bag Preprint Series, Division of Physics, Mathematics and Astronomy, California Institute of Technology, (May 1985).

Hanley, H.J.M. and Evans, D.J. (1980), Equilibrium and Nonequilibrium Radial Distribution Functions in Mixtures, Molecular Physics (1980), Vol. 39, 4: 1039-1042.

Hanley, H.J.M. and Evans, D.J. (1981), Behavior of a Nonconformal Mixture via Computer Simulation, International Journal of Thermophysics (1981), Vol. 2, 1: 1-19.

Hanley, H.J.M. and Evans, D.J. (1982), A Thermodynamics for a System Under Shear, The Journal of Chemical Physics (March 1982), Vol. 76, 6: 3225-3232.

Hawkins, G.W. (1983), Simulation of Granular Flow, Mechanics of Granular Materials: New Models and Constitutive Relations, 305.

Hertz (1882). Refer to Timoshenko, S. and Goodier, J.N. (1970), Theory of Elasticity, McGraw-Hill Book Company, New

York, 3rd Edition, 402-424.

Hess, S. and Hanley, H.J.M. (1982), Distortion of the Structure of a Simple Fluid, Physical Review (March 1982), Sect. A, Vol. 25, 3: 1801-1805.

Heyes, D.M., Kim, J.J., Montrose, C.J. and Litovitz, T.A. (1980), Time Dependent Nonlinear Shear Stress Effects in Simple Liquids: A Molecular Dynamics Study, The Journal of Chemical Physics (October 1980), Vol. 73, 8: 3987-3996.

Hockney, R.W. and Buneman (1963). Refer to Hockney, R.W. and Eastwood, J.W. (1981), Computer Simulation Using Particles, McGraw-Hill Book Company, New York.

Hoover, W.G. (1986a), Dynamic Compaction of Powders, Computer Simulation in Physical Metallurgy (Ed. G. Jacucci), 69-85.

Hoover, W.G. (1986b), Flow and Plasticity via Non-equilibrium Molecular Dynamics, Computer Simulation in Physical Metallurgy (Ed. G. Jacucci), 87-106.

Hoover, W.G. (1986c), Simulation of Brittle Fracture via Molecular Dynamics, Computer Simulation in Physical Metallurgy (Ed. G. Jacucci), 145-158.

Hoover, W.G., Ladd, A.J.C. and Hickman, R.B. (1980a), Bulk Viscosity via Non-equilibrium and Equilibrium Molecular Dynamics, Physical Review (May 1980), Sect. A, Vol. 21, 5: 1756-1760.

Hoover, W.G., Evans, D.J., Hickman, R.B., Ladd, A.J.C., Ashurst, W.T. and Moran, B. (1980b), Lennard-Jones Triple-point Bulk and Shear Viscosities. Green-Kubo Theory, Hamiltonian Mechanics, and Non-equilibrium Molecular Dynamics, Physical Review (October 1980), Sect. A, Vol. 22, 4: 1690-1697.

Ishibashi, I. and Chen, Y.C. (1988), Dynamic Shear Moduli and their Relationship to Fabric of Granular Materials, Mlchromechanics of Granular Materials (Eds. M. Satake and J.T. Jenkins), Elsevier (1988), Amsterdam, 95-102.

Jenkins, J.T. (1988), Volume Change in Small Strain Axisymmetric Deformations of a Granular Material, Micromechanics of Granular Materials, (Eds. M. Satake and J.T. Jenkins), Elsevier (1988), Amsterdam, 245-252.

Johnson, K.L. (1982), One hundred years of Hertz contact, Proceedings of the Institute of Mechanical Engineers, Vol 196, 363-378.

Johnson, K.L. (1985), Contact Mechanics, Cambridge University Press, ISBN 0521 255767.

Lotstedt, P. and Dahlquist, G. (1978), Interactive Simulation of the Progressive Collapse of a House, Numerical Methods for Differential Equations and Simulation, (Eds. A.W. Bennett and R. Vichnevetsky), North-Holland Publishing Company, 135-138.

Maw, N., Barber, J.R. and Fawcett, J.N. (1976), The Oblique Impact of Elastic Spheres, Wear (1976), Vol. 38, 1: 101-114.

Maw, N., Barber, J.R. and Fawcett, J.N. (1981), The Role of Elastic Tangential Compliance in Oblique Impact, Transactions of the ASME (January 1981), Vol. 103: 74-80.

Metropolis, N., Rosenbluth, A.W., Rosenbluth, M.N., Teller, A.H. and Teller, E. (1953), Equation of State Calculations by Fast Computing Machines, The Journal of Chemical Physics (June 1953), Vol. 21, 6: 1087-1092.

Mindlin, R.D. (1949), Compliance of Elastic Bodies in Contact, Journal of Applied Mechanics, 259-268.

Mindlin, R.D. and Deresiewicz (1953), Elastic Spheres in Contact Under Varying Oblique Forces, Journal of Applied Mechanics (September 1953), Vol. 20:327-344.

Naitoh, T. and Ono, S. (1979), The Shear Viscosity of a Hard-sphere Fluid via Nonequilibrium Molecular Dynamics, The Journal of Chemical Physics (May 1979), Vol. 70: 4515-4523.

Oda, M. and Konishi, J. (1974), Microscopic Deformation Mechanism of Granular Material in Simple Shear, Soils and Foundations, Jap. Soc. of Soil Mech. and Found. Eng., Vol. 14, 4: 25-38.

Oda, M., Nemat-Nasser, S. and Mehrabadi, M. M. (1982), A statistical study of fabric in a random assembly of spherical granules, International Journal of Analytical Methods in Geomechanics, Vol 6, 77-94.

Petrakis, E., Dobry, R. and Ng, T. (1988), Small Strain Response of Random Arrays of Elastic Spheres Using a Nonlinear Distinct Element Procedure, Prepared under Grant AFOSR-86-0135 United States Air Force Office of Scientific Research, Bolling Air Force Base, Washington, Report No. CE-88-02.

Platts, J.C. (1989), Final Year Undergraduate Research Project, Dept. of Civil Engineering, University of Aston in Birmingham.

Pollock, E.L. and Alder, B.J. (1980), Static Dielectric Properties of Stockmayer Fluids, North Holland Publishing Company, 1980.

Rahman, A. (1964), Correlations in the Motion of Atoms in Liquid Argon, Physical Review (October 1964), Sect. A, Vol. 136, 2: 405-411.

Strack, O.D.L. and Cundall, P.A. (1978), The Distinct Element Method as a Tool for Research in Granular Media, Part I, Dept. Civ. Min. Engng. Univ. Minnesota.

Szalwinski, C.M. (1985), Flexibility of a Contact Area of an Isotropic Elastic Body, Journal of Applied Mechanics (March 1985), Vol. 52: 62-66.

Thornton, C. (1987a), Computer Simulated Experiments on Particulate Material, Tribology in Particulate Technology, (Eds. Briscoe and Adams), Adam-Hilger, 292-302.

Thornton, C. (1987b), Induced Anisotropy and Energy Dissipation in Particulate Material- Results from Computer Simulated Experiments, Proc. IUTAM/ICM Symp. on Yielding, Damage and Failure of Anisotropic Solids, Villard de Lans, (24-28 August 1987).

Thornton, C. and Barnes, D.J. (1986a), Evolution of Stress and Structure in Particulate Material, Applied Solid Mechanics- 1 (Eds. Tooth and Spence), Elsevier (1988), Amsterdam, 191-204.

Thornton, C. and Barnes, D.J. (1986b), Computer Simulated Deformation of Compact Granular Assemblies, Acta Mechanica (1986), Vol. 64: 45-61.

Thornton, C. and Randall, C.W. (1988), Applications of Theoretical Contact Mechanics to Solid Particle System Simulation, Micromechanics of Granular Materials, (Eds. M. Satake and J.T. Jenkins), Elsevier (1988), Amsterdam, 133-142.

Ting, J.M., Corkum, B.T., Kauffman, C.R. and Greco, C. (1989), Discrete Numerical Model for Soil Mechanics, Journal of Geotechnical Engineering (March 1989), Vol. 115, 3: 379-398.

Walton, O.R. (1983), Computer Simulation of Shearing Flow of Inelastic Frictional Particles in Two Dimensions, Proc. 1st European Symp. on Stress and Strain Behaviour in Granular

Media, CHISA Congress, Prague 1984.

Walton, O.R. (1984), Application of Molecular Dynamics to Macroscopic Particles, International Journal of Engineering Science (1984), Vol. 22, 8-10: 1097-1107.

Watts, R.O. (1981), Molecular Dynamics Study of Electric Polarisation, Chemical Physics Letters (June 1981), Vol. 80, 2: 211-214.

Webster, S.P. (1989), Final Year Undergraduate Research Project, Dept. of Civil Engineering, University of Aston in Birmingham.

Werner, B.T. and Haff, P.K. (1985), Dynamical Simulations of Granular Materials Using Concurrent Processing Computers, Brown Bag Preprint Series, Division of Physics, Mathematics and Astronomy, California Institute of Technology.

Werner, B.T. and Haff, P.K. (1986), The Impact Process in Eolian Saltation: Two-dimensional Studies, Brown Bag Preprint Series, Division of Physics, Mathematics and Astronomy, California Institute of Technology.

Zwanzig, R. (1981), Nonlinear Shear Viscosity and Long Time Tails, Applied Physical Sciences (June 1981), Vol. 78, 6: 3296-3297.